Novel Phases and Dynamic Signatures of Kondo Lattice Model

Jing Luo

Hubei, China

BS Physics,

Wuhan University,

Wuhan, China, 2014

A Dissertation presented to

the Graduate Faculty of the University of Virginia

in Candidacy for the Degree of

Doctor of Philosophy

Department of Physics

University of Virginia

July, 2020

Acknowledgements

First and foremost, I would like to express my sincere gratitude to my advisor Prof. Gia-Wei Chern, for his continuous support and mentorship. Prof. Chern has spent much of his precious time and effort teaching and guiding me. I learnt considerably from his patient and careful mentorship on various aspects including research, presentation, communication and writing. I am especially thankful for the opportunities given to me to improve myself.

Besides my advisor, I would like to thank other defense committee members, Prof. Keivan Esfarjani, Prof. Seunghun Lee and Prof. Israel Klich, for their insightful questions, valuable comments and suggestions. I thank Prof. Israel Klich again for the collaborations with him and his student Amr Ahmadain. I would also like to thank Prof. Utpal Chatterjee and Prof. Seunghun Lee for serving on my research committee, the questions they asked, and the encouragement they gave to me.

Next, I would like to express my appreciation to students in our group, including Preetha Saha, Zhijie Fan, Puhan Zhang, Zhongzheng Tian, Sheng Zhang, Chen Cheng for the time we spent together. I learnt a lot from them and the presence of them made my life more enjoyable. I would also like to thank some students who I enjoyed various collaborations with, Depei Zhang, Syed Raza, Meng Hua, Amr Ahmadain.

I would like to thank the department of physics at the University of Virginia for offering such a great opportunity for my Ph.D. studies.

Finally, I would like to thank my parents, grandparents, and my sister for their continued encouragement and support.

Abstract

The Kondo lattice model is one of the most fundamental models that have received tremendous theoretical interest. It describes strongly correlated systems with interaction between itinerant electrons and local magnetic moments. This interaction plays an important role in heavy fermion materials, where local magnetic moments interact with $4f$ or $5f$ electrons which behaves as if they are effectively much heavier than themselves. In this thesis, we present a few numerical studies on the Kondo lattice model and models based on Kondo chains.

Tensor network is a geometric architecture composed of connected tensors to represent quantum many body states. The representation turns out to be surprisingly efficient for area law states, in which the entanglement entropy scales linearly with the surface area of the system, rather than the volume as in a generic state. Tensor network algorithms have witnessed fast development in the past near 30 years. Density matrix renormalization group (DMRG), popularized in the last two decades for low dimensional system studies, and time-evolving block decimation (TEBD) are two representatives. In this thesis, we characterize the phases of one-dimensional Kondo lattice model with quantum localized spins using DMRG, and present the quench dynamics of the model using TEBD.

Highly frustrated magnets have attracted considerable attention with its intriguing and sometimes unexpected magnetic phases. In this thesis, we present an extensive numerical study of a new type of frustrated itinerant magnetism on the pyrochlore lattice. In this theory, the pyrochlore magnet can be viewed as a cross-linking network of Kondo or double-exchange chains. Contrary to models based on Mott insulators, this itinerant magnetism approach provides a natural explanation for several spin and orbital superstructures observed on the pyrochlore lattice. Through extensive Monte Carlo simulations, we obtain the phase diagrams at two representative electron filling

fractions $n = 1/2$ and $2/3$. For the half filling case, we observed a paramagnetic phase and an all-in-all-out phase, mimicking a spin ice. For the case of $2/3$ filling, we found a $\left(\frac{1}{3}, \frac{1}{3}, 1\right)$ magnetic order, ferromagnetic phase, paramagnetic phase and an unexpected $\left(\frac{1}{2}, \frac{1}{2}, \frac{1}{2}\right)$ order. In particular, we show that the intriguing glassy magnetic state characterized by ordering wavevectors $\mathbf{q} = \left(\frac{1}{3}, \frac{1}{3}, 1\right)$ gives a rather satisfactory description of the low temperature phase recently observed in spinel $GeFe_2O_4$.

Finally, we present extensive large-scale dynamical simulations of the phase separated states, which are a mixture of ferromagnetic metallic cluster and antiferromagnetic insulating regions, in the double exchange model. These inhomogeneous electronic states play a crucial role in the colossal magnetoresistance phenomenon (CMR). The double-exchange model (Kondo lattice model) is considered as a major mechanism for its electronic phase separation. We present an innovative and efficient von-Neumann Landau-Lifshitz dynamics framework which enables large-scale dynamical simulation of inhomogeneous electronic states for the very first time. We compute the dynamical structure factor of these nanoscale textures using. Dynamical signatures of the various underlying magnetic structures are identified. At small hole doping, the structure factor exhibits a dominating signal of magnons from the background Néel order and localized modes from magnetic polarons. A low-energy continuum due to large-size ferromagnetic clusters emerges at higher doping levels. Implications for experiments on magnetoresistive manganites are also discussed.

Contents

List of Figures

Chapter 1

Introduction

1.1 Overview

Condensed matter physics is a field that studies the collective behavior of atoms and electrons in condensed matter. It covers a wide variety of phenomenon such as superconducting, phase transition. Complexity emerges when individual atoms and electrons are grouped together. The collective behavior could be dramatically different from that of the individual components.

Strongly correlated systems have attracted tremendous attention and research efforts. Interesting phenomenon appear due to the strong interactions and correlations. Topics include high temperature superconducting, colossal magnetoresistance. In the real word, understanding the physics of strongly correlated system help us develop next generation electronic technology for real life and industry applications, such as Mott transistor, multiferroicity. Over decades, the research on strongly correlated systems has seen seen its breakthrough and become the building block of condensed matter physics.

The study of strongly correlated systems is a board area. There are many rep-

resentative models. In this thesis, we focus on the systems where itinerant electrons interact with local magnetic moments. More specifically, the model is expressed in the Hamiltonian with both electron degree of freedom and spin degree of freedom,

$$\mathcal{H} = -t \sum_{\langle i,j \rangle} \sum_{\sigma=\uparrow,\downarrow} \left(c^{\dagger}_{i,\sigma} \, c_{j,\sigma} + \text{h.c.} \right) + J \sum_{i} \mathbf{S}_i \cdot \mathbf{s}_i, \tag{1.1}$$

where the first term describes electron hopping between nearest-neighbor sites, and the second term is the onsite coupling between electrons $\mathbf{s}_i = \sum_{\alpha,\beta} c^{\dagger}_{i\alpha} \boldsymbol{\sigma}_{\alpha\beta} c_{i\beta}$ and local magnetic moments $\mathbf{S}_i$.

For antiferromagnetic onsite coupling ($J > 0$), this is the Kondo lattice model. The local spins are quantum. This is taken as the standard model for heavy fermion systems.

When the coupling is ferromagnetic ($J < 0$), this is the double exchange model, also known as ferromagnetic Kondo lattice model. It is worth noting that although these two models have the same form of Hamiltonian, the antiferromagnetic and ferromagnetic interactions come from different mechanisms. In this model, even classical local spins can result in rich phases diagrams. A model on a specific lattice structure, such as pyrochlore, could also result in geometrical frustration.

1.2 The Kondo Lattice Model and Heavy Fermion Materials

Heavy fermion materials are in general a class of inter-metallic compounds with rare earth or actinide elements [8]. These elements typically contain $4f$ or $5f$ electrons that are highly localized, which is the origin of the local magnetic moments [9]. These materials exhibits energy scales typically as small as a few tens of Kelvin, giving rise

to extremely enhanced specific heat and spin susceptibility [8]. The effective mass of electron quasiparticles is typically a few hundreds or thousands of the bare electron mass. Thus these electron quasiparticles are named heavy fermions.

The physics of these materials are dominated by the interactions between itinerant electrons and the localized moments. A model to describe heavy fermion systems is the periodic Anderson model which considers the interaction between two types of electrons, the itinerant electrons and the localized f electrons [8]. In the Kondo regime, this model can be transformed into the Kondo lattice model, where local moments are immersed in a conducting background and favor antiferromagnetic configurations with onsite electrons. We will give a detailed introduction to the Kondo lattice model in Chapter 2 and present our study on its quench dynamics.

1.3 The Double Exchange Model and the Manganites

The double exchange model has the same expression as the Kondo lattice model, with the difference that the coupling between the local magnetic moments and conducting electrons is ferromagnetic, rather than antiferromagnetic as in the Kondo lattice model. However, they come from different mechanisms. This ferromagnetic coupling in the double exchange model originates from Hund's coupling, which is not considered in the Kondo lattice model since the orbital degeneracy is ignored.

The double exchange model was proposed to describe the physics of manganites, a class of mineral with chemical formula $T_{1-x}D_xMnO_3$, where T is a trivalent rare earth element or Bi^{3+} cation, D is a divalent alkaline or Pb^{2+} cation [10]. The most interesting characteristic property of manganites is colossal magnetoresistance (CMR), where a small magnetic field could induce a dramatic change in the electrical

resistance.

In Chapter 4, we discuss our dynamical simulations on the phase separated states in the square lattice double exchange model.

1.4 Layout of the Thesis

Although tremendous efforts have been spent on the equilibrium phases of the Kondo lattice model and double exchange model, at least two aspects are less explored: **spatial inhomogeneity** and **dynamics**. In this thesis, we will present a few numerical studies that focus more on these two aspects.

The layout of the thesis is as follows. In chapter 2, we present a numerical study on the one-dimensional Kondo lattice model with quantum localized spins. We give a detailed introduction to tensor network states. Two tensor network based algorithms are also introduced: density matrix renormalization group (DMRG) and time-evolving block decimation (TEBD). We apply the essentially exact DMRG to study phases of the model, and study its quench dynamics using TEBD.

In chapter 3, we discuss the frustrated Kondo chains with classical local spins on the pyrochlore lattice. The corss-linked Kondo chains give rise to a new type of geometrical frustration. We present extensive numerical simulations on this model and characterize its phase diagrams at two representative filling fractions 1/2 and 2/3. This study is also experiment motivated and the glassy magnetic phase characterized by the ordering wavevector $\mathbf{q} = \left(\frac{1}{3}, \frac{1}{3}, 1\right)$ at 2/3 filling gives a rather satisfactory description of the low temperature phase recently observed in spinel $GeFe_2O_4$. The discussion on 1D Kondo chains with classical local spins is also included for comparison and illustration.

In chapter 4, we focus on the spatial inhomogeneity of the model, especially the

phase separated states mixed by the ferromagnetic metallic clusters and antiferromagnetic insulating regions. These inhomogeneous electronic states are believed to play an import role in colossal magnetoresistance. However, the dynamics of this phase was less explored partly due to a lack of efficient numerical methods. To this end, we introduce a real-space von-Neumann Landau-Lifshitz (LLvN) dynamics which enables large-scale dynamical simulation of the phase separated states. We compute the dynamical structure factor and identity the dynamical signatures, especially the roles of the magnetic polarons and larger metallic clusters. We also discuss the implications for experiments on magnetoresistive manganites.

In chapter 5, we summarize the thesis and point out some possible future directions.

1.5 Publication List

Below is a list of publication. The thesis is based on [1], [2] and some unpublished work.

[1] **J. Luo**, G. Chern, *Dynamics of the phase separated states in the double exchange model*, arXiv 1904.05252 (2019).

[2] **J. Luo**, G. Chern, *Frustrated Kondo chains and glassy magnetic phases on the pyrochlore lattice*, Phys. Rev. B **98**, 214423 (2018).

[3] B. S. Shivaram, **J. Luo**, G. Chern, D. Phelan, R. Fittipaldi, A. Vecchione, *Nonlinear Pauli susceptibilities in $Sr_3Ru_2O_7$ and universal features of itinerant metamagnetism*, Phys. Rev. B **97**, 100403 (Rapid Communication) (2018).

Chapter 2

Quench Dynamics of One-dimensional Kondo Lattice Model

In this chapter, we discuss the Kondo lattice model, especially the one-dimensional Kondo lattice model. After that we introduce tensor network, especially its one-dimension version matrix product states, and some tensor network algorithms, namely, density matrix renormalization group (DMRG), time-evolution block decimation (TEBD). These algorithms are extensively used in the investigation in this chapter. We apply DMRG to obtain the phases of the one-dimensional Kondo lattice model and apply TEBD to study its quench dynamics between some states.

2.1 Introduction

To introduce the Kondo lattice model, we first give an introduction to the Kondo model. The *Kondo model* (also referred to as the *s-d model*) is a model that describes

the effect of a single local magnetic moment (impurity) interacting with a background of conducting electrons. It is usually expressed in the following form,

$$\mathcal{H} = \sum_{\mathbf{k},\sigma} \epsilon_{\mathbf{k}} c^{\dagger}_{\mathbf{k}\sigma} c_{\mathbf{k}\sigma} + J\mathbf{S} \cdot \mathbf{s}_0, \tag{2.1}$$

where $c^{\dagger}_{\mathbf{k}\sigma}$ is the creation operator for the electron with momentum $\mathbf{k}$ and spin σ, $J > 0$ measures the strength of the interaction between the local impurity $\mathbf{S}$ with spin-$\frac{1}{2}$ at the origin and the conducting electron

$$\mathbf{s}_0 = \sum_{\mathbf{k},\mathbf{k}',\sigma,\sigma'} c^{\dagger}_{\mathbf{k}\sigma} \sigma_{\sigma,\sigma'} c_{\mathbf{k}'\sigma'}, \tag{2.2}$$

at the impurity site. The Kondo model was studied by Jun Kondo [11] in 1964 to account for the phenomenon resistance minimum at low temperatures in dilute magnetic alloys.

The electrical resistivity were deemed to decrease monotonically with the decreasing temperature, due to the contributions from phonon scattering. However, W. J. de Haas, J. de Boer, and G.J.van den Berg [12] discovered in 1934 that in "not very pure" gold wires with less than $10^{-4}\%$ impurity, the resistivity starts to increase below a certain temperature (3.70 K), resulting in a resistance minimum.

One of the most well known sets of the measurement that shows resistance minimum was taken in 1964 [1]. They measured alloys $\mathrm{Mo}_x\mathrm{Nb}_{1-x}$ and $\mathrm{Mo}_x\mathrm{Re}_{1-x}$ with and without 1% Fe. The scaled resistivity for $(\mathrm{Mo}_x\mathrm{Nb}_{1-x})_{0.99}\mathrm{Fe}_{0.01}$ is shown in Fig. 2.1.

The phenomenon has been a puzzle for over 30 years until Jun Kondo solved this problem. He analyzed the experimental observations and found that this phenomenon is closely related to the existence of magnetic impurities. These observations also

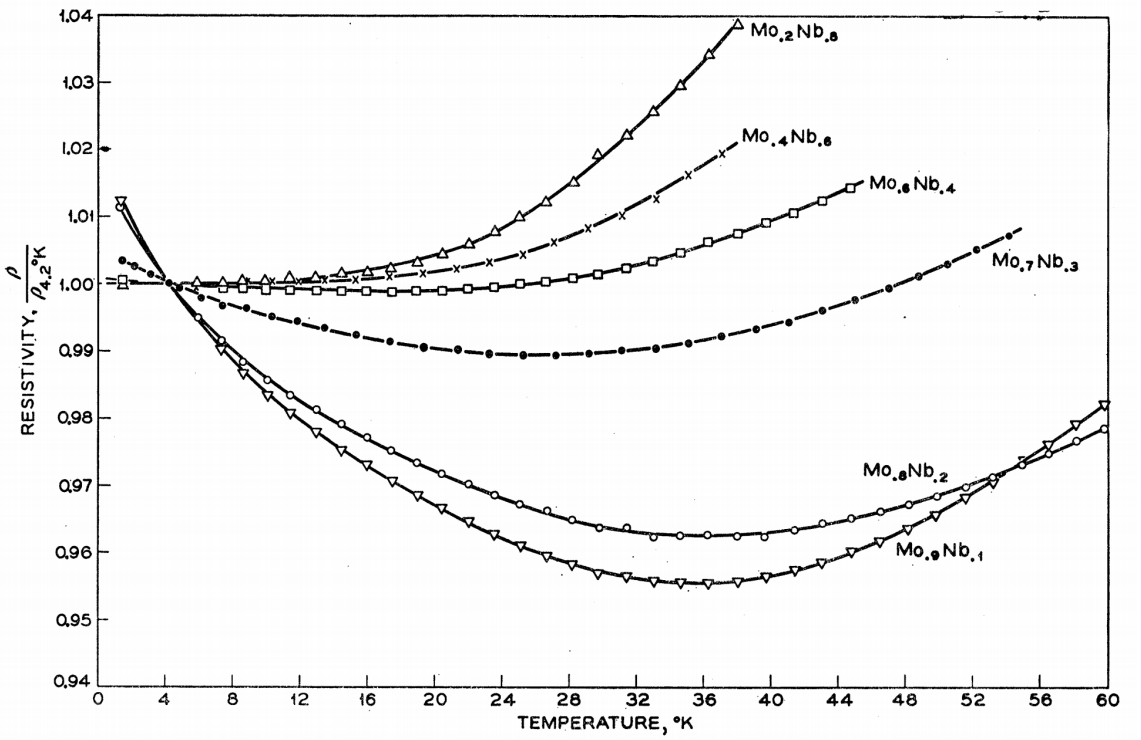

Figure 2.1: The temperature dependence of resistivity measured in $(Mo_xNb_{1-x})_{0.99}Fe_{0.01}$ from Ref. [1]. The resistivity is rescaled at 4.2K.

suggested that resistivity minimum does not come from the interactions between magnetic impurities, but is an effect due to interactions between the conducting electrons and magnetic impurities.

The magnetic moments originate from the localization of the electrons that are unpaired in the atomic or ionic d or f shell. At low temperatures, the high frequency excitations are eliminated and the only degree of freedom is the magnetic moment. The *Curie-Weiss law* describes such a system composed of magnetic moments with the magnetic susceptibility

$$\chi = \frac{C}{T - T_c}, \tag{2.3}$$

where C is a material specific constant and T_c is the Curie temperature. A positive

T_c reflects antiferromagnetic interactions between spins while a negative T_c indicates ferromagnetic interactions. Earlier than Jun Kondo, Philip W. Anderson formulated a later called *Anderson model* where he found the interaction between the local magnetic moments and the itinerant electrons in metals is antiferromagnetic [13]. Later the antiferromagnetic interaction was confirmed in Kondo's work [11].

In this model, the resistivity contribution from the electron-impurity interaction was calculated to be

$$R_{\text{imp}}^{\text{spin}} = \frac{3\pi m J^2 S(S+1)}{2e^2\hbar\epsilon_{\text{F}}}\left(1 - 4J\rho_0\left(\epsilon_{\text{F}}\right)\ln\left(\frac{k_{\text{B}}T}{D}\right)\right), \tag{2.4}$$

where D is the half band width [11, 14]. For an antiferromagnetic coupling $J > 0$, the J^3 term increase as $\ln T$ when lowering the temperature. The total resistivity is

$$R(T) = aT^5 + c_{\text{imp}}R_0 - c_{\text{imp}}R_1\ln\left(\frac{k_{\text{B}}T}{D}\right), \tag{2.5}$$

where c_{imp} is the density of magnetic impurities, the first term is the contribution from phonon, the second term is the contribution from impurities, the third term comes from the interactions between conduction electrons and local magnetic moments. The resistivity has a minimum at

$$T_{\text{min}} = \left(\frac{R_1}{5a}\right)^{1/5} c_{\text{imp}}^{1/5}. \tag{2.6}$$

The result fits the data well for dilute AuFe alloys.

On the other hand, the result also defines the Kondo temperature

$$T_K = De^{-1/(2J\rho)} \tag{2.7}$$

below which the physics is roughly dominated by electron-impurity coupling. The resistivity above diverges logarithmically in the low temperature regime ($T < T_K$). Gaining understanding in this regime became the famous *Kondo problem* which inspired significant theoretical investigations and developments. The problem was finally solved by Kenneth G. Wilson using numerical renormalization group [15].

Over the last 50 years, the Kondo model has become one of the most fundamental models in condensed matter physics and the playground for theoretical and numerical methods.

2.2 The Kondo Lattice Model and Heavy Fermion Materials

In the Kondo model, the magnetic impurity is on a single site. It is tempting to think of a lattice of these magnetic impurities on each site. Such a model with massive local magnetic moments is called the *Kondo lattice model*. This is the model that this chapter and some of the following chapters are built on.

The Hamiltonian of the Kondo lattice model can be written as

$$\mathcal{H} = \sum_{\mathbf{k}\sigma} \varepsilon_{\mathbf{k}} c^{\dagger}_{\mathbf{k}\sigma} c_{\mathbf{k}\sigma} + J \sum_{i} \mathbf{S}_i \cdot \mathbf{s}_i, \tag{2.8}$$

where $\mathbf{S}_i$ is the local magnetic moment at position i. The tight-binding form of a Kondo lattice model is

$$\mathcal{H} = -t \sum_{\langle i,j \rangle} \sum_{\sigma=\uparrow,\downarrow} \left(c^{\dagger}_{i,\sigma}\, c_{j,\sigma} + \text{h.c.} \right) + J \sum_{i} \mathbf{S}_i \cdot \mathbf{s}_i, \tag{2.9}$$

where $c^{\dagger}_{i,\sigma}$ is the creation operator of electrons at site i with spin σ, $\langle i, j \rangle$ represents

nearest neighbor sites, t is the nearest-neighbor hopping constant, J is the coupling strength, $\mathbf{S}_i$ is local magnetic moment, and

$$\mathbf{s}_i = \sum_{\alpha,\beta} c^\dagger_{i\alpha} \boldsymbol{\sigma}_{\alpha\beta} c_{i\beta}, \tag{2.10}$$

is the spin of the conduction electron.

The Kondo lattice model can also be viewed as transformed from the periodic Anderson model. The Hamiltonian is

$$\begin{aligned} \mathcal{H}_{\text{PAM}} = -t \sum_{\langle i,j \rangle} \sum_{\sigma} \left(c^\dagger_{i,\sigma} c_{j,\sigma} + \text{h.c.} \right) + \sum_{i,\sigma} \varepsilon_f n^f_{i,\sigma} \\ + V \sum_{i,\sigma} \left(c^\dagger_{i,\sigma} f_{i,\sigma} + h.c. \right) + U \sum_i n^f_{i,\uparrow} n^f_{i,\downarrow}, \end{aligned} \tag{2.11}$$

where $n_{i,\sigma} = c^\dagger_{i,\sigma} c_{i,\sigma}$ is the conducting electron number operator, $n^f_{i,\sigma} = f^\dagger_{i,\sigma} f_{i,\sigma}$ is the local spin number operator, ε_f is atomic energy of the f level, V mixes the electrons in two orbitals, U is the Coulomb repulsion between f electrons [8]. It is important to note that there is no Hund's rule coupling since the orbital degeneracy is ignored. In the Kondo regime, unpaired f electrons have lower energy than the conduction band and thus can be treated as local moments. The periodic Anderson model can be reduced to a Kondo lattice model as in Eq. 2.8 and Eq. 2.9 with the coupling strength $J = 8V^2/U$ [8].

Another important mechanism for the local moments is the Ruderman-Kittel-Kasuya-Yosida (RKKY) interaction [16, 17, 18], which explains the indirect long-range interactions between local moments mediated by itinerant electrons. The RKKY interaction has an energy scale [9]

$$E_{RKKY} = J^2 \rho. \tag{2.12}$$

The physics of heavy fermion materials is determined by the competition of Kondo effect and the RKKY interaction.

In the Hamiltonian of Kondo lattice model, if the coupling between the local moments and the itinerant electrons is ferromagnetic, the model becomes *double-exchange model* or *ferromagnetic Kondo lattice model*, which describes another mechanism in a class of material called *manganites*. Since it is more relevant to the following chapters, we will introduce it later.

2.3 Tensor Networks

Various numerical methods have been applied to study the Kondo lattice model. Here we introduce methods based on tensor networks.

Tensor network is a geometric architecture composed of tensors connected by bonds to represent quantum states. The last two decades have witnessed the exploding development of tensor networks. It lays a solid basis for some powerful simulation algorithms for condensed matter systems. In a tensor network, each node is a multidimensional tensor with open and/or contracted indices. They are linked by bonds to form a tensor network to represent a quantum state. An accurate representation usually results in large dimensions of the tensors, or equivalently the bond dimensions (dimensions of the bonds). Then the size of tensor network state for a generic system grows exponentially with the system size. However, thanks to the area law, lots of low lying states of the systems of interest can be exactly or almost exactly represented by tensor networks with restricted bond dimensions. This is where the efficiency of some tensor network algorithms is rooted in.

Numerical methods based on tensor networks has seen a rapid growth since the invention of density matrix renormalization group (DMRG) by Steve White in

1992 [19, 20]. Its connection with tensor networks, or more specifically matrix product states, was found later in Ref. [21, 22, 23, 24]. DMRG has become one of dominating methods for studying low dimensional, especially one dimensional lattice systems. It is widely used in calculating the ground state or other low lying states and gives essentially numerical exact results. For the dynamics, time evolution block decimation (TEBD) and some other methods have been developed. In this chapter, we present an introduction to tensor networks, DMRG and TEBD and apply TEBD to study the quench dynamics of Kondo lattice model.

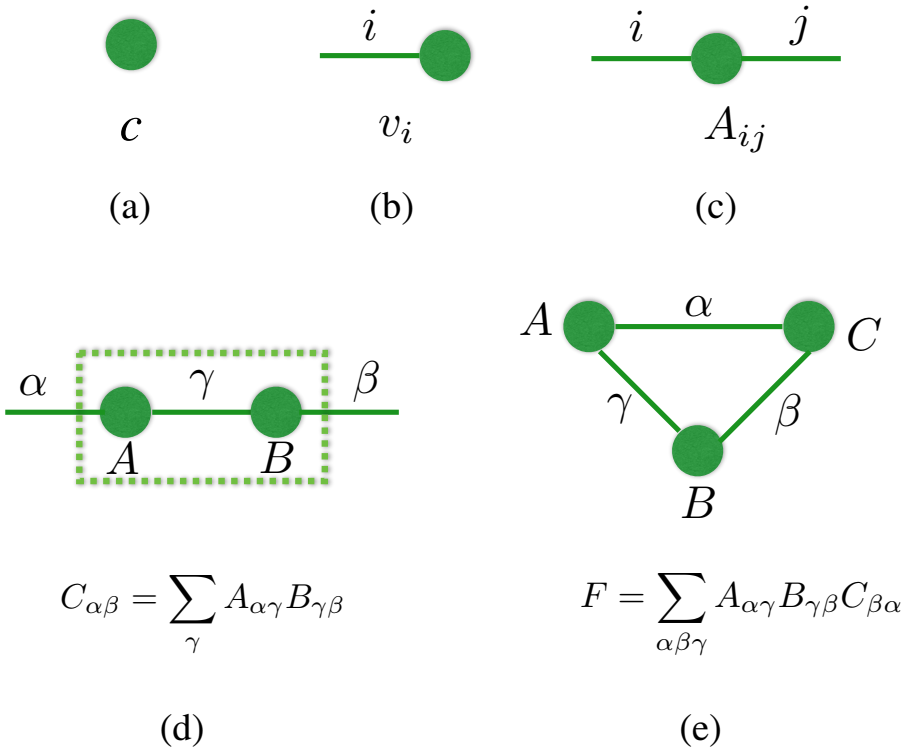

Figure 2.2: Graphic representations of (a) a rank-0 tensor (scalar), (b) rank-1 tensor (vector), (c) rank-2 tensor (matrix), (d) matrix product of two rank-2 tensors, (e) trace of 3 rank-2 tensors.

Tensors are the building blocks of tensor networks. We illustrate the graphic representation of tensor networks in Fig. 2.2. Each circle represents a tensor with connected lines (bonds) being the indices for the tensor. The number of lines is

the rank of the tensor. The actual values for entries in the tensor are hidden in the graphic representation until being used in computation or calculation. Fig. 2.2 (a) (b) (c) represents a rank-0 tensor (scalar), rank-1 tensor (vector), rank-2 tensor (matrix) respectively. In the connected tensors, we perform a summation (contraction) over the connecting indices. Thus, the product of matrix A and matrix B, namely,

$$C_{\alpha\beta} = \sum_{\gamma} A_{\alpha\gamma} B_{\gamma\beta} \tag{2.13}$$

can be represented in Fig. 2.2 (d). This process is usually named *contraction*. Similarly, trace of tensors (matrices), for an example,

$$F = \sum_{\alpha\beta\gamma} A_{\alpha\gamma} B_{\gamma\beta} C_{\beta\alpha} \tag{2.14}$$

can be represented Fig. 2.2 (e).

A tensor network is connected network composed of these tensors.

2.3.1 Tensor network states

Each quantum state can be expressed as a vector in the Hilbert space. Consider a spin-$\frac{1}{2}$ σ, the Hilbert space has a dimension of 2 with a basis $\{|\uparrow\rangle, |\downarrow\rangle\}$. For a many-body state, the Hilbert space is then spanned by the tensor products of the bases in the local Hilbert spaces. A quantum many-body state can be written as

$$|\Psi\rangle = \sum_{\sigma_1\sigma_2\cdots\sigma_N} C_{\sigma_1\sigma_2\cdots\sigma_N} |\sigma_1\rangle |\sigma_2\rangle \cdots |\sigma_N\rangle \tag{2.15}$$

where $|\psi_i\rangle$ is a local state on site i, and $C_{\sigma_1\sigma_2\cdots\sigma_N}$ constitute a set of coefficients.

Tensor networks can be used to represent quantum states, called *tensor network*

states. A generic tensor network state is shown in Fig. 2.3 (a) with N open indices. Each index represents a physical local dimension σ_i. The internal structure of tensor network states are specified in practical use cases. For example, in matrix product states (MPS) as illustrated in Fig. 2.3 (b), we use N rank-3 tensors to represent N sites in the system. Each tensor has an open physical index and two bonds connected with two neighboring tensors. If the boundary is open, the tensors on the boundary have a rank of 2 instead of 3. MPS is used for one-dimensional systems, sometimes also applied in two-dimensional systems. $C_{\sigma_1\sigma_2\cdots\sigma_N}$ could be calculated explicitly by contracting the tensors (making products of matrices in the MPS case). The geometric structure of a tensor network state varies, often mimicking the geometry of the lattice structure or the interactions between sites. Apart from matrix product states, projected entangled pair states (PEPS) in Fig. 2.3 (c) are also frequently used for two dimensional systems.

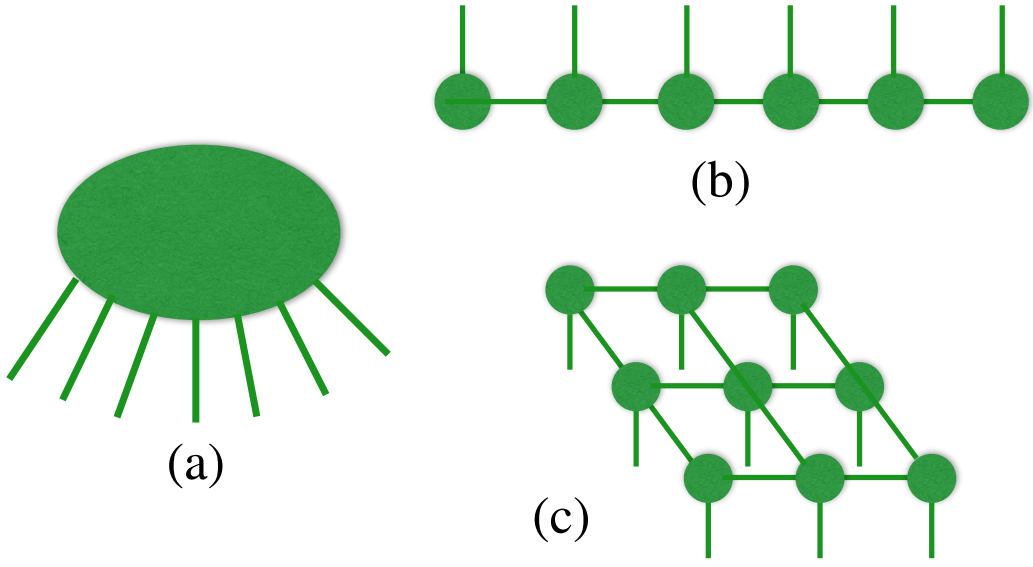

Figure 2.3: Graphic representations of representative tensor network states: (a) a generic tensor network state, (b) matrix product states (MPS) with periodic boundary condition and (c) projected entangled pair states (PEPS).

2.3.2 Matrix product states

We will be using matrix product states for our investigations in this chapter. Consider a one-dimensional quantum spin system with local Hilbert space dimension d, the state of such a system can be represented as a matrix product state in Fig. 2.4. Each tensor in the MPS takes open or closed indices. The open indices are the physical

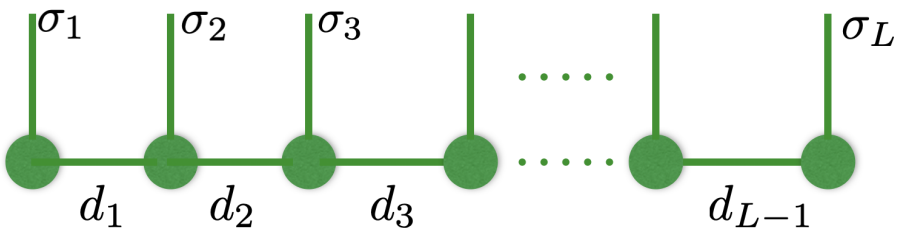

Figure 2.4: A schematic diagram of matrix product states. σ_i's are the physical indices. d_i's are the bond dimensions.

indices that represent the physical components and the closed indices indicate where the tensors should be contracted. The state in Fig. 2.4 is

$$|\psi\rangle = \sum_{\sigma_1,\cdots,\sigma_L} M_1^{\sigma_1} M_2^{\sigma_2} \cdots M_L^{\sigma_L} |\sigma_1\sigma_2\cdots\sigma_L\rangle \tag{2.16}$$

where σ_i is the direction of spin on site i, M_i is the rank-3 tensor at site i, $M_i^{\sigma_i}$ is a matrix for the corresponding local state σ_i with dimension $d_{i-1} \times d_i$, $|\sigma_1\sigma_2\cdots\sigma_L\rangle$ is a vector of the basis. For each $|\sigma_1\sigma_2\cdots\sigma_L\rangle$, the matrix product $M_1^{\sigma_1} M_2^{\sigma_2} \cdots M_L^{\sigma_L}$ yields a number. The state $|\psi\rangle$ can thus be explicitly represented by computing d^L such numbers.

The MPS representation for a state is not unique, it is possible to do a gauge transformation on the MPS and keep the state the same. The gauge transformation can be completed by inserting a matrix G and its inverse G^{-1} in a bond, and incorporating (contracting) them to the left and right tensors respectively.

Each bond bipartition the system into two parts with size N_L on the left and $N_R = N - N_L$ on the right, namely,

$$|\psi\rangle = \sum_{i=1}^{\dim \mathcal{H}_L} \sum_{j=1}^{\dim \mathcal{H}_R} A_{ij} \, |u_i\rangle_L \, |v_j\rangle_R \tag{2.17}$$

where $|u_i\rangle_L$ and $|v_j\rangle_R$ are the basis for the left and right systems respectively, A_{ij} is the corresponding coefficient, the dimensions of the Hilbert spaces $\dim \mathcal{H}_L = d^{N_L}$ and $\dim \mathcal{H}_R = d^{N_R}$ for a generic state. Considering the tensor representation, we are essentially looking for matrices M_L and M_R such that $A = M_L M_R$. M_L has dimension $d^{N_L} \times d_{N_L}$ and M_R has dimension $d_{N_L} \times d^{N_R}$. The bond dimension between the left and right systems is $d_{N_L} = \min\{d^{N_L}, d^{N_R}\}$. Consequently, to precisely represent a generic state, the bond dimension d_i grows exponentially as d^i from either end of the chain to the middle. d_i becomes very big in the middle of the chain, but it is not necessary for most states of interest. These states are compressible using singular value decomposition.

For a general matrix A of dimension $m \times n$ and $k = \min\{m, n\}$, a *singular value decomposition* (SVD) is written as

$$A = USV^\dagger, \tag{2.18}$$

where U is a $m \times k$ matrix that has $U^\dagger U = I$, V is a $k \times n$ matrix that satisfy $VV^\dagger = I$, and S is $k \times k$ diagonal matrix with *singular values* $s_1 \geqslant s_2 \geqslant s_3 \geqslant \cdots \geqslant s_k \geqslant 0$. The number of positive singular values is equal to the rank of A.

After the singular value decomposition, we have

$$A_{ij} = \sum_{\alpha=1}^{r} U_{i\alpha} s_\alpha V^*_{j\alpha}. \tag{2.19}$$

By a unitary transformation defined by U and V, we could form a new set of basis for the system and write the state as

$$|\psi\rangle = \sum_{\alpha=1}^{r} s_\alpha |\alpha\rangle_L |\alpha\rangle_R \tag{2.20}$$

where r is the rank of matrix A and the new basis is

$$\begin{aligned} |\alpha\rangle_L &= \sum_{i=1}^{\dim \mathcal{H}_L} U_{i\alpha} |i\rangle_L \\ |\alpha\rangle_R &= \sum_{j=1}^{\dim \mathcal{H}_R} V^*_{j\alpha} |j\rangle_R \end{aligned} \tag{2.21}$$

Thus we should be able to reduce the bond dimension to r. More technical details can be found in [25, 7].

Another important aspect about tensor network states is normalization. Performing singular value decompositions using the full matrix is computationally expensive. It turns out we could iteratively keep the matrix product states left-canonical and right-canonical about a bond while performing calculations. This is called the mixed canonical form. As a result, we only need to operate on the tensors on sites connected by the bond, which greatly reduces computational efforts.

The singular value decomposition also gives the entanglement entropy of the subsystems conveniently. The reduced density matrix for the left and right subsystems are

$$\rho_L = \mathrm{tr}_R \left|\psi\right\rangle \left\langle\psi\right| = \sum_{\alpha=1}^{r} s_\alpha^2 \left|\alpha\right\rangle_L \left\langle\alpha\right|_L \tag{2.22}$$

$$\rho_R = \mathrm{tr}_L \left|\psi\right\rangle \left\langle\psi\right| = \sum_{\alpha=1}^{r} s_\alpha^2 \left|\alpha\right\rangle_R \left\langle\alpha\right|_R \tag{2.23}$$

The entanglement entropy is

$$S_{N_L}(|\psi\rangle) = -\operatorname{tr}_A \rho_A \ln \rho_A = -\operatorname{tr}_B \rho_B \ln \rho_B = -\sum_{\alpha=1}^{r} s_\alpha^2 \ln s_\alpha^2 \tag{2.24}$$

In general, if the entanglement entropy is low, that means more singular values are 0, so a relatively low bond dimension is sufficient to provide an almost numerically exact result. During the SVD, if some singular values are very small, we could also remove these values and rescale the remaining singular values. This is *truncation*. The necessary bond dimension grows exponentially with the entanglement entropy between the left and right subsystem divided by the bond.

One of the advantages of matrix product states is that DMRG becomes easily extendable to more complicated systems and problems in this language. It is also understood that the reason behind the strength of DMRG and related numerical methods is that the low lying states of most of Hamiltonians of interest obey the celebrated *area law*. For area law states, the entanglement entropy does not scale as the volume of the system, but grow with the size of the surface. For such states in 1D systems, the area of the intersections is constant. Consequently, the entanglement entropy can only grow to an upper bound, which means the bond dimension of the matrix product state has an upper limit, making the operations on the MPS more practical.

One of the most popular and interesting examples for matrix product states is the Affleck-Kennedy-Lieb-Tasaki (AKLT) state. We present its MPS form in Appendix B.1.

2.3.3 Matrix product operators

An operator can also be represented in a tensor network form, named *matrix product operator* (MPO), where each tensor has two open indices. A generic operator for a system of size L can be written as

$$O = \sum_{\{\sigma\}} \sum_{\{\sigma'\}} C_{\sigma_1 \dots \sigma_L, \sigma'_1 \dots \sigma'_L} |\sigma_1 \dots \sigma_L\rangle \langle \sigma'_1 \dots \sigma'_L| \tag{2.25}$$

To represent it as a matrix product operator, we write

$$O = \sum_{\{\sigma_i, \sigma'_j\}} M^{\sigma_1 \sigma'_1} M^{\sigma_2 \sigma'_2} \dots M^{\sigma_L \sigma'_L} |\sigma_1 \dots \sigma_L\rangle \langle \sigma'_1 \dots \sigma'_L| \tag{2.26}$$

Fig. 2.5 is an example of a matrix product operator Eq. 2.25 for a one-dimensional spin system.

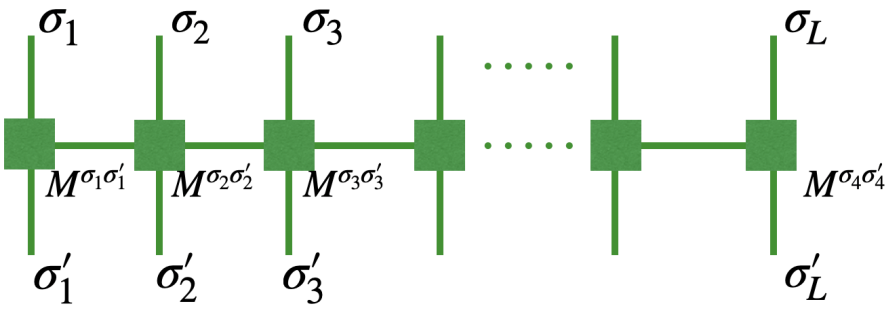

Figure 2.5: A schematic diagram of matrix product operators, with σ_i, σ'_i the local indices and d_i the bond dimensions (not shown in the figure).

There is a systematic way of constructing short-ranged Hamiltonians with minimized bond dimensions almost automatically [25]. We show an example of constructing the MPO of Heisenberg Hamiltonian from Ref. [7] in B.2.

2.4 Tensor Network Algorithms: DMRG and TEBD

2.4.1 Density matrix renormalization group (DMRG)

Density matrix renormalization group (DMRG) can be viewed as a variational method based on MPSs. We introduce DMRG following Ref. [7]. To find the ground state for a 1D system, we could start with a random state $|\psi\rangle$ and keep varying it until we reach a good approximation. During the process, we are minimizing the energy of the state [7],

$$E = \frac{\langle\psi|H|\psi\rangle}{\langle\psi|\psi\rangle}. \tag{2.27}$$

Minimizing it is equivalent to minimizing

$$\langle\psi|H|\psi\rangle - \lambda\langle\psi|\psi\rangle. \tag{2.28}$$

In the language of tensor networks, we could represent Eq. 2.28 as Fig. 2.6. Then,

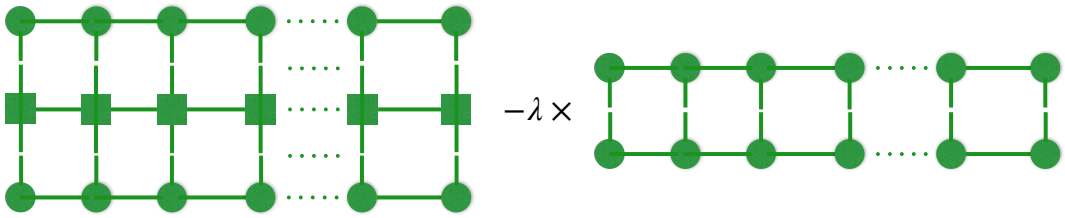

Figure 2.6: Density matrix renormalization group: minimizing the variational function.

for each site i, we just need to solve an equation

$$\frac{\partial}{\partial M^{\sigma_{i^*}}}(\langle\psi|H|\psi\rangle - \lambda\langle\psi|\psi\rangle) = 0 \tag{2.29}$$

which is represented as Fig. 2.7.

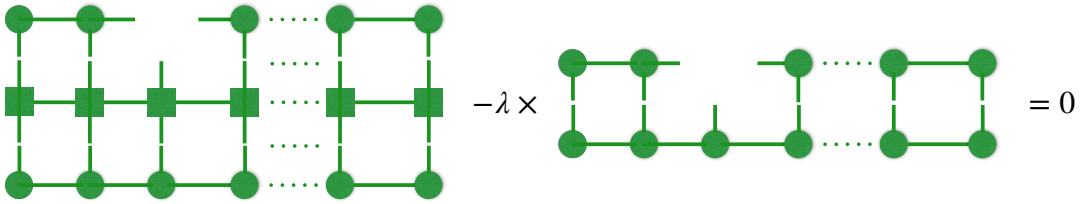

Figure 2.7: Density matrix renormalization group: solving an equation.

If the MPS is normalized both on the left and right sides (mixed canonical form), we could simplify it as Fig. 2.8.

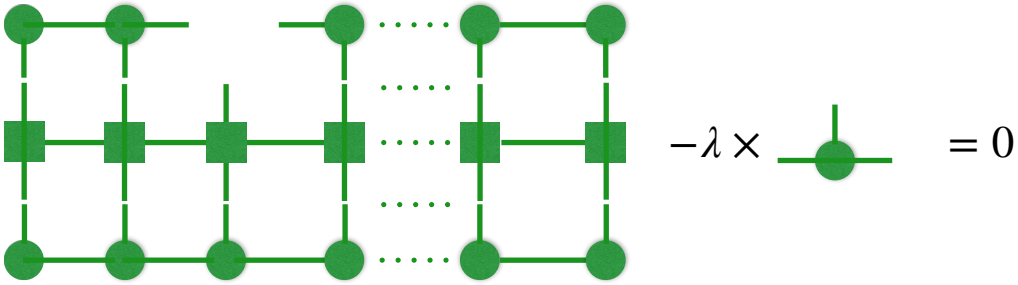

Figure 2.8: Density matrix renormalization group: eigenvalue problem.

This is an eigenvalue problem

$$H_i M = \lambda M, \tag{2.30}$$

where H_i is illustrated in Fig. 2.9. Now we just need to solve this eigenvalue problem

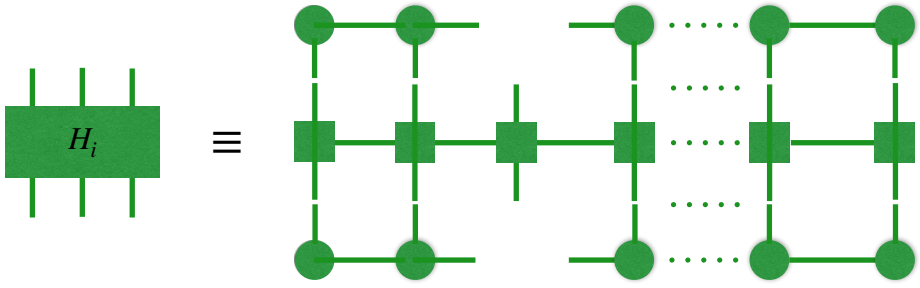

Figure 2.9: Density matrix renormalization group: H matrix.

and take M corresponding to the smallest λ. After updating M, we continue to apply the same procedure to the next site.

We summarize the procedures of DMRG as follows. (1) Prepare a MPS for the system to start with. This MPS could be random or any other state that is adequate to reach the ground state under DMRG. (2) Sweep each bonds from one end to the other end while keeping the MPS in a mixed canonical form. On each bond, solve a eigenvalue problem to update the MPS. Reduce the bond dimension if necessary in the process. (3) Repeat step (2) until the energy and entropy converges. In practice, for some systems, converging results can be obtained within only a few sweeps. More technical details can be found in Ref. [25, 7]. To optimize, we could work on specific sectors defined by quantum numbers of the system.

There are some tensor network packages developed in the recent decade, such as ITensor [26]. We use ITensor for tensor network calculations in this thesis.

2.4.2 Time evolution blocking decimation (TEBD)

Using the matrix product states, we can also simulate dynamics in a straightforward way. The method is *time evolution blocking decimation* (TEBD) [27]. For a generic system, the time evolved state is the initial state applied by the time evolution operator e^{-iHt}, namely $|\psi(t)\rangle = \mathrm{e}^{-\mathrm{i}Ht}|\psi(0)\rangle$. Explicitly evolving the state in the language of tensor network states is computationally expensive and usually intractable. We could take advantage the fact that most of Hamiltonians of interest only involves nearest-neighbor or short range interactions. The basic idea of this algorithm is to break down the Hamiltonian into nearest-neighbor pieces and apply one small piece of the Hamiltonian with a small time interval each time. Applying an operator on a MPS generally increases the bond dimension by a few times, so we do singular value decomposition to compress the state simutanously.

Specifically for the one-dimensional Kondo lattice model, we write the Hamiltonian as

$$H = \sum_{i=1}^{L} h_i, \tag{2.31}$$

where

$$h_i = -t \sum_{\sigma} \left(c^{\dagger}_{i,\sigma} c_{i+1,\sigma} + c^{\dagger}_{i+1,\sigma} c_{i\sigma} \right) - J \mathbf{S}_i \cdot \mathbf{s}_i. \tag{2.32}$$

We also break the total evolving time to smaller $\tau = t/N$. τ is small enough that the time evolution operator can be Trotter decomposed as

$$e^{-iH\tau} = e^{-i\sum_{i=1}^{L-1} h_i \tau} \approx e^{-ih_1\tau} e^{-ih_2\tau} e^{-ih_3\tau} \dots e^{-ih_{L-1}\tau} \tag{2.33}$$

Higher order of the Trotter decomposition is also possible if higher precision is necessary. Time evolved state $|\psi(\tau)\rangle$ at time τ can be found by applying the small pieces $e^{-ih_i\tau}$ consecutively on the MPS from one end to the other end until arriving at the final state. $|\psi(t)\rangle$ can be obtained by repeating this process and performing singular value decomposition to compress the states simultaneously.

2.5 The Phase Diagram of 1D Kondo Lattice Model

The phase diagram of the one-dimensional Kondo lattice with $S = \frac{1}{2}$ localized quantum spins has been studied in Ref. [2]. To keep the notation consistent with that in their work, we rewrite the Hamiltonian as follows,

$$\mathcal{H} = -t \sum_{\langle i,j \rangle, \sigma} c^{\dagger}_{i\sigma} c_{j\sigma} - J \sum_{i} \vec{S}_i \cdot \vec{\sigma}_i. \tag{2.34}$$

Here we change the sign in front of J to incorporate their results. The local electron Hilbert space is spanned by states with zero, one spin up, one spin down or two electrons, represented as $|\emptyset\rangle$, $|\uparrow\rangle$, $|\downarrow\rangle$, and $|\updownarrow\rangle$, the dimension is 4. The local spins contribute to another dimension of 2 ($|\Uparrow\rangle$ and $|\Downarrow\rangle$). So the total local Hilbert space dimension is 8. It is spanned by

$$|\emptyset \Uparrow\rangle, |\uparrow\Uparrow\rangle, |\downarrow\Uparrow\rangle, |\updownarrow\Uparrow\rangle, |\emptyset \Downarrow\rangle, |\uparrow\Downarrow\rangle, |\downarrow\Downarrow\rangle, |\updownarrow\Downarrow\rangle. \tag{2.35}$$

Local operators are then specified in our program by defining their matrix elements under the local basis. For example, in the case of $c^\dagger_{i\uparrow}$, we have $\langle\uparrow\Uparrow| c^\dagger_{i\uparrow} |\emptyset \Uparrow\rangle = 1$, $\langle\updownarrow\Uparrow| c^\dagger_{i\uparrow} |\downarrow\Uparrow\rangle = 1$, $\langle\uparrow\Downarrow| c^\dagger_{i\uparrow} |\emptyset \Downarrow\rangle = 1$, $\langle\updownarrow\Downarrow| c^\dagger_{i\uparrow} |\downarrow\Downarrow\rangle = 1$ and all other matrix elements are 0.

The authors [2] applied the finite size DMRG on the 1D chain of 36 sites for several commensurate electron filling fractions with either ferromagnetic ($J > 0$) or antiferromagnetic ($J < 0$) couplings. The ground state phase diagram is presented in Fig. 2.10. In the figure, n is the average number of itinerant electrons per site.

For relatively smaller Hund's or Kondo couplings in some regions, there exists the so-called island phase, characterized by a prominent wavevector $q = 2k_F = n\pi$. They also found that the island phase transits to a ferromagnetic phase for stronger couplings, through a "spiral" phase. This "spiral" phase is characterized by incommensurate values of q's and short range correlations.

Phase separation emerges on the top right corner with electron density close to $n = 1$ and strong Hund's coupling. This is consistent with our results on the square lattice double exchange model with classical local spins in chapter 4. When the electron density $n = 1$, it becomes a spin liquid.

To characterize the phases, we calculate some parameters of the obtained ground

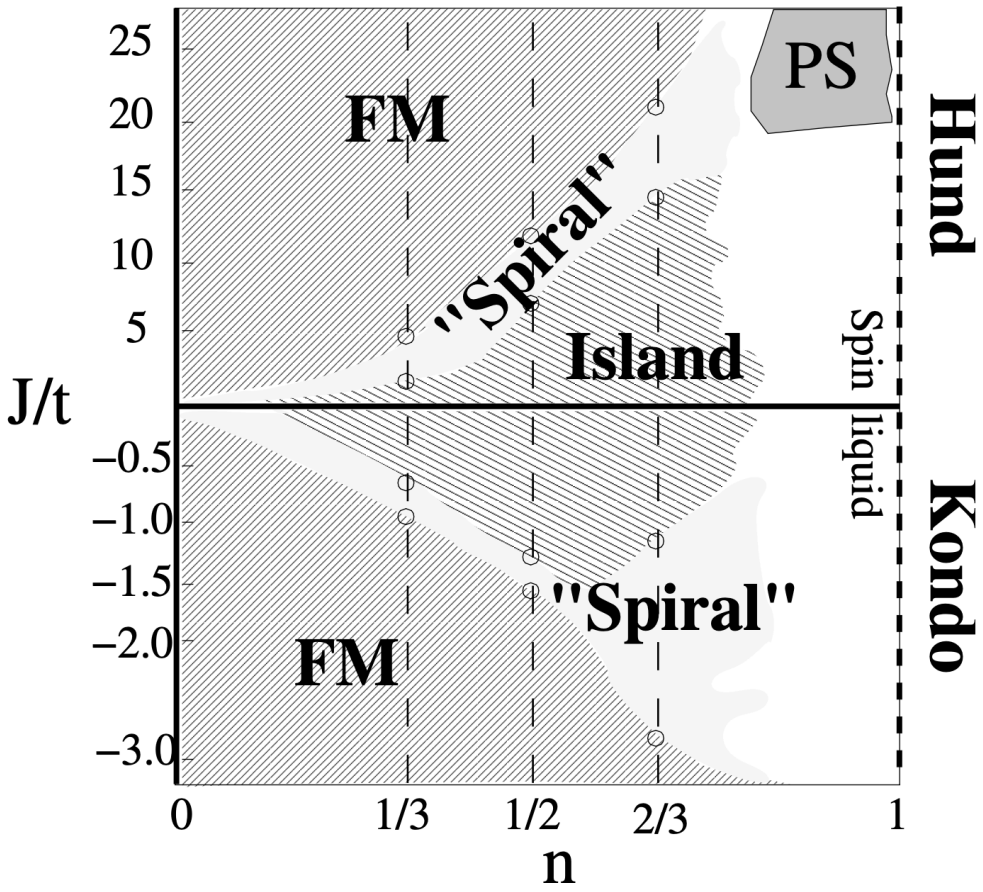

Figure 2.10: The ground state phase diagram of the 1D Kondo lattice model with 36 sites and commensurate electron fillings obtained using DMRG in Ref. [2].

state obtained using DMRG. These quantities can all be implemented in the language of MPSs and MPOs. The first quantity we want to calculate is the average spin-spin correlation

$$C(d) = \frac{1}{L-d} \sum_i \left\langle \vec{S}_i \cdot \vec{S}_{i+d} \right\rangle , \tag{2.36}$$

and the background removed correlation

$$C'(d) = \frac{1}{L-d} \sum_i \left\langle \vec{S}_i \cdot \vec{S}_{i+d} \right\rangle - \left\langle \vec{S}_i \right\rangle \cdot \left\langle \vec{S}_{i+d} \right\rangle . \tag{2.37}$$

We also calculate the spin structure factor

$$S(q) = \frac{1}{L} \sum_{i,j} e^{iq(R_j - R_i)} \left\langle \vec{S}_i \cdot \vec{S}_j \right\rangle . \tag{2.38}$$

As comparisons, we also show spin correlations with the spin in the middle $\left\langle \vec{S}_i \cdot \vec{S}_{L/2} \right\rangle$, nearest-neighbor spin correlations $\left\langle \vec{S}_i \cdot \vec{S}_{i+d} \right\rangle$, and $\langle S_i^z \rangle$ for local spins. For the electrons, the expected number of up and down electrons, $\langle n_{i,\uparrow} \rangle = c_{i\uparrow}^\dagger c_{i\uparrow}$, $\langle n_{i,\downarrow} \rangle = c_{i\downarrow}^\dagger c_{i\downarrow}$ and $\langle n_i \rangle = \langle n_{i,\uparrow} \rangle + \langle n_{i,\downarrow} \rangle$ on each site. We also calculate $\langle S_i^{e,z} \rangle = \frac{1}{2} \left(\langle n_{i,\uparrow} \rangle - \langle n_{i,\downarrow} \rangle \right)$ and $\left\langle S_i^{tot,z} \right\rangle = \langle S_i^{e,z} \rangle + \langle S_i^z \rangle$.

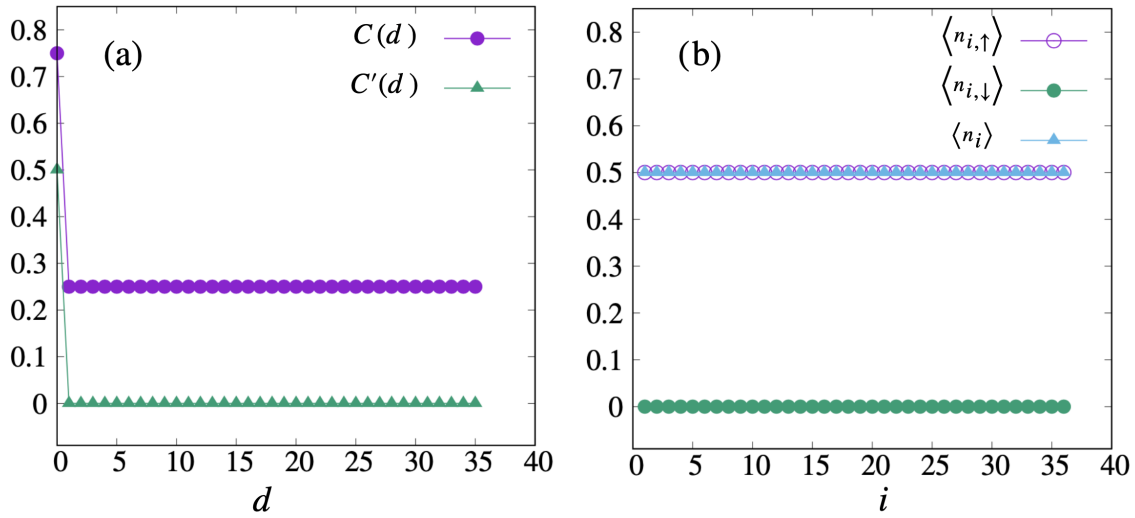

Figure 2.11: The ferromagnetic ground state phase of the double exchange model with $N = 36, N_f = 18, J = 20$. (a) shows the correlation and the background removed correlation of spins with distance d apart. (b) shows the expected number of up and down electrons, $\langle n_{i,\uparrow} \rangle$, $\langle n_{i,\downarrow} \rangle$ and total number of electrons $\langle n_i \rangle = \langle n_{i,\uparrow} \rangle + \langle n_{i,\downarrow} \rangle$ on each site.

In the Hund's coupling regime of the phase diagram, a large portion is ferromagnetic ground state at large J, especially when the density of electrons is low. We pick $N = 36$, $n = 0.5$, number of electrons $N_f = 18$ and $J = 20$, the phase is characterized in Fig. 2.11. With a dominating J, the spins are aligned perfectly in the

same direction. Each local spin align with the electron to form a triplet state $S = 1$. The expected number of $|\uparrow\rangle$ electrons is also distributed almost uniformly in the 1D lattice.

On the other hand, when $J = 2, n = 0.5$, the ground state is a "island phase", as illustrated in Fig. 2.12. The spin order at $q = \pi/2$ in (b) becomes significant and thus we can see a zigzag 4-site periodic pattern in the spin-spin correlation (a). The spin correlation with central site also show this periodicity in (c); the neighboring site spins also exhibits a strong correlation and the 4-site periodic pattern in (d). In (e), we see the expectation of the total spin tends to be 0. Contrary to the ferromagnetic case, the electron density plot in (f) does not show difference between $|\uparrow\rangle$ and $|\downarrow\rangle$ electrons. In addition, the electron density is almost uniform in the bulk.

These are the two states that we will study the dynamics on. More detailed studies on the phase diagrams can be found in Ref. [2]. It is worth noting that the phase diagrams of 1D Kondo lattice model have been studied using various methods, but the phase diagram itself is not the main focus of our research.

2.6 Quench Dynamics of 1D Kondo Lattice Model

In this section, we apply the TEBD algorithm on the Kondo lattice model to study its quench dynamics. We consider the system with a representative filling (quarter filling) at $n = 1/2$. For the dynamics, we can prepare the initial state as the ground state of the model at some coupling strength J using DMRG, and then immediately quench it on the system with a different J. Snapshots of the evolved states for different time steps obtained using TEBD are saved for analysis. Due to the linearly increasing entanglement entropy, we could only simulate a system with size $L = 24$.

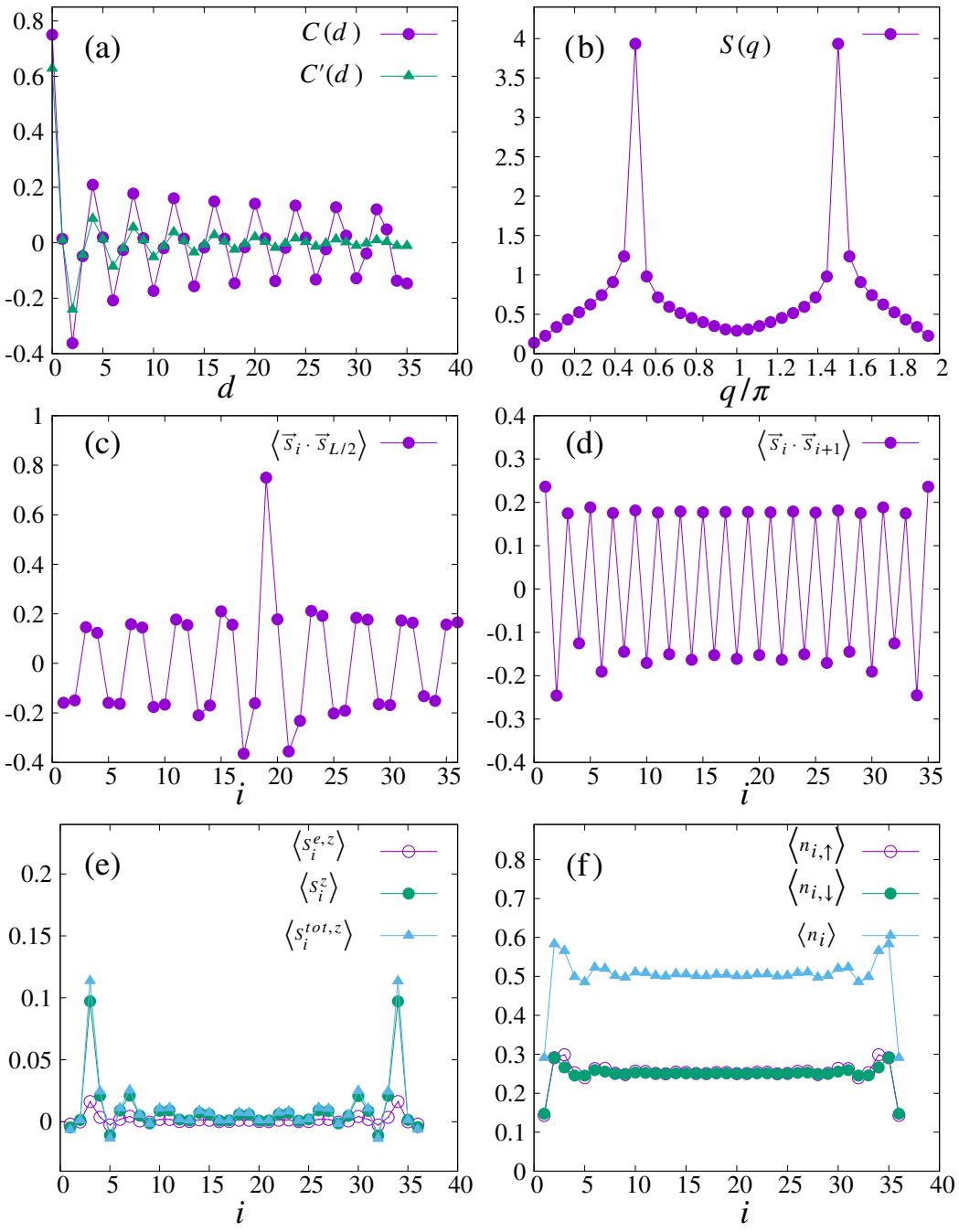

Figure 2.12: The Island ground state phase of the double exchange model with $N = 36, N_f = 18, J = 2$. (a) shows the correlation and the background removed correlation of spins with distance d apart. (b) is the structure factor. (c) is the spin correlation with the central site. (d) is the correlation between neighboring spins. (e) is the expectation of electron spin $\langle S_i^{e,z} \rangle$, local spin $\langle S_i^z \rangle$, and total spin $\langle S_i^{tot,z} \rangle = \langle S_i^{e,z} \rangle + \langle S_i^z \rangle$ on each site. (e) shows the expected number of up and down electrons, $\langle n_{i,\uparrow} \rangle$, $\langle n_{i,\downarrow} \rangle$ and total number of electrons $\langle n_i \rangle = \langle n_{i,\uparrow} \rangle + \langle n_{i,\downarrow} \rangle$ on each site.

We simulate the quench dynamics between the island state at $J = 2$ and ferromagnetic state at $J = 20$. For the quench of the ferromagnetic ground state at $J = 20$ under the Hamiltonian with $J = 2$, we observe that the state stays exactly the same across the quench. This indicates that the ferromagnetic ground state is an eigenstate of the island phase Hamiltonian.

On the other hand, the quench of the island state at $J = 2$ under the Hamiltonian with $J = 20$ yields more interesting phenomenon. To characterize some features, we define the Loschmidt rate $\langle\psi\left|e^{-iHt}\right|\psi\rangle$. This is essentially the overlap of the time evolved state and the initial state. It exhibits a damped oscillation pattern and this overlap tends to stabilize at a finite constant value in Fig. 2.13 (a). This stabilized constant can characterize how the initial state is inherently compatible with the quench Hamiltonian. In Fig. 2.13 (b) is time dependence of the central bond entanglement entropy. The linearly increasing entanglement entropy is consistent with the studies on 1D quantum systems [28, 29]. A qualitative picture to understand it involves quasiparticles. The quench in our study is global in the sense that each onsite coupling undergoes a change or perturbation. This perturbation results in quasiparticle excitations. These excitations travels at some speed v. Thus the distance between entangled quasiparticle pairs increase linearly with time. This could be signified by the correlations of the local observables. The regions covered by the entangled pairs exhibit a light-cone pattern. If we assume the entanglement entropy scales as the number of entangled pairs, the entanglement entropy should increase linearly.

The linearly increasing entanglement entropy is also found in quenches for different electron filling fractions in this system, which we don't show here. The growing entanglement entropy, leading to growing bond dimensions for accurate representations of the evolving states, means that simulation of long time dynamics is difficult

in the framework of TEBD for such a system.

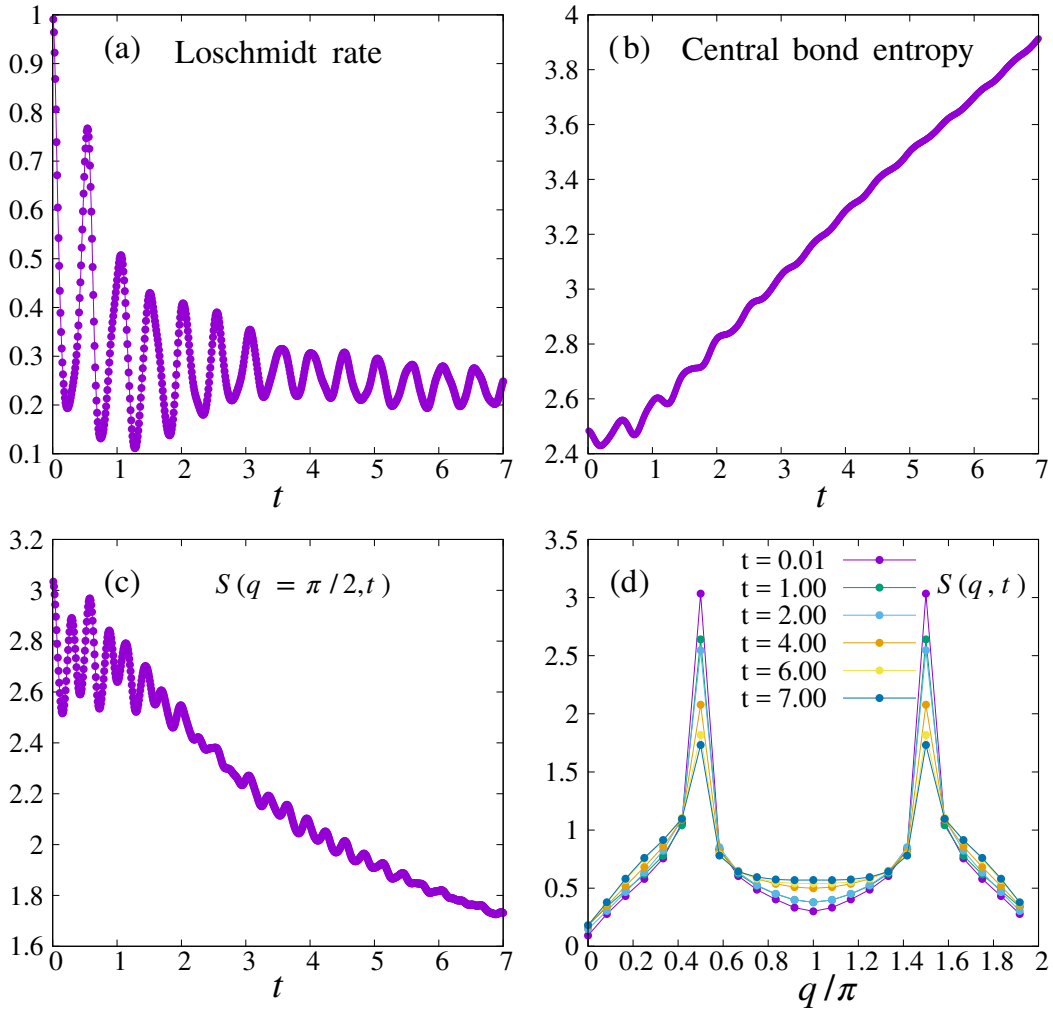

Figure 2.13: Dynamics of the Kondo lattice model simulated on a chain of size $L = 20$. (a) is the time dependence of the Loschmidt rate, (b) is the time dependence of the central bond entropy, (c) is the time dependence of $S(q = \frac{\pi}{2})$ and (d) shows a few snapshots of $S(q)$ at different time slices.

To take a closer look at how the states are evolved, we compute the time dependence of the spin structure factor at the prominent peak $\pi/2$. As imagined, $S(q = \pi/2)$ decreases over time in Fig. 2.13 (c). The decrease takes a similar oscillation pattern as the Loschmidt rate. In Fig. 2.13 (d), we plot $S(q)$ for a few time

snapshots. Although the peak is fading away, the peak at $q = \pi/4$ remains significant with the time span of the simulations. Another interesting observation is that $S(q = 0)$ does not increase much, although we are using $J = 20$ to quench the system.

Chapter 3

Frustrated Kondo Chains and Glassy Magnetic Phases on the Pyrochlore Lattice

In this chapter, we present an extensive numerical study of a model for frustrated itinerant magnet. This model is composed of cross-linked Kondo chains on the pyrochlore lattice, which gives rise to a new kind of geometrical frustration. This itinerant electron picture provides a natural explanation for several spin and orbital superstructures observed in materials on the pyrochlore lattice. We extract the phase diagrams for the model at two representative filling fractions 1/2 and 2/3 through extensive Monte Carlo simulations. We find a glassy magnetic state with wave vector $\mathbf{q} = \left(\frac{1}{3}, \frac{1}{3}, 1\right)$ to provide a good description of the low temperature phase observed in spinel $GeFe_2O_4$.

3.1 Introduction to Frustration

Frustration is common in condensed matter physics. It happens with a large ground state degeneracy. There are basically two kinds of sources of frustration. One of them is from competing interactions. The simplest example of this kind of frustrated system would be the one-dimensional axial next-nearest neighbor Ising (ANNNI) model [30] as illustrated in figure.

$$H = -J_1 \left(\sum_i S_i S_{i+1} - \kappa \sum_i S_i S_{i+2} \right) \tag{3.1}$$

In this model, the ferromagnetic nearest neighbor interaction J_1, which favors a ferromagnetic state with all spins pointing up or down. However, the antiferromagnetic interaction $J_2 = -\kappa J_1$ between second nearest neighbors favors the up-up-down-down pattern as in Fig. 3.1. No matter how the spins are arranged, the state cannot satisfy

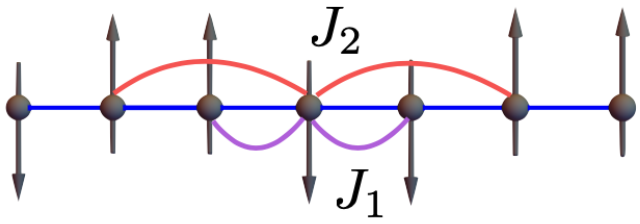

Figure 3.1: A schematic diagram of the 1D ANNNI model. J_1, J_2 are the coupling between nearest, second nearest neighbors.

both ground state constraints simultaneously. The competition between these two interactions gives rise to a rich phase diagram. A comprehensive review on the 1D, 2D, 3D ANNNI models can be found in [30].

Another kind of frustration comes from the fact that the pairwise interactions cannot be simultaneously minimized due to the lattice geometry. The interactions may lead to one or a few well-defined stable ground state on some lattice, but result

in frustration on other lattices (geometrical frustration). Let's consider a simple antiferromagnetic Ising model [3] on a square lattice Fig. 3.2 (a). Here we can find a simple pattern for the ground state, in which each spin has antiparallel neighbors. The ground state degeneracy is 2. However, if the lattice is triangular as in Fig. 3.2 (b), the scenario becomes different. The first two spins could be aligned anti-parallelly, but the third spin is frustrated because it does not know how to align itself. Either pointing up or pointing down gives rise to the same energy.

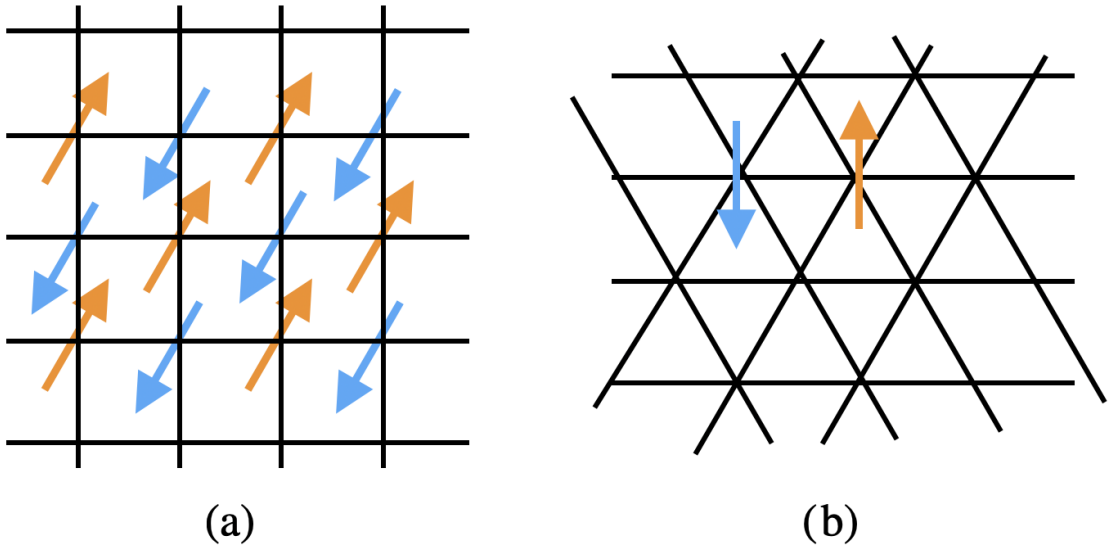

Figure 3.2: The antiferromagnetic Ising model on a square lattice (a) without frustration and triangular lattice (b) with frustration reproduced from Ref. [3].

One of the most notable features of strong frustration is the emergence of macroscopic degeneracy. The model usually used to illustrate this is the Heisenberg model

$$H = J \sum_{\langle i,j \rangle} \mathbf{S}_i \cdot \mathbf{S}_j, \tag{3.2}$$

where $\langle i, j \rangle$ denotes the nearest neighbors and $\mathbf{S}_i$ is a classical Heisenberg spin on site i. Instead of considering how the individual spins should be arranged, it is usually

more convenient to view the model in terms of simplexes. We write the Hamiltonian as

$$H = \frac{J}{2} \sum_{\alpha} |\mathbf{L}_\alpha|^2 + C. \tag{3.3}$$

Here C is a constant that could be ignored, $\mathbf{L}_\alpha = \sum_{i \in \alpha} \mathbf{S}_i$ is the sum of mutually interacting spins in a simplex. In a triangular lattice, the simplex is the smallest triangle composed of 3 spins. In the pyrochlore lattice (Fig. 3.3), the simplex is the smallest tetrahedra with 4 spins. In a ground state, all $\mathbf{L}_\alpha = \mathbf{0}$. There are many possible configurations for this condition to be satisfied. To obtain the ground state degeneracy, we apply the Maxwell counting argument. Denote F, K, D as the number of degrees of freedom in the system, number of constraints in the ground state, number of ground state degree of freedom, respectively. Then we have $D = F - K$.

The pyrochlore lattice is a face-centered cubic (FCC) lattice with a basis consisting of a tetrahedra, as shown in Fig. 3.3. On a pyrochlore lattice with N Heisenberg spins, $F = 2N$ since each spin has 2 degrees of freedom as it could be parametrized by two numbers, polar angle θ and azimuthal angle ϕ. Each cluster contains 4 spins and each spin is shared by 2 clusters, thus there are $N/2$ clusters in total and $D = \frac{3}{2}N$. Finally the ground state degree of freedom is $D = F - K = \frac{1}{2}N$. It is an extensive number. The low temperature phase is confined in the region near the ground state manifold and the system is thus sensitive to perturbation. The extensive ground state degree of freedom also gives rise to some other features of frustrated system, such as order by disorder.

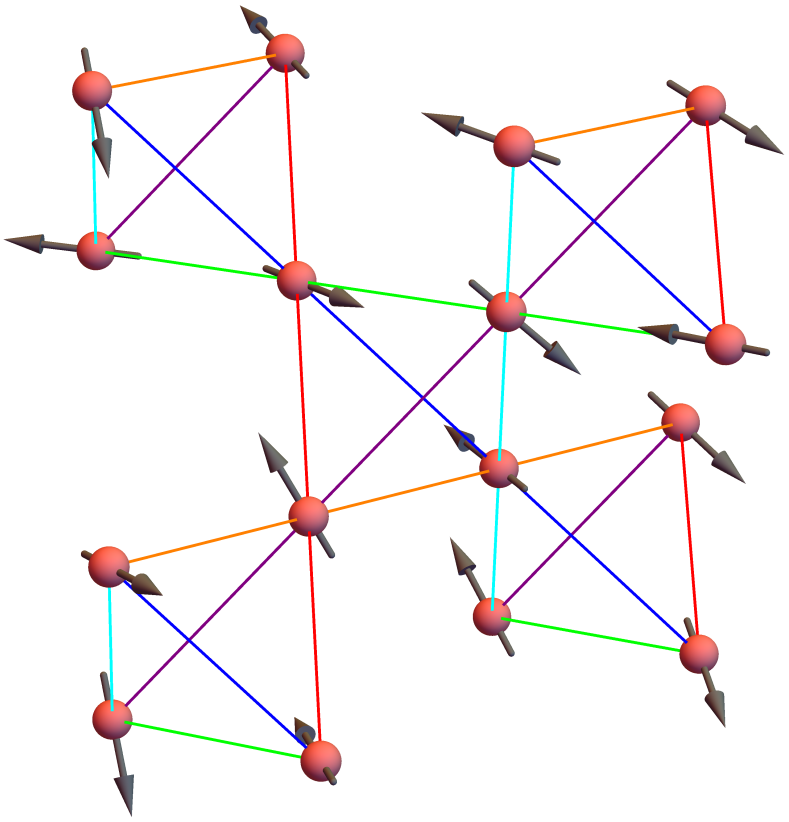

Figure 3.3: A unit cell of the pyrochlore lattice with spins on each site.

3.2 Motivation and Overview

Highly frustrated magnets continue to fascinate physicists with intriguing and sometimes unexpected magnetic phases. This is particularly true for spin systems exhibiting strong geometrical frustration such as pyrochlore antiferromagnets [3]. Conventionally, frustrated magnets are modeled by the Heisenberg Hamiltonian $\mathcal{H} = \sum_{ij} J_{ij}\mathbf{S}_i \cdot \mathbf{S}_j$ within the framework of Mott insulators. For pyrochlore and kagome lattices, the frustrated nearest-neighbor antiferromagnetic spin interactions give rise to a macroscopic ground-state degeneracy [31, 32]. This in turn makes the magnets highly susceptible to small perturbations. Removal of the extensive degeneracy

by perturbations beyond J_1 leads to unusual spin ordering and even unconventional magnetic phases [33, 34]. For systems with degenerate orbitals, a good starting point is the Kugel-Khomskii Hamiltonian [35], which has been successfully employed to understand spin-orbital ordering in frustrated magnets [36, 37, 38].

Recently, complex spin and/or orbital superstructures observed in spinels such as $CuIr_2S_4$ [39, 40], $MgTi_2O_4$ [41], and ZnV_2O_4 [42] have posed an intriguing theoretical challenge. Several models have been proposed to explain the experimental results. However, understanding these unusual orderings within the framework of Mott insulators often requires fine tuning or sometimes *ad hoc* perturbations. On the other hand, it has been demonstrated in many cases that approaches based on itinerant magnetism provide a very natural explanation for the observed superstructures [43, 44, 45]. For example, the octamer-order in $CuIr_2S_4$ and chiral distortion in $MgTi_2O_4$ can be explained as resulting from an orbital driven Peierls instability [43, 46]. Moreover, several of these compounds have been shown to be a bad insulator, indicating that these magnets are in the vicinity of metal-insulator transition [47, 48, 49, 50]. Recent experiments further support the picture of orbital-Peierls state [51, 52].

The itinerant approach also naturally explains the $\mathbf{q} = (0, 0, 1)$ magnetic structure of ZnV_2O_4, which consists of $\uparrow\uparrow\downarrow\downarrow \cdots$ spin chains along [110] directions of the pyrochlore lattice [44, 45]. Essentially, taking into account the reduced dimensionality of electron hopping in such systems, this interesting commensurate one-dimensional (1D) order can be understood as resulting from the spin-induced nesting instability of 1D Kondo chains. Another interesting example is the multiple-$\mathbf{q}$ magnetic ordering recently observed in spinel $GeFe_2O_4$ [53]. At low temperatures, neutron-scattering experiments found diffusive peaks centered at $\mathbf{q} = (\frac{1}{3}, \frac{1}{3}, 1)$ and other symmetry-related wavevectors, implying a quasi-1D ordering with a tripled unit cell. Stabilization of

this unusual commensurate magnetic order seems rather difficult using the localized spin models.

In this chapter, we present a detailed numerical study of a novel frustrated itinerant spin model for spinel compounds AB_2X_4. In these materials, the octahedral crystal field splits the $3d$ orbitals of the B-site magnetic ion into a t_{2g} triplet and a higher energy e_g doublet. The lattice structure (pyrochlore) is shown in Fig. 3.3. Keeping only the dominant $dd\sigma$ transfer integral between the low-energy t_{2g} orbitals, electron hoppings on the pyrochlore lattice can be modeled by a set of one-dimensional (1D) tight-binding chains in this leading order approximation [44]. Inclusion of the on-site Hubbard and Hund's interactions within the mean-field approximation then leads to Kondo or double-exchange type electron-spin couplings. A minimum model is given by a collection of cross-linking Kondo chains running along the $\langle 110 \rangle$ directions of the pyrochlore lattice. Importantly, commensurate 1D spin order can arise naturally as a result of Fermi point nesting instability in Kondo chains with a rational electron filling fraction. A new type of geometrical frustration then results from the fact that the favored 1D spin order cannot be realized on all chains simultaneously, leading to novel 3D magnetic order and to glassy behavior in some cases.

3.3 Frustrated Kondo Chains on the Pyrochlore Lattice Model

Our itinerant electron approach to magnetic orders in spinels is based on a mean-field treatment of Hubbard-type Hamiltonian. First, we consider the tight-binding model of t_{2g} orbitals in spinels. As discussed above, the magnetic ions in spinels form a pyrochlore lattice. Fig. 3.4 shows some representative hopping processes of t_{2g} electrons on the pyrochlore lattice. Here the various hopping integrals are computed

using the Slater-Koster formula; the results can be expressed in terms of fundamental bond integrals $V_{dd\sigma}$, $V_{dd\pi}$, and $V_{dd\delta}$ [54]. In general, the σ bond-integral is much stronger than the π, and δ bonds. To the leading-order approximation, we thus neglect contributions from $V_{dd\pi}$ and $V_{dd\delta}$ to the various bond integrals. As a result, only the t_1 hopping remains in this approximation, which means only those nearest-neighbor hoppings between the same type of orbitals among appropriate chains dominate, namely, d_{xy} along $\langle 110\rangle, \langle 1\bar{1}0\rangle$, d_{yz} along $\langle 011\rangle, \langle 01\bar{1}\rangle$ and d_{zx} along $\langle 101\rangle, \langle \bar{1}01\rangle$, see Fig. 3.4.

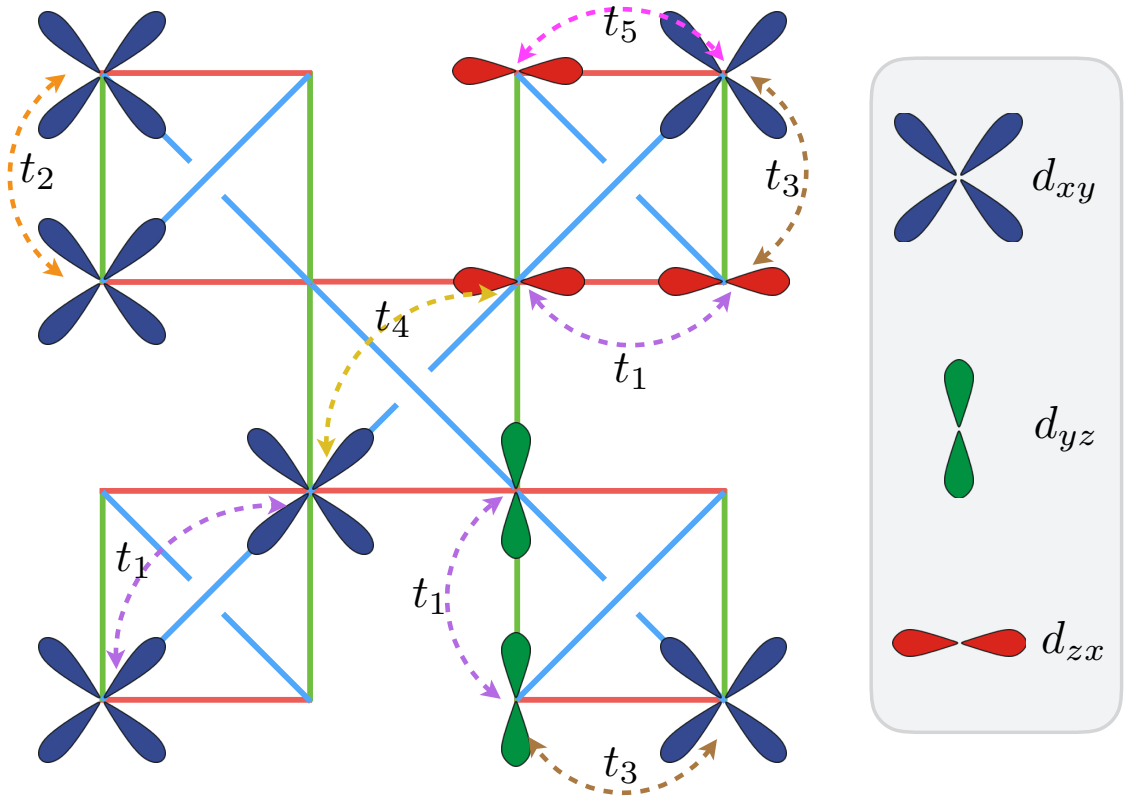

Figure 3.4: The inequivalent transfer integrals between the three t_{2g} orbitals on the pyrochlore lattice: $t_1 = \frac{3}{4}V_{dd\sigma} + \frac{1}{4}V_{dd\delta}$, $t_2 = \frac{1}{2}V_{dd\pi} + \frac{1}{2}V_{dd\delta}$, $t_3 = \frac{1}{2}V_{dd\pi} - \frac{1}{2}V_{dd\delta}$, $t_4 = t_5 = 0$.

Next we consider the on-site interactions which is dictated by the multi-orbital Hubbard-Kanamori interaction $\mathcal{H}_U$ [55]. Since we are interested in solutions with

non-zero local moment, we use the Hartree-Fock mean-field method to decouple the interaction terms. The mean-field decoupling gives rise to a Kondo-like electron-spin coupling $\mathcal{H}_U = U_{\text{eff}}\langle\hat{\mathbf{s}}_i\rangle \cdot \hat{\mathbf{s}}_i$, where $\hat{\mathbf{s}}_i$ is the electron spin operator, and U_{eff} is an effective Hubbard parameter. For example, for t_{2g} orbitals, $U_{\text{eff}} = 4(U/9 + 4J_H/9)$, where U and J_H are the on-site Hubbard repulsion and Hund's coupling, respectively. In the case of $GeFe_2O_4$, the magnetic Fe^{2+} ions have a $t_{2g}^4\, e_g^2$ electron configuration. Due to strong intra-orbital Hubbard interaction and Hund's coupling, the two e_g electrons remain in the correlated $S = 1$ state. The remaining t_{2g}^4 electrons thus form conduction band with a filling fraction $n = 2/3$.

We thus arrive at the following Hamiltonian describing cross-linking Kondo chains on the pyrochlore lattice in Fig. 3.5:

$$\mathcal{H} = -t\sum_{\mu,\sigma}\sum_{\langle ij\rangle\|\mu}\left(\hat{c}^{\dagger}_{i\,\mu\sigma}\,\hat{c}_{j\mu\sigma} + \text{h.c.}\right) - J\sum_{i,\mu}\mathbf{S}_i \cdot \hat{\mathbf{s}}_{i,\mu} \tag{3.4}$$

where $\hat{c}^{\dagger}_{i,\mu\sigma}$ is the creation operator for electron with spin $\sigma =\uparrow,\downarrow$ and orbital flavor $\mu = xy$, yz, zx at site-i, $\langle ij\rangle \parallel \mu$ indicates the nearest-neighbor (NN) pair along the $\langle 110\rangle$ direction that corresponds to the active t_{2g} orbital μ, the hopping constant t is set to be 1 in all the simulations below, $J \approx U_{\text{eff}}\langle\hat{\mathbf{s}}\rangle$ is the effective Hund's coupling, $\mathbf{S}_i$ is the $O(3)$ local magnetic moment, and $\hat{\mathbf{s}}_{i,\mu} = \sum_{\alpha,\beta} c^{\dagger}_{i\mu\alpha}\boldsymbol{\sigma}_{\alpha\beta}c_{i\mu\beta}$ is the electron spin operator.

The 1D ferromagnetic Kondo chain, which is the backbone of Hamiltonian (4.1), have been extensively studied over the years [8, 2, 56]. However, the fact that every local spin $\mathbf{S}_i$ is shared by three Kondo chains introduces competition between different chains. In particular, the cross-linking Kondo chains exhibit a new type of geometrical frustration since the electronic energy of neighboring chains cannot be simultaneously minimized. For example, the shortest hexagonal loops (Fig. 3.5)

of spins on the pyrochlore lattice contain sites which belong to six different Kondo chains. Consequently, the nearest-neighbor spin-spin correlation favored by individual chains might not be able to extend over the hexagonal loop consistently, leading to frustrated interactions.

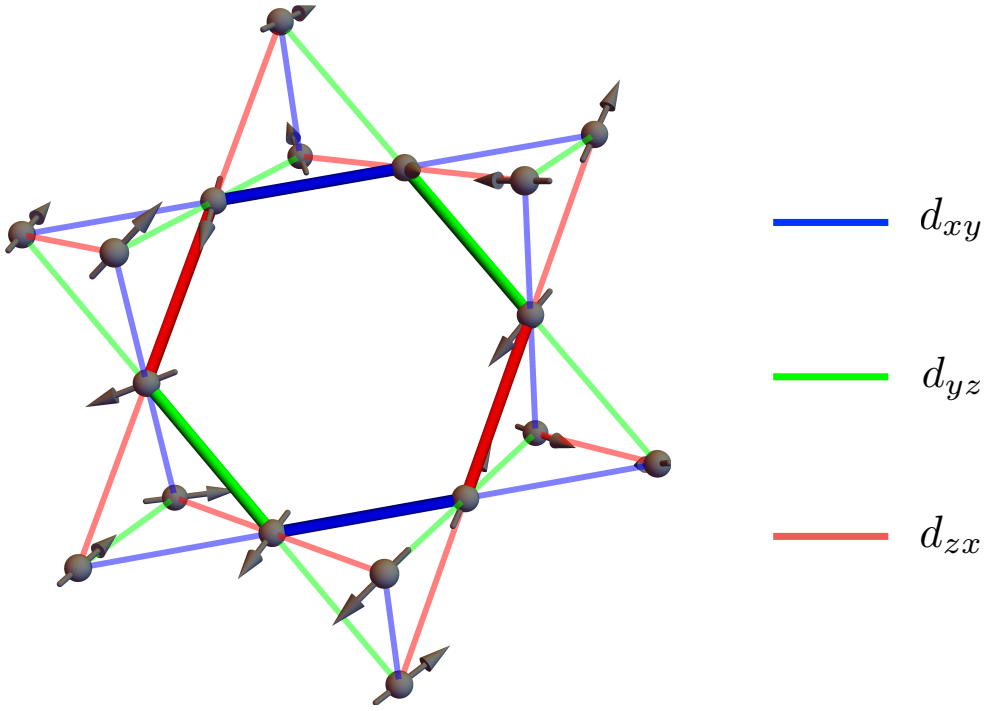

Figure 3.5: Schematic diagram showing the shortest hexagonal loops in the pyrochlore lattice. The three different colors indicate distinct Kondo chains occupied by the three t_{2g} orbitals.

Since our main interest is in the potential magnetic orderings of this model, we will assume classical local spins here. However, even with classical local spins, Monte Carlo simulations of Kondo-lattice models are a challenging task mainly due to the non-local electron-mediated effective interactions between the local moments. Indeed, in the weak-coupling limit $J \ll t$, integrating out the electrons gives rise to a long-range RKKY type spin interactions. For large J, one needs to diagonalize the electron tight-binding Hamiltonian that depends on the spin configuration for each Monte

Carlo update. For a pyrochlore lattice of linear size L, there are $N = 16L^3$ spins and the dimension of a generic spinful and orbitally degenerate TB Hamiltonian is $D = 2\times3\times N = 96L^3$. This severely limits the largest accessible lattice sizes, as exact diagonalization scales as $\mathcal{O}(D^3)$ and is computationally very costly. However, thanks to the 1D nature of the TB model in Eq. (4.1), each local spin update only requires diagonalizing three chains whose dimension is $D_{\rm 1D} = 4L$. Specifically, we adopt the standard local Metropolis Monte Carlo method. For a randomly chosen spin, say at site-i, we consider rotating the spin from $\mathbf{S}_i$ to $\mathbf{S}_i'$. The energy cost associated with this update comes from the electron energy of the three Kondo chains intersecting at this site, i.e.

$$\Delta E = \sum_{\mu=xy,yz,zx} \left[\sum_{m=1}^{N_f} \left(\varepsilon_m^{(\mu)}(\mathbf{S}_i') - \varepsilon_m^{(\mu)}(\mathbf{S}_i) \right) \right]. \tag{3.5}$$

Here $\varepsilon_m^{(\mu)}$ are the eigen-energies of the μ-orbital Kondo chain and N_f is the number of occupied electrons determined by the filling fraction. Once ΔE is obtained by exactly diagonalizing the three chains intersecting at $\mathbf{S}_i$, the spin-update is accepted according to the standard Metropolis algorithm with a probability

$$p_{\rm acc} = \min\left[1, \exp\left(-\frac{\Delta E}{k_B T}\right)\right]. \tag{3.6}$$

The computational cost of each update thus scales as $\mathcal{O}(D_{\rm 1D}^3) \sim \mathcal{O}(N)$. Each sweep is completed by updating local spins sequentially. The Monte Carlo simulation for the coupled chains is still costly with an overall scaling $\mathcal{O}(N \times D_{\rm 1D}^3) \sim \mathcal{O}(N^2)$, but the efficiency is much improved compared with the full 3D tight-binding model.

3.4 Phase Diagrams

In this part we obtain the phase diagram of Hamiltonian Eq. (4.1) for two representative filling fractions $n = 1/2$ and $2/3$ based on extensive Monte Carlo simulations; the results are summarized in Fig. 3.6.

3.4.1 Half filling

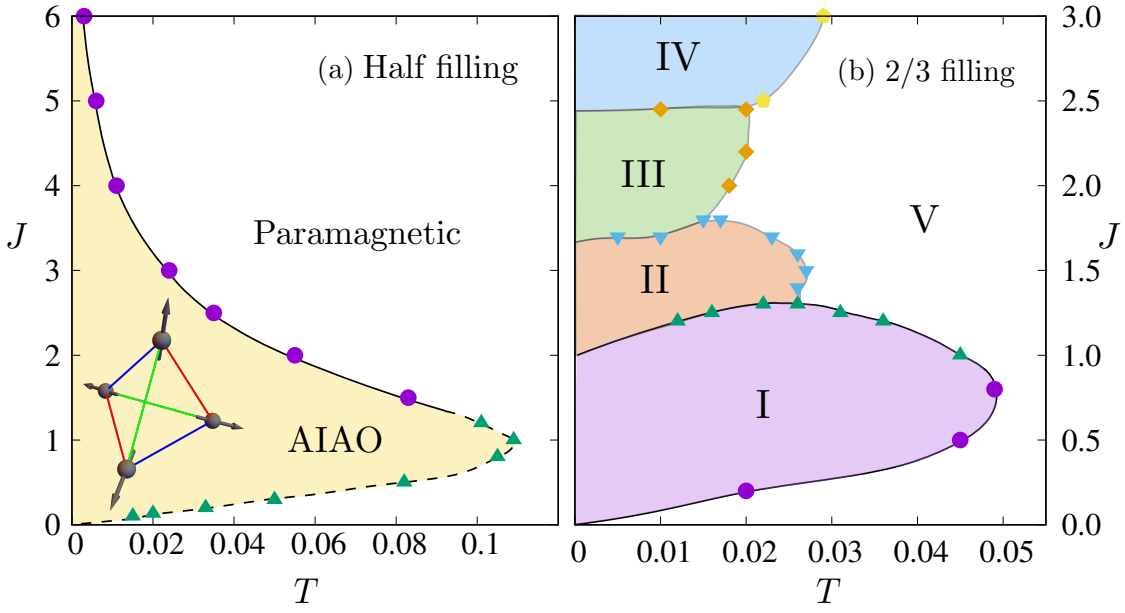

Figure 3.6: The phase diagrams for (a) half filling and (b) 2/3 filling. Solid and dashed lines represents 1st and 2nd order phase transitions respectively in both (a) and (b). For half filling, two phases are all-in-all-out phase (AIAO), paramagnetic phase. For 2/3 filling, phases are (I) $\mathbf{q} = \left(\frac{1}{3}, \frac{1}{3}, 1\right)$ order, (II) $\left(\frac{1}{2}, \frac{1}{2}, \frac{1}{2}\right)$ order, (III) a unknown magnetic phase characterized by a large spin nematic order parameter, (IV) ferromagnetic phase and (V) paramagnetic phase.

We first discuss the simpler case of half-filling. There is only one ordered phase characterized by the non-coplanar all-in-all-out (AIAO) spin order at low temperatures; see Fig. 3.6(a). For a half-filled Kondo chain, the nesting of the Fermi points favors a collinear Néel order with doubled unit cell, i.e $\uparrow\downarrow\uparrow\downarrow\cdots$. However, it is easy

to convince oneself that such collinear ordering cannot be simultaneously realized in the three different chains on the pyrochlore lattice; a manifestation of the geometrical frustration is discussed above. The solution to this conflicted situation is the AIAO order in which an 1D spin-order with a doubled unit cell, albeit with non-collinear spins, still gaps out the Fermi points and lowers the overall energy. The AIAO order is characterized by three non-zero staggered magnetization:

$$\mathbf{L}_1 = \mathbf{S}_0 + \mathbf{S}_1 - \mathbf{S}_2 - \mathbf{S}_3, \tag{3.7}$$

and the symmetry-related $\mathbf{L}_2$ and $\mathbf{L}_3$. Here $\mathbf{S}_m$ denotes the spin of the m-th sublattice (there are four sublattices) of the pyrochlore lattice. A perfect AIAO has $|\mathbf{L}_1| = |\mathbf{L}_2| = |\mathbf{L}_3|$ while their orientations satisfy $\mathbf{L}_1 \perp \mathbf{L}_2 \perp \mathbf{L}_3$. Due to the non-coplanar nature of this magnetic order, the AIAO phase further breaks a Z_2 chiral symmetry which is measured by the discrete scalar spin chirality

$$\chi = \mathbf{L}_1 \cdot (\mathbf{L}_2 \times \mathbf{L}_3) \tag{3.8}$$

The phase boundary of the AIAO order, shown in Fig. 3.6(a), is determined from the Binder crossing of corresponding staggered order parameters for continuous phase transition at small J.

Interestingly, the transition becomes first-order at large J. As in general Kondo-lattice or double-exchange models, the effective Hamiltonian in the large-J limit is given by a Heisenberg model with a dominant NN exchange $J_{\mathrm{AF}} \sim t^2/J$. This can be understood as follows. In the $J \to \infty$ limit at half-filling, electrons are localized in individual orbitals of each site with their spins aligned with the local moments. This gives rise to a huge degeneracy which is lifted by the electron hopping. Due to Pauli exclusion principle, electrons can hop to neighboring sites only when their spins are

not aligned, thus favoring an antiferromagnetic interaction. Specifically, the effective Hamiltonian corresponds to the energy gain through the second-order process, which is

$$E_{ij}^{(2)} \approx -\frac{\left[t \langle \chi_i | \chi_j \rangle\right]^2}{J}, \tag{3.9}$$

where $|\chi_i\rangle$ is the local electron spinor wavefunction. Since Pauli exclusion requires that the spins at i and j must be anti-aligned in order to allow the electrons hop to the NN sites, the inner product of the spinor eigenstates $\langle \chi_i | \chi_j \rangle = \sin(\theta_{ij}/2)$, where θ_{ij} is the angle between the two local spins. Consequently, we obtain an effective spin interaction:

$$E_{ij}^{(2)} = J_{\mathrm{AF}}\, \mathbf{S}_i \cdot \mathbf{S}_j \tag{3.10}$$

up to a constant, with $J_{\mathrm{AF}} \sim t^2/J$.

It is interesting to note that the frustrated nature of the coupled Kondo chains in the large-J limit corresponds to the well known geometrical frustration of AF Heisenberg model on the pyrochlore lattice. The huge ground-state degeneracy of this model leads to a low temperature spin liquid phase. Contrary to the high-temperature paramagnetic phase, disordered spins in this classical spin liquid exhibit strong short-range correlation [32]. A possible scenario is that the system first enters a correlated classical spin liquid regime at $T \sim J_{\mathrm{AF}}$, then undergoes a phase transition at a lower T_c into the AIAO phase. Our detailed analysis shows that the classical spin liquid phase is preempted by the first-order transition, and the system immediately goes to the AIAO phase at a critical $T_c \sim J_{\mathrm{AF}}$.

3.4.2 2/3 filling

We now turn to the case of 2/3-filling. Before discussing the phase diagram of coupled Kondo chains on the pyrochlore lattice, we first consider the ground states of a single Kondo chain. The Fermi wavevector of a 2/3-filled 1D band is $k_F = 2\pi/3\ell$, where $\ell = \sqrt{2}a/4$ is the 1D lattice constant and a is the size of the cubic unit cell. The system is thus susceptible to perturbations with a wavevector $q = 2k_F = 4\pi/3\ell$ that gaps out the two Fermi points; see Fig. 3.7. Indeed, our Monte Carlo simulations on a single Kondo chain find a magnetic order with a tripled unit cell at $T \to 0$ and small J. The three spins within the extended unit cell are coplanar, with a relative angle very close to 120°; more details can be found in Appendix A.

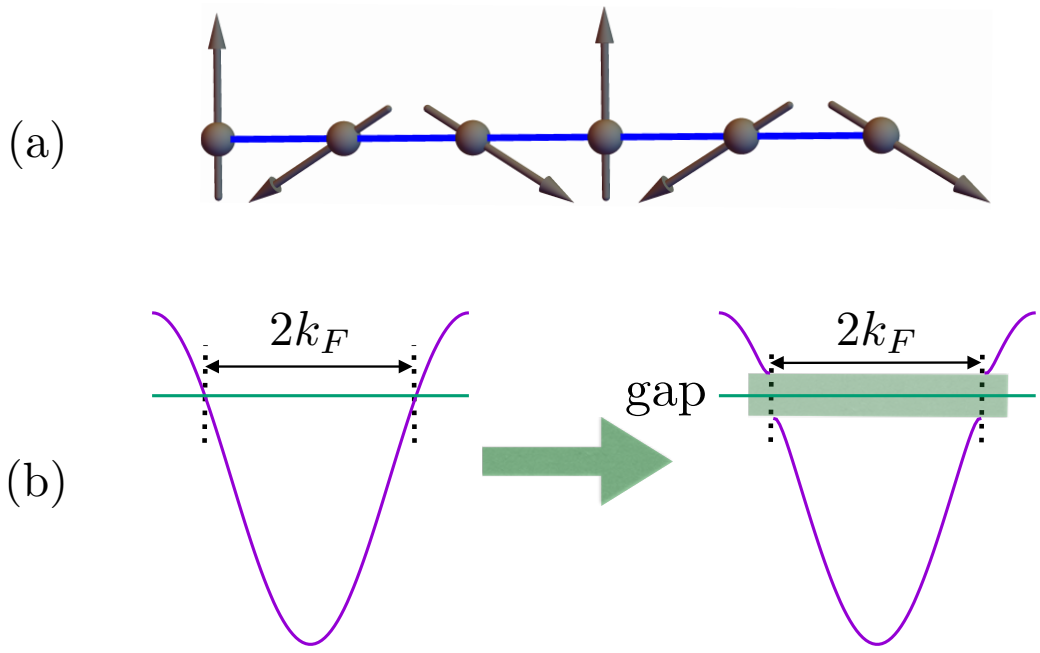

Figure 3.7: (a) The $T \to 0$ ground state of a single Kondo chain. The long-range spin order is characterized by a tripled unit cell with a coplanar almost 120° structure within a unit cell. (b) shows the gap-opening of a $n = 2/3$-filled Kondo chain due to Fermi point nesting.

Next we apply the above 1D results to understand the ground-states of coupled

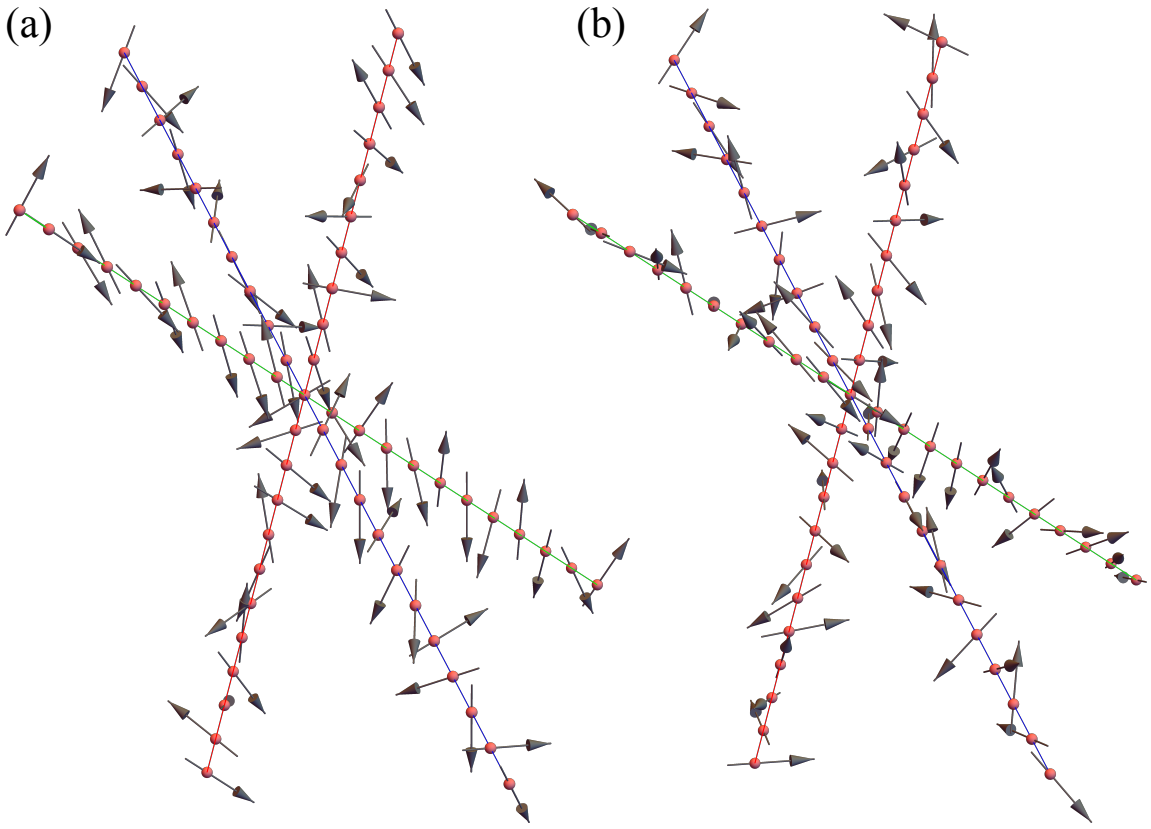

Figure 3.8: Snapshots of the local spin configurations for (a) the $\mathbf{q} = (\frac{1}{3}, \frac{1}{3}, 1)$ order and (b) $\mathbf{q} = (\frac{1}{2}, \frac{1}{2}, \frac{1}{2})$ order.

Kondo chains in 3D, which is particularly important in explaining the magnetic order of spinel $GeFe_2O_4$ where the t_{2g} orbitals are 2/3-filled. From direct inspection of the geometry, one immediately realizes that the above coplanar 1D ground-state cannot be consistently combined in the 3D pyrochlore lattice. This is another manifestation of the geometrical frustration discussed in Fig. 3.5. Contrary to the half-filling case, where the frustrated coupling leads to the AIAO long-range order, there is no simple magnetic structure selected in the 2/3-filling case. A snapshot of spin configuration from our Monte Carlo simulations is shown in Fig. 3.8(a). Individual Kondo chains are clearly not in their 1D ground state discussed above. In fact, spins on a given chain are not even coplanar. Although no clear pattern can be seen from this snapshot, detailed characterization shows that a long-range spin-spin correlation with a tripled unit cell nonetheless is developed along each individual chain of the 3D lattice; see Fig. 3.9(a). Moreover, the 3D non-coplanar spin order is characterized by multiple wavevectors that are related to $\mathbf{q} = (\frac{1}{3}, \frac{1}{3}, 1)$ by symmetry, as shown in the inset of Fig. 3.9(a).

From the phase diagram of single Kondo chain discussed in Appendix A, the magnetic order at large J cannot be understood from the Fermi-point nesting picture. Here we performed extensive Monte Carlo simulations to obtain the $n = 2/3$-filling phase diagram, shown in Fig. 3.6(b). At small Hund's coupling, the low-T phase is a magnetic order characterized by multiple ordering wavevectors that are related to $\mathbf{q} = (\frac{1}{3}, \frac{1}{3}, 1)$, as discussed above. Several unusual magnetic structures are obtained at larger J. The phase boundaries are mostly first order, except for the small J regime (purple dots) where the phase transition between paramagnetic and $(\frac{1}{3}, \frac{1}{3}, 1)$-ordered phases might be continuous.

The various 3D phases are loosely related to their 1D counterpart. Upon increasing J, the ordering wavevectors first change from $\mathbf{q} = (\frac{1}{3}, \frac{1}{3}, 1)$ to $(\frac{1}{2}, \frac{1}{2}, \frac{1}{2})$ at $J \approx t$. The

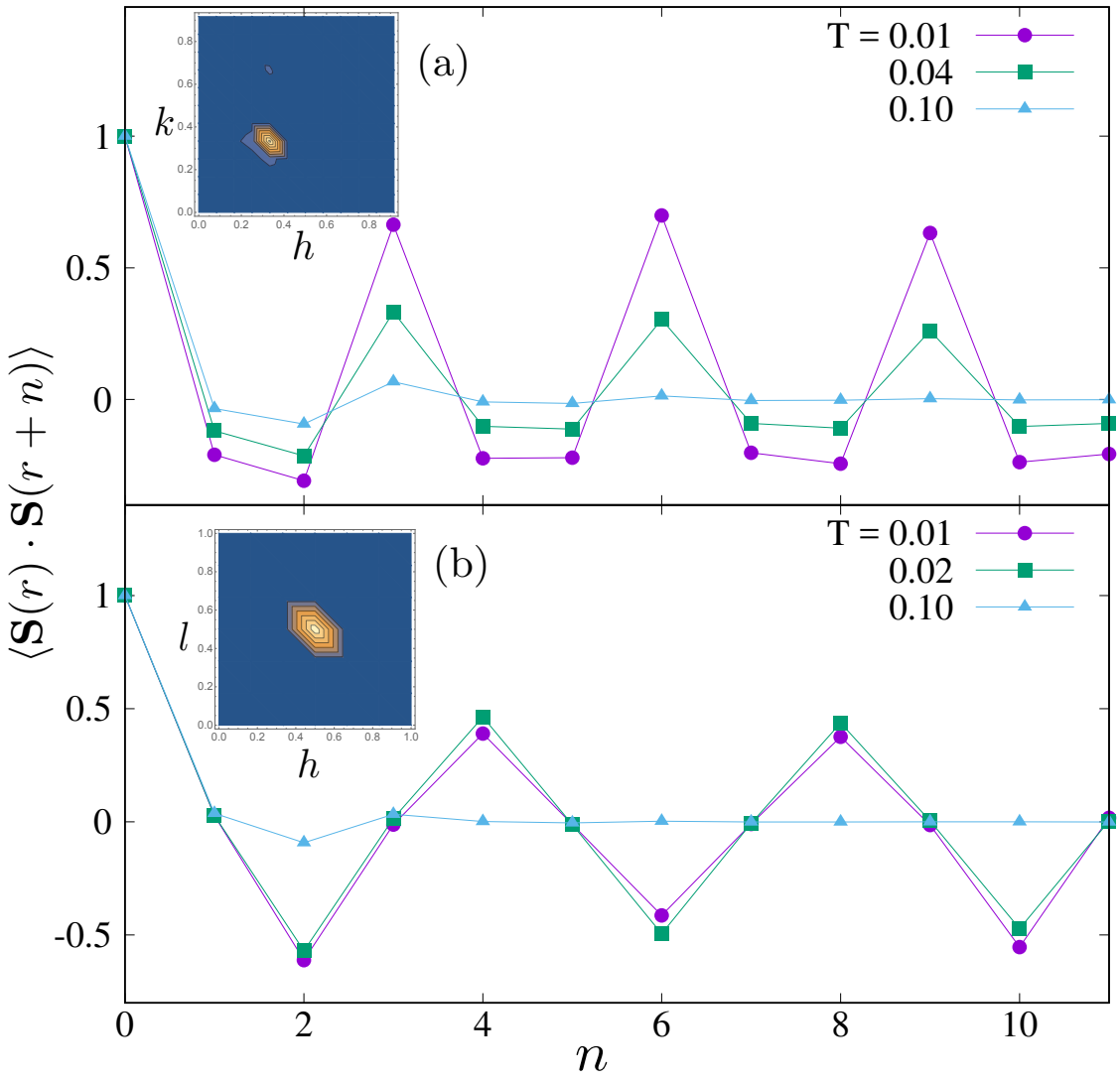

Figure 3.9: The spin-spin correlation function $\langle \mathbf{S}(r) \cdot \mathbf{S}(r+n) \rangle$ averaged over all Kondo chains of the pyrochlore lattice for (a) the $\mathbf{q} = (\frac{1}{3}, \frac{1}{3}, 1)$ and (b) the $\mathbf{q} = (\frac{1}{2}, \frac{1}{2}, \frac{1}{2})$ order at $n = 2/3$ filling with (a) $J = 1$ for and (b) $J = 1.5$. The insets show the corresponding structure factor on the (a) $\mathbf{q} = (h, k, 1)$ and (b) $\mathbf{q} = (h, h, l)$ plane.

system undergoes another 1st-order transition at $J \approx 1.6t$ into an unknown magnetic order (phase III) that is characterized by rather large nematic order parameter. We have checked that spins are pretty much frozen in this phase, yet no clear long-range order can be seen from the static structure factor. And finally, the ferromagnetic order takes over as the ground state when $J \gtrsim 2.5t$.

An interesting case is the $\mathbf{q} = (\frac{1}{2}, \frac{1}{2}, \frac{1}{2})$ phase at intermediate Hund's coupling $1 \lesssim J \lesssim 1.6$ (phase-II in the phase diagram). A snapshot of local spin configurations on three different chains intersecting at one spin is shown in Fig. 3.8(b). Again, although no clear ordering pattern can be found in the snapshot, detailed analysis showed that individual Kondo chains exhibit a clear 1D spin correlation with a quadrupled unit cell, as shown in Fig. 3.9(b). This is in stark contrast to the ground state of a single Kondo chain in the same J regime, where the $T \to 0$ ground state is a multiple-q non-coplanar order. In this case, the "frustrated" inter-chain coupling actually stabilizes the quadrupled chains and the $\mathbf{q} = (\frac{1}{2}, \frac{1}{2}, \frac{1}{2})$ order on the pyrochlore lattice.

3.5 Quasi-degeneracy and Glassy Behaviors of the $\mathbf{q} = (\frac{1}{3}, \frac{1}{3}, 1)$ Phase

To characterize the complex multiple-$\mathbf{q}$ magnetic order in the $\mathbf{q} = (\frac{1}{3}, \frac{1}{3}, 1)$ phase, we introduce vector order parameters

$$\mathbf{\Phi}_m \equiv \frac{1}{N} \sum_j \mathbf{S}_j \exp(i\mathbf{q}_m \cdot \mathbf{r}_j), \tag{3.11}$$

which are the Fourier modes of spins at the 12 symmetry-related wavevectors $\mathbf{q}_m = \left(\pm\frac{1}{3}, \pm\frac{1}{3}, 1\right)$, $\left(\pm\frac{1}{3}, 1, \pm\frac{1}{3}\right)$, and $\left(1, \pm\frac{1}{3}, \pm\frac{1}{3}\right)$. Phenomenologically, the phase transition

is described by a Landau free energy expansion [57]

$$\begin{aligned}\mathcal{F} &= \alpha(T-T_c)\sum_m |\mathbf{\Phi}_m|^2 + \beta\sum_m |\mathbf{\Phi}_m|^4 \\ &+ \sum_{m,n,k,l}{}' \lambda_{mnkl}(\mathbf{\Phi}_m\cdot\mathbf{\Phi}_n)(\mathbf{\Phi}_k\cdot\mathbf{\Phi}_l) + \cdots ,\end{aligned} \tag{3.12}$$

where $\alpha, \beta > 0$, and the prime in the summation indicates the condition of momentum conservation, i.e. $\mathbf{q}_m + \mathbf{q}_n + \mathbf{q}_k + \mathbf{q}_l = 0$ module a reciprocal lattice vector. The overall $\mathbf{q} = (\frac{1}{3}, \frac{1}{3}, 1)$ magnetic ordering is measured by the order parameter

$$\mathcal{M} = \left(\sum_{m=1}^{12} |\mathbf{\Phi}_m|^2\right)^{1/2}. \tag{3.13}$$

The temperature dependence of the $\mathcal{M}$, shown in Fig. 3.10(b), clearly indicates that these vector order parameters develop a nonzero expectation value at $T < T_c$, where T_c is estimated to be $0.045t$ for $J = t$. Detailed structure of this $\mathbf{q} = (\frac{1}{3}, \frac{1}{3}, 1)$ magnetic order is determined by the interaction terms λ_{mnkl}, which are very difficult to compute analytically. Our extensive Monte Carlo simulations, on the other hand, seem to observe a multitude of different magnetic structures and a possible glassy regime below T_c.

To explore this intriguing glassy phase, we compute the so-called nematic order-parameter Q for spin structures obtained from our simulations. Essentially, this order parameter provides a measure of the collinearity of spins. It is given by the largest eigenvalue of the traceless matrix [58]

$$\mathcal{Q}_{\mu\nu} \equiv \langle S_\mu S_\nu - \frac{\delta_{\mu\nu}}{3}\rangle \quad (\mu,\nu = x,y,z). \tag{3.14}$$

This matrix is averaged over all spins in the lattice.

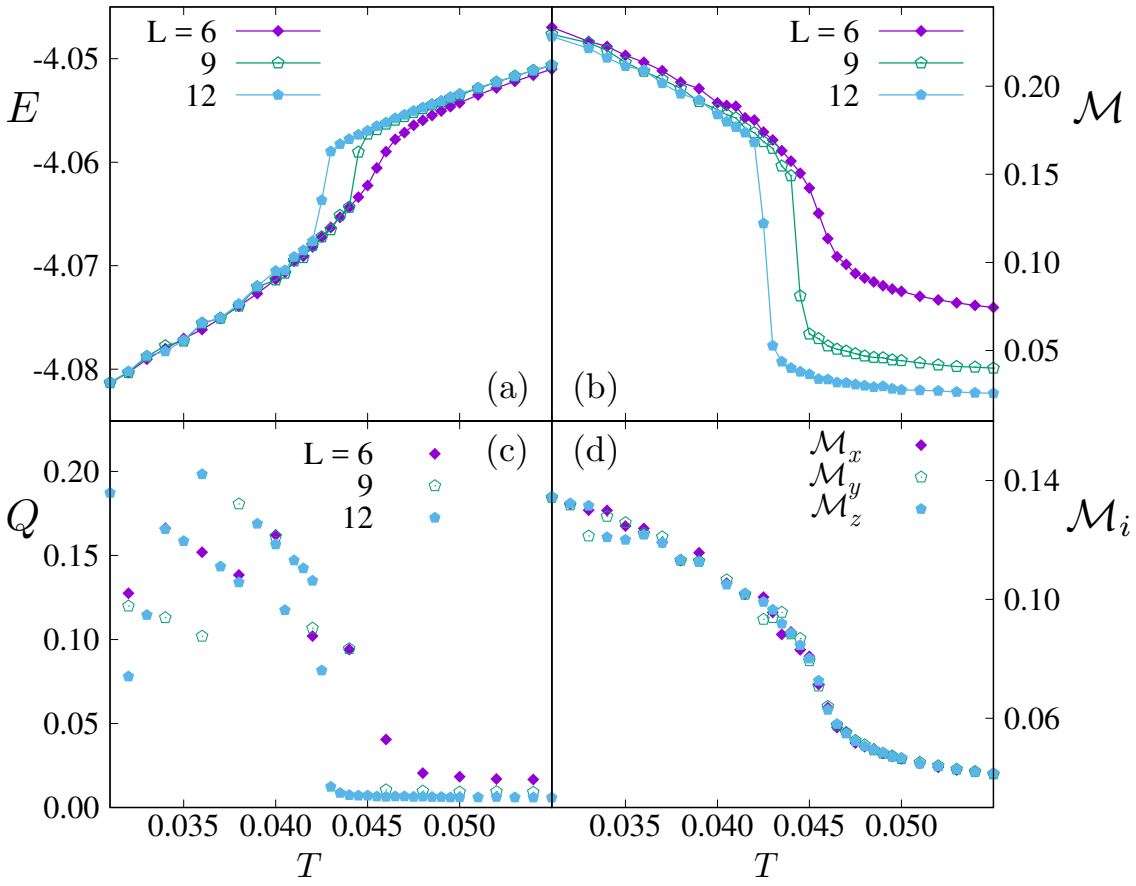

Figure 3.10: The temperature dependence of some quantities for the 2/3-filled coupled Kondo chains with $J = 1$. (a) the energy density and (b) the magnetic order parameter $\mathcal{M}$ shows the first order phase transition. (c) the nematic order parameter Q bifurcates into multiple branches below the phase transition point. (d) the partial magnetic order parameter, $\mathcal{M}_x, \mathcal{M}_y, \mathcal{M}_z$, which are summation of $\mathbf{\Phi}_m$ at wavevectors $\mathbf{q}_m = \left(1, \pm\frac{1}{3}, \pm\frac{1}{3}\right)$, $\left(\pm\frac{1}{3}, 1, \pm\frac{1}{3}\right)$, $\left(\pm\frac{1}{3}, \pm\frac{1}{3}, 1\right)$, respectively, with $L = 6$ show no significant difference at low temperatures.

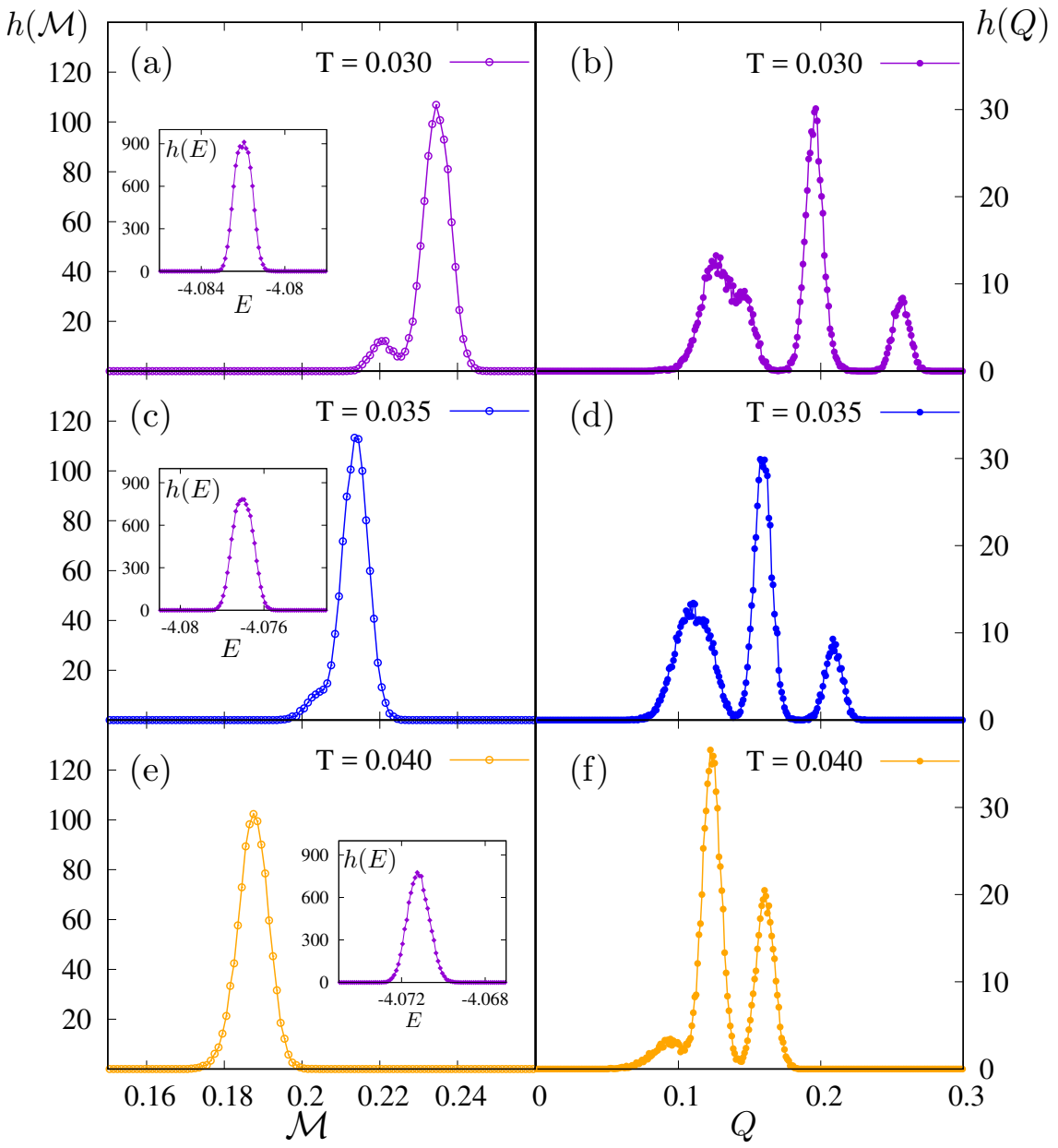

Figure 3.11: Probability distribution function for the magnetic order parameter $\mathcal{M}$, the nematic order parameter Q and the energy density E (insets) at three different temperatures below T_c. These curves are obtained from extensive Monte Carlo simulations on lattices of $J = 1, L = 9$.

Interestingly, the temperature dependence of the nematic order, shown in Fig. 3.10 (c), exhibits three branches below the critical temperature T_c, implying distinct configurations of the $\mathbf{q} = (\frac{1}{3}, \frac{1}{3}, 1)$ magnetic order. To demonstrate this quasi-degeneracy directly, Fig. 3.11 shows the probability distribution of energy density E, magnetic order parameter $\mathcal{M}$, and spin nematic order parameter Q at three different temperatures below T_c. Interestingly, while a single prominent peak is observed in the distribution of energy and magnetic order, the histogram of the nematic order parameter Q exhibits several peaks, consistent with the multiple branches in Fig. 3.10 (c). This finding clearly indicates a quasi degeneracy of the multiple-$\mathbf{q}$ magnetic orders, and the various quasi-degenerate $\mathbf{q} = (\frac{1}{3}, \frac{1}{3}, 1)$ structures can be divided into three different groups according to their collinearity. We note that a systematic finite-size study is required in order to see whether this quasi-degeneracy structure persists in the thermodynamic limit. However, due to the limitation of our current Monte Carlo simulations that is based on the exact diagonalization method, it is already too costly to compute the histogram for $L = 12$ lattices. Nonetheless, we have compared the histograms of $L = 6$ and $L = 9$ systems and found similar results. In fact, the multiple-peak feature is even more pronounced in the $L = 9$ histogram than the $L = 6$ one.

Another important question is whether the cubic symmetry remains in the $\mathbf{q} = (\frac{1}{3}, \frac{1}{3}, 1)$ magnetically ordered phase. To answer this question, we first define the partial magnetic order parameters $\mathcal{M}_x$, $\mathcal{M}_y$, and $\mathcal{M}_z$, which are sum of $|\mathbf{\Phi}_m|^2$ at wavevectors $\mathbf{q}_m = \left(1, \pm\frac{1}{3}, \pm\frac{1}{3}\right)$, $\left(\pm\frac{1}{3}, 1, \pm\frac{1}{3}\right)$, $\left(\pm\frac{1}{3}, \pm\frac{1}{3}, 1\right)$, respectively. The dependence of these partial magnetic orders are plotted in Fig. 3.10(d) as functions of temperature. It is apparent that the cubic symmetry in the low-T phase is conserved *in average*. However, the issue remains whether individual multi-$\mathbf{q}$ configuration pre-

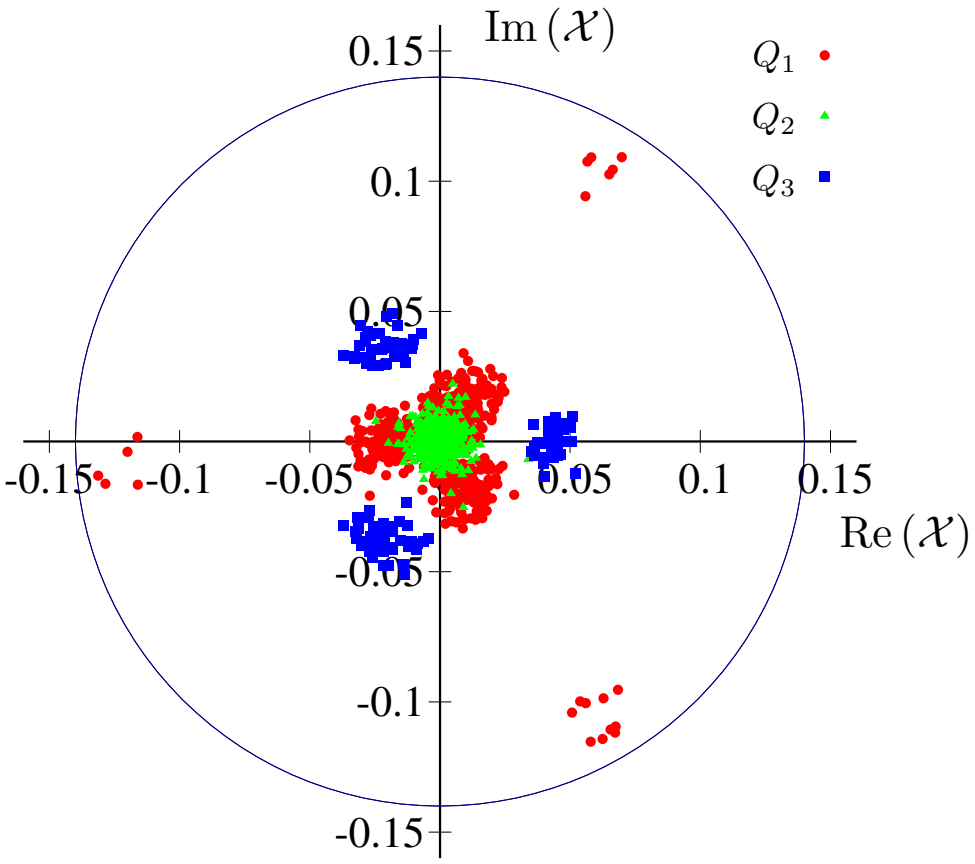

Figure 3.12: Distribution for $\mathcal{X}$ in the complex plane. Red, green, blue points represent independent samples whose nematic order parameter Q is in the left, middle and right peaks, respectively, of the histogram $h(Q)$ in Fig. 3.11(b). Namely, $Q_1 \in [0, 0.17)$, $Q_2 \in [0.17, 0.23)$, $Q_3 \in [0.23, 0.3]$. The figure is obtained with 1000 samples of the system at $T = 0.03, J = 1, L = 6$.

serves the cubic symmetry. To this end, we define a complex order parameter

$$\mathcal{X} = \mathcal{M}_x + \omega \mathcal{M}_y + \omega^2 \mathcal{M}_z \tag{3.15}$$

which measures the disparity between the three partial magnetic orders; here $\omega = e^{i\frac{2\pi}{3}}$. A symmetric phase with $\mathcal{M}_x \approx \mathcal{M}_y \approx \mathcal{M}_z$, thus gives rise to a vanishing complex order parameter $\mathcal{X} \approx 0$.

Fig. 3.12 shows the distribution of $\mathcal{X}$ obtained from 1000 independent Monte

Carlo runs. Interestingly, we find strong correlation between the nematic order Q and the cubic-symmetry parameter $\mathcal{X}$. Here magnetic orders belonging to distinct groups in the histogram (Fig. 3.11) are labeled by three different colors. For example, the $\mathcal{X}$ parameters corresponding to the middle peak of $h(Q)$ in Fig. 3.11(b) cluster around the origin, indicating that these $\mathbf{q} = (\frac{1}{3}, \frac{1}{3}, 1)$ magnetic orders approximately preserves the cubic symmetry. The two distinct parts with smaller Q illustrate the possible existence of two phases corresponding to this peak. On the other hand, magnetic orders with large Q tends to break the cubic symmetry. However, it is worth noting that the cubic symmetry is recovered when averaging over multiple domains each characterized by a different $\mathcal{X}$ in the system. This picture of quasi-degenerate multi-$\mathbf{q}$ manifold is thus consistent with the experimental observation that $GeFe_2O_4$ retains cubic symmetry in the low-T magnetic glassy phase.

We also compute the spin freezing parameter defined as

$$q_{\mathrm{SG}}^{(2)} = \sum_{\mu\nu} \left\langle q_{\mu\nu}^2 \right\rangle , \tag{3.16}$$

where

$$q_{\mu\nu} = \frac{1}{N} \sum_i S_{i,\mu}^{(a)} S_{i,\nu}^{(b)} \tag{3.17}$$

denotes the overlap of spins obtained from two replicas a and b [59]. These two replicas of the same size are simulated independently from different random initial spin configurations. This parameter is nonzero when spins are frozen either in an ordered or a random configuration.

Fig. 3.13 shows the temperature dependence of the $q_{\mathrm{SG}}^{(2)}$ parameter computed from our Monte Carlo simulations for $J = 1$. The freezing parameter starts to grow at the

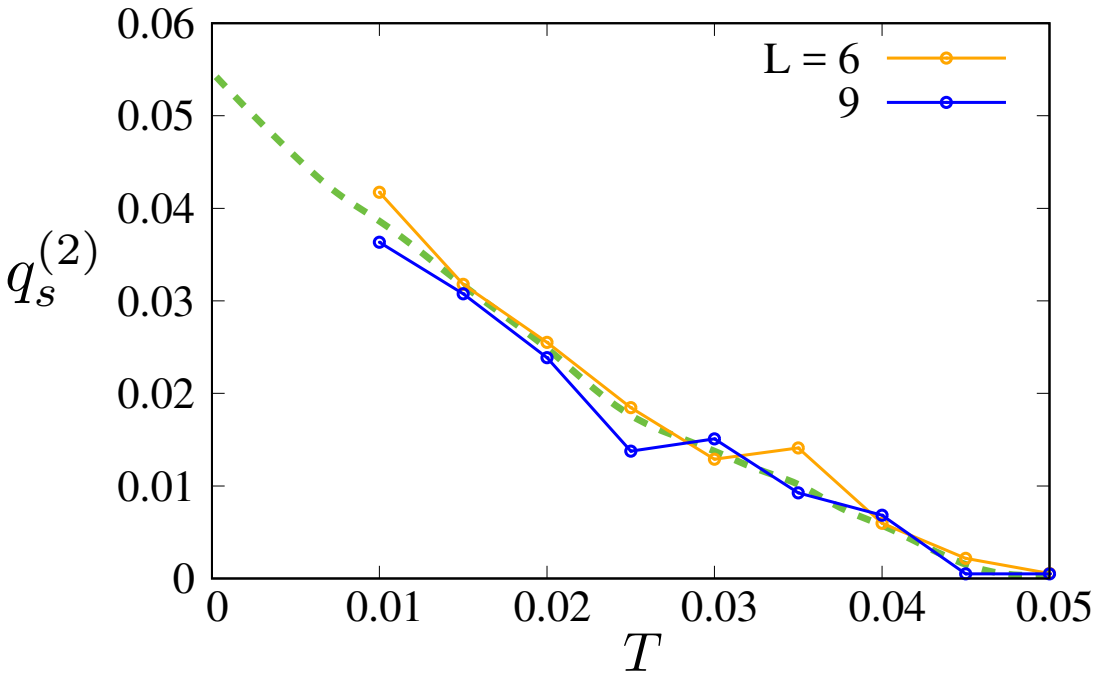

Figure 3.13: The spin freezing parameter $q_s^{(2)}$ as a function of temperature with the electron-spin coupling $J = 1$. The green dashed line is a guide to the eye. The distribution of $q_s^{(2)}$ is rather asymmetric and non-Gaussian.

magnetic transition point. Moreover, the curves for different lattice sizes show rather weak finite size dependence, consistent with a first-order phase transition scenario. Extrapolating to zero temperature, we obtain a nonzero, yet rather small $q_{\mathrm{SG}}^{(2)} \approx 0.05$. This near vanishing of the freezing parameter can be attributed to the quasi-degeneracy of the multiple-$\mathbf{q}$ manifold of the $(\frac{1}{3}, \frac{1}{3}, 1)$ phase. Similar multiple-$\mathbf{q}$ glassy states have also been observed in J_1-J_2 Heisenberg pyrochlore antiferromagnets [60, 61].

3.6 Conclusion and Outlook

To summarize, we have presented a thorough numerical study of a new type of itinerant frustrated magnetism on the pyrochlore lattice. In this model, the pyrochlore

magnet can be viewed as a cross-linking network of Kondo chains. We have obtained the phase diagrams at two representative filling fractions $n = 1/2$ and $2/3$. This model provides a natural explanation to complex spin and orbital structures observed in several spinels compound, which are very difficult to understand within localized spin models.

Importantly, this magnetic phase provides a rather consistent explanation for the recently observed magnetic order in spinel $GeFe_2O_4$ [53]. In this compound, two of the 6 d-electrons of the magnetic Fe^{2+} ion occupy the e_g level, forming the local spins $\{\mathbf{S}_i\}$ with length $S = 1$. The other 4 d-electrons partially fill the t_{2g} orbitals, forming quasi-1D tight-binding chains with a filling fraction $n = 2/3$. Instead of a sharp Bragg peak, neutron scattering experiments show diffusive peaks centered at $\mathbf{q} = (\frac{1}{3}, \frac{1}{3}, 1)$ wavevectors, indicating a short-range spin ordering in this material. This observation is also consistent with the glassy $(\frac{1}{3}, \frac{1}{3}, 1)$ phase of our model. Since the magnetic transition is first order, the correlation length remains finite throughout the phase transition. The large quasi-degeneracy of spin orders in this phase also means that most likely the low temperature phase of $GeFe_2O_4$ consists of finite domains of different magnetic structures.

The $\mathbf{q} = (\frac{1}{3}, \frac{1}{3}, 1)$ glassy phase is reminiscent to other magnetic glassy states reported in strongly correlated systems, including frustrated magnets [62, 63], high-T_c superconducting materials [64, 65], and spin-orbital Mott insulator [66]. All these states are characterized by diffuse scattering at well defined wavevectors, indicating the short-range nature of magnetic orders. A plausible picture for these glassy magnets is the coexistence of domains with different spin structures separated by domain-walls. Moreover, they also exhibit dynamical behaviors [67, 68, 69] that are different from conventional spin glass. Our work along with previous studies [60, 61] suggest that multiple-$\mathbf{q}$ magnetic ordering in frustrated magnets provides a new route

to realize such unconventional glassy magnets and $GeFe_2O_4$ is a potential candidate.

Chapter 4

Dynamics of Phase Separated States in the Double Exchange Model

In this chapter, we study the dynamics of the phase separated states in the square lattice double exchange model. We start by an introduction to the double exchange model, phase separated states and the relevant background. Then we introduce the method we developed to study its dynamics. Finally we present our simulation results and give a detailed discussion.

4.1 Introduction

4.1.1 Manganites

Manganites are a class of mineral with chemical formula $T_{1-x}D_xMnO_3$, where T is a trivalent rare earth element or Bi^{3+} cation , D is a divalent alkaline or Pb^{2+} cation [10]. It can be viewed a mixture of $TMnO_3$ and $DMnO_3$. The Oxygen occupies

two more electrons to constitute O^{2-} and the Mn is in either Mn^{4+} or Mn^{3+} with the proportion determined by x. In 1950, Jonker and Van Santen reported their studies on manganites $La_{1-x}Ca_xMnO_3$, $La_{1-x}Sr_xMnO_3$ and $La_{1-x}Ba_xMnO_3$ for the first time [70]. Manganites have the same crystal structure as perovskite as shown in Fig. 4.1, where the large ions (La^{3+}, Sr^{2+}, Ca^{2+}) reside on the A sites, small ions (Mn^{3+}, Mn^{4+}) occupy the B sites, and the oxygens surrounding the B sites stays at the face centers [4]. It is worth noting that in some manganites, the Mn-O-Mn is always distorted and deviates from 180°.

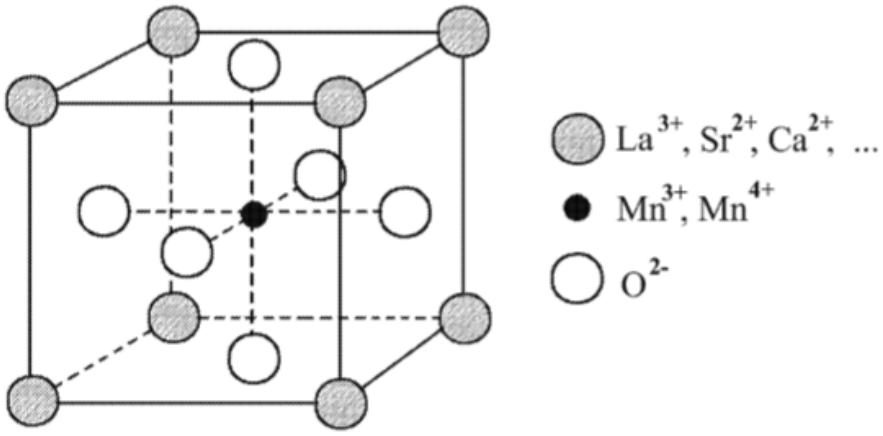

Figure 4.1: Crystal Structure of Manganites from Ref. [4].

By the middle of 1960s, physicists had understood the basic physics of manganites and the research interest faded away [71], until it was brought into attention about 20 years ago. As summarized in [4], the growing interest comes from at least 3 reasons, (1) the colossal magnetoresistance effect, (2) the rich phase diagrams, and (3) the intrinsic inhomogeneity of manganites.

4.1.2 Colossal magnetoresistance

Colossal magnetoresistance (CMR) is the effect of dramatical change in the elec-

trical resistance when a magnetic field is applied. In 1994, a group of researchers prepared thin film of perovskite $La_{0.67}Ca_{0.33}MnO_3$ and measured the magnetoresistance to be more than 3 orders of magnitude higher than the ordinary giant magnetoresistance materials [5]. They defined the MR ratio to be $\Delta R/R_H = (R_H - R_0)/R_H$, where R_H is the resistance R at the magnetic field $H = 6T$ and R_0 is R at $H = 0$. The temperature dependence of the MR ratio was presented in Fig. 4.2. The MR ratio was found to be around 1300% near room temperature and 127,000% near 77K (not shown in the figure) after processing optimizations.

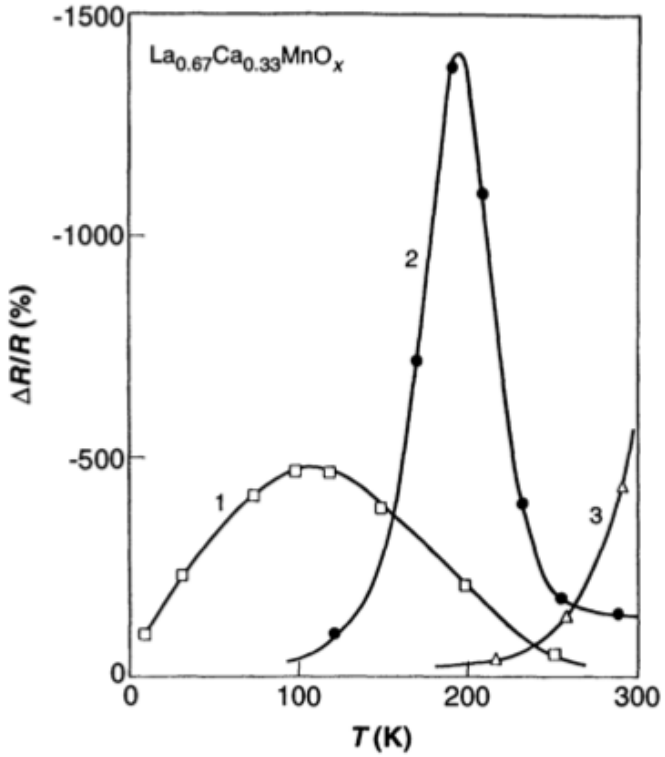

Figure 4.2: Colossal magnetoresistance: the temperature dependence of MR ratio for $La_{0.67}Ca_{0.33}MnO_3$ (La-Ca-Mn-O films) from Ref. [5].

4.1.3 The Double-exchange mechanism and double-exchange model

In 1951, Zener explained the origin of the ferromagnetic phase in manganites using a mechanism later known as *double exchange* mechanism [72]. The $3d$ orbitals are

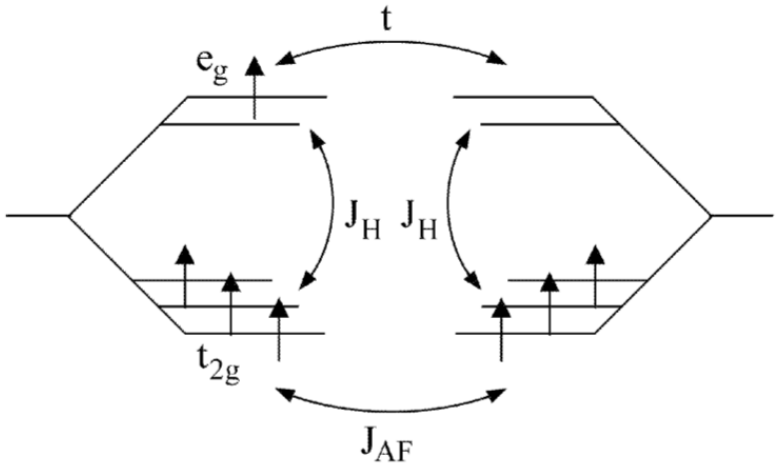

Figure 4.3: The double exchange mechanism from Ref. [4]. J_H is the Hubd's coupling between t_{2g} and e_g orbitals on the same site. J_H is a direct exchange between neighboring sites.

split into a t_{2g} triplet and a e_g doublet with a higher energy. The e_{2g} electrons are localized to be the local magnetic moment while the e_g electrons hopes between sites. Due the ferromagnetic Hund's coupling J_H, the electrons favors a configuration which maximize the total spins. The itinerant e_g electrons do not change the spins while hoping, so the energy will be lowered if the local magnetic moments are aligned with the e_g electrons. This finally induce an indirect ferromagnetic coupling between the local spins. It is worth noting that besides the indirect ferromagnetic interaction mediated by the itinerant electrons, a direct antiferromagnetic coupling J_{AF} also exists in the material.

The Hamiltonian for the double-exchange model resembles that of the Kondo lat-

tice model, with the difference in the sign of the coupling between the local magnetic moments and the conducting electrons. We will discuss the details in the section below.

4.1.4 Phase separation and the dynamics

Phase separation is ubiquitous in systems dominated by nonlinear and non-equilibrium processes [73, 74]. In particular, it has been observed in the intermediate state of numerous first-order phase transitions [75]. Nanoscale phase separation also underpins many of the intriguing functionalities of strongly correlated electron materials [10, 76, 77, 78, 79, 80]. A prominent example is the colossal magnetoresistance (CMR) observed in several manganese oxides [4, 10, 78, 76, 81], in which a small change in magnetic field induces an enormous variation of resistance, as mentioned above. Detailed microscopic studies have revealed complex nano-scale textures consisting of metallic ferromagnetic clusters embedded in an insulating matrix [82, 83, 84]. It is believed that CMR arises from a field-induced percolating transition of the metallic nano-clusters in such mixed-phase states [85, 86, 87].

In a network of nodes and links, percolation theory describes the behavior when a proportion of these nodes or links are removed randomly, and result in fragmented disconnected clusters. For example, in a network, a bond could be either open and allows liquids to flow with probability p, or closed with probability $1 - p$. In a finite lattice (network), the bond percolation problem is calculating the probability of existence of a connected cluster, or equivalently an open path, that connects two ends of the lattice. In an infinite lattice, the question is if there exists a cluster of infinite size in the network. The probability of existence is either 0 below a critical $p = p_c$ or 1 above the critical p_c. In an infinite square lattice, p_c was found to be $\frac{1}{2}$.

In our particular system, although the mechanism of CMR is still under debate,

one possible picture involves percolating transition suggested in Ref. [87]. As illustrated in Fig. 4.4, the phase is separated by antiferromagnetic insulating clusters (red) and ferromagnetic metallic clusters (blue). These metallic clusters are disconnected and spins in different clusters point to different directions. Driven by an external magnetic field, these spins tend to align in the same direction along the magnetic field, and the sizes of insulating clusters are also reduced, resulting in an increased probability p of "open bonds". Consequently, electrons have higher probability to percolate or transit through the system, and the resistivity is reduced.

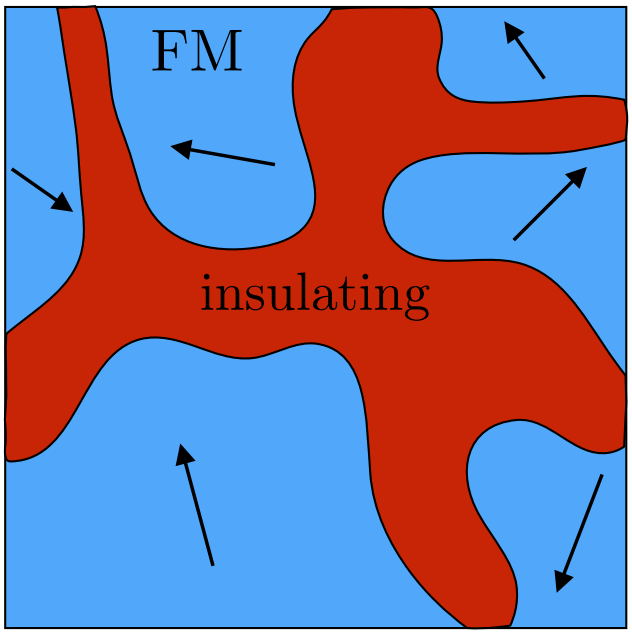

Figure 4.4: Schematic diagram of the phase separation. The red domain is an antiferromagnetic insulating cluster, while the blue domains are ferromagnetic metallic clusters with different directions for spins represented by the arrows.

Considerable experimental and theoretical effort has been devoted to understanding the origin of these complex nano textures in manganites and other correlated systems. An emerging picture is that such inhomogeneous states result from the competition between two distinct electronic phases with nearly degenerate energies.

Microscopically, the double-exchange model [72, 88] is considered a major mechanism for the electronic phase separation. It describes itinerant electrons interacting with local magnetic moments through the Hund's coupling. Since electrons can gain kinetic energy when propagating in a sea of parallel spins, an instability occurs when ferromagnetic domains favored by doped carriers compete with the background antiferromagnetic order. The tendency toward phase separation is further enhanced by factors such as long-range Coulomb interaction, quenched disorder, and coupling to spin, orbital, and lattice degrees of freedom [4].

The magnetization dynamics of the hole-doped manganites $L_{1-x}A_x\mathrm{MnO}_3$, where L is a trivalent lanthanide ion and A is a divalent alkaline earth ion, has also been extensively studied experimentally [89, 90, 91, 92, 93, 94]. The majority of the investigations focused on the ferromagnetic phase with optimal hole doping, which is also the regime exhibiting pronounced CMR effect. While the spin-wave spectrum of some ferromagnetic manganites such as $\mathrm{La}_{1-x}\mathrm{Sr}_x\mathrm{MnO}_3$ is well described by the double-exchange model [95, 96], intriguing unconventional magnetic behaviors have also been reported. For example, the spin wave dispersion of manganites with a lower critical T_c is significantly softened near the Brillouin zone boundary. Moreover, enhanced broadening of magnon excitations has also been observed in several compounds, particularly for large-q excitations approaching the zone boundary. Theoretically, the anomalous spin-wave excitations have been attributed to a host of diverse mechanisms including higher-order effects of spin-charge coupling [97, 98, 99], magnon-phonon coupling [100, 101], orbital fluctuations [102], and disorder effect [103].

4.1.5 Overview

Despite extensive studies on the spin-wave excitations of the ferromagnetic regime, the spin dynamics of the phase-separated states has received much less attention.

From the theoretical viewpoint, the lack of translation invariance in a mixed-phase state renders most momentum-based diagrammatic techniques inapplicable.

In this chapter, we present the first large-scale dynamical simulations of the phase-separated states in the single-band double exchange model based on an efficient real-space formulation of the electron and spin equations of motion. The dynamical structure factor of these highly inhomogeneous states are computed via the space-time Fourier transform of the spin trajectories. We find intriguing coexistence of ferromagnetic and antiferromagnetic magnons at large hole doping. Dynamical signatures of the magnetic polarons and ferromagnetic metallic clusters are also identified. In particular, an abundance of low-energy magnons is found to arise from the larger size metallic clusters.

4.2 The Double-Exchange Model on a Square Lattice

We start with the single-band double-exchange (DE) model on a square lattice,

$$\mathcal{H} = -t \sum_{\langle ij \rangle} \left(c^{\dagger}_{i\alpha} c_{j\alpha} + \text{h.c.} \right) - J \sum_{i} \mathbf{S}_i \cdot c^{\dagger}_{i\alpha} \boldsymbol{\sigma}_{\alpha\beta} c_{i\beta}, \tag{4.1}$$

where repeated indices α, β imply summation. The first term describes the electron hopping: $c^{\dagger}_{i\alpha}$ creates an electron with spin $\alpha =\uparrow, \downarrow$ at site i, $\langle ij \rangle$ indicates the nearest neighbors, t is the electron hopping constant. The second term represents the Hund's rule coupling J between electron spin and the local magnetic moment $\mathbf{S}_i$, which are assumed to be classical spins with length $S = 1$. These interactions are illustrated in Fig. 4.5 (left). The square-lattice DE model has been extensively studied theoretically [6, 104, 105]. We show the results from [6] in Fig. 4.5 (right). Exactly at

half-filling, there is one electron per site on average. Due to Pauli exclusion principle, electrons tend not to hop between sites if they are aligned in the same/close direction. Thus, electrons are antiparallel and are able to hop between nearest sites to lower the energy. The local spins accordingly develop a long-range Néel order in the $T = 0$ insulating ground state. When the electron density $\langle n \rangle$ is small, on the other hand, a metallic state with predominantly ferromagnetic (FM) spin correlation emerges as the ground state. Near half-filling with a small hole doping, the FM metal becomes unstable against either a noncollinear magnetic spiral or phase separation [6, 104, 105, 106] depending on the strength of the Hund's coupling J.

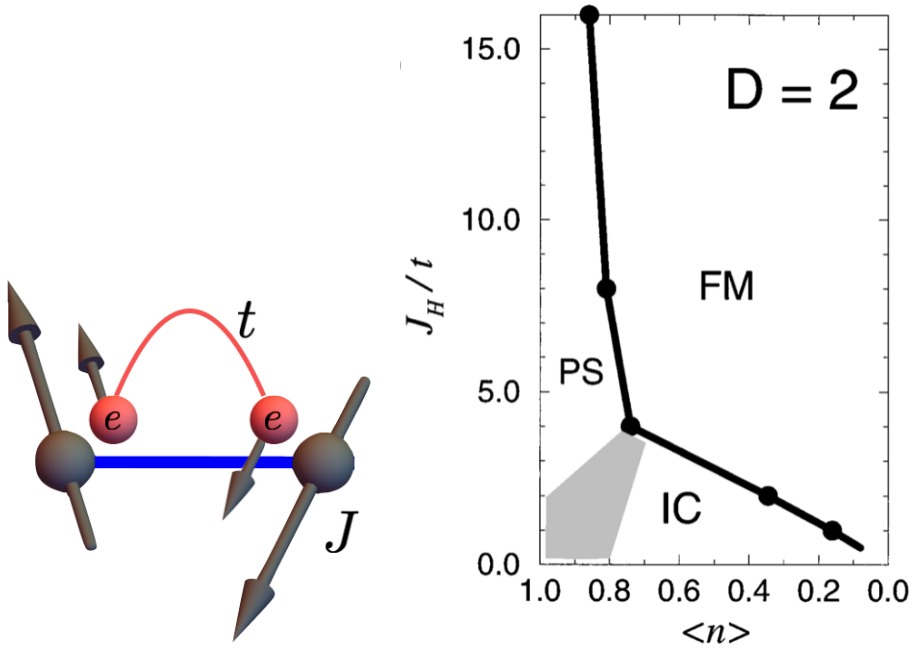

Figure 4.5: Left: interactions in the double-exchange model. Right: phase diagram of the double-exchange model on a square lattice [6], $\langle n \rangle$ is the electron density (number of electrons per site).

In the large-J regime, the instability of the FM phase leads to phase separation with FM domains coexisting with a Néel background. Such mixed-phase state has been observed in Monte Carlo simulations [6]. Because of the nonlocal electronic

degrees of freedom, large-scale equilibrium simulation of the DE model requires efficient algorithms for solving the tight-binding Hamiltonian. The linear-scaling kernel polynomial method (KPM) is usually used to solve the electronic structure problem in simulations of DE model [107, 108, 109]. Here we adopt an efficient Langevin dynamics method combined with a gradient extension of the KPM [110, 111, 112] to obtain equilibrium phase-separated states. A few examples of such mixed-phase states on a 60×60 square lattice are shown in Fig. 4.6. The red region corresponds

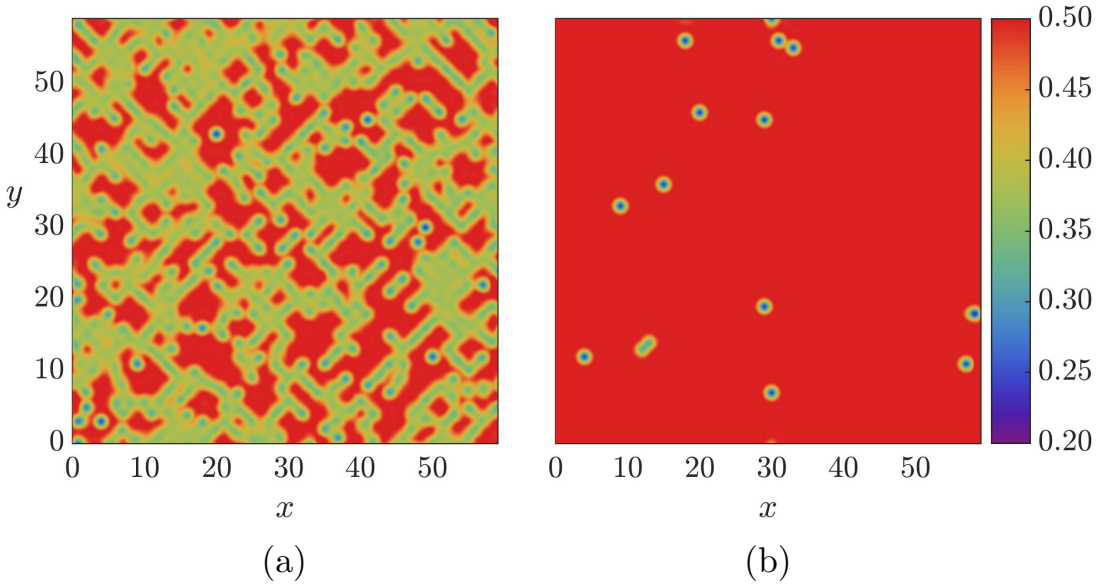

Figure 4.6: The local electron density plots of the phase-separated states with filling fractions (a) $f = 0.43$ and (b) $f = 0.498$ on a 60×60 square lattice. The red region is the half-filled antiferromagnetic insulating background, where the green and blue regions indicate ferromagnetic metallic domains with low electron density.

to the half-filled insulating background with the antiferromagnetic order, while the green and blue regions indicate metallic FM domains with low electron density. Interestingly, in addition to forming puddles of FM state, a fraction of the doped holes are self-trapped in a composite object which can be viewed as the magnetic analog of the polaron [113, 114, 115, 116]. Especially in Ref. [116], the polarons with short range ferromagnetic correlation were found numerically on a three-dimensional lattice

using Monte Carlo. The size of the polarons is 3-4 lattice spacing, consistent with neural scattering experiments.

4.3 Laudau-Lifshitz-von Neumann (LLvN) Dynamics

To describe the dynamics of the DE system, one needs to account for the time evolution of both the local spins and the electrons. Here we assume the dynamics of local moments is governed by the Landau-Lifshitz equation

$$\frac{d\mathbf{S}_i}{dt} = -\mathbf{S}_i \times \frac{\partial \langle \mathcal{H} \rangle}{\partial \mathbf{S}_i} = J\mathbf{S}_i \times \boldsymbol{\sigma}_{\alpha\beta}\, \rho_{i\beta,i\alpha}, \tag{4.2}$$

where

$$\rho_{i\alpha,j\beta} \equiv \langle c^{\dagger}_{j\beta}\, c_{i\alpha} \rangle \tag{4.3}$$

is the reduced single-particle electron density matrix. Importantly, the effective local field

$$\mathbf{h}_i(t) = -\frac{\partial \langle \mathcal{H} \rangle}{\partial \mathbf{S}_i} \tag{4.4}$$

depends on the electron degrees of freedom which have to be propagated simultaneously. The evolution of the electronic state is given by a time-dependent Slater determinant $|\Psi(t)\rangle = \prod_{m=1}^{N_e} \psi^{\dagger}_m(t)|0\rangle$, where the quasi-particle field operator satisfies the Heisenberg equation

$$\frac{\partial \psi_m}{\partial t} = i[\mathcal{H}(t), \psi_m(t)]. \tag{4.5}$$

This approach has been employed to study the photo-induced dynamics of DE system in recent works [117, 118]. However, since the Hamiltonian $\mathcal{H}$ is time-varying through its dependence on $\mathbf{S}_i$, propagation of the Slater determinant is rather cumbersome numerically.

Instead of evolving the many-body wavefunction, one could equally describe the electron dynamics in terms of the reduced density matrix. An additional advantage with this formulation is that it can be straightforwardly generalized to finite-temperature simulations, which are beyond the description of a single Slater determinant. To this end, we define a time-dependent "first-quantization" Hamiltonian

$$H_{i\alpha,j\beta}(t) = -t_{ij}\delta_{\alpha\beta} - J\,\delta_{ij}\,\mathbf{S}_i(t)\cdot\boldsymbol{\sigma}_{\alpha\beta}. \tag{4.6}$$

The DE model in Eq. (4.1) can then be expressed as $\hat{\mathcal{H}} = \sum_{i,j}\sum_{\alpha,\beta} H_{i\alpha,j\beta}\hat{c}^{\dagger}_{i\alpha}\hat{c}_{j\beta}$. In terms of H, the reduced density matrix satisfies the von Neumann equation $d\rho/dt = i[\rho, H]$, or explicitly:

$$\begin{aligned}\frac{d\rho_{i\alpha,j\beta}}{dt} &= i(t_{ik}\,\rho_{k\alpha,j\beta} - \rho_{i\alpha,k\beta}\,t_{kj}) \\ &+ iJ(\mathbf{S}_i\cdot\boldsymbol{\sigma}_{\alpha\gamma}\,\rho_{i\gamma,j\beta} - \rho_{i\alpha,j\gamma}\,\boldsymbol{\sigma}_{\gamma\beta}\cdot\mathbf{S}_j).\end{aligned} \tag{4.7}$$

It can be readily verified that the total energy of the system $E = \langle\mathcal{H}\rangle = \mathrm{Tr}(\rho H)$ is a constant of motion. The numerical efficiency of integrating the von Neumann equation can be improved with optimized sparse-matrix multiplication algorithms. A similar formulation has been developed for the semiclassical dynamics of spin density waves in the Hubbard model [119].

We name the method above Laudau-Lifshitz-von Neumann (LLvN) dynamics. Let's summarize it here. (1) Start with an initial state, build the density matrix.

The initial state can be obtained from other methods. (2) For each time step, apply Runge-Kutta method to propagate the density matrix using Eq. 4.7, and then update the local spins using Eq. 4.2. To be more specific, we propagate the density matrix at time step t_n as

$$\rho_{i\alpha,j\beta}\left(t_{n+1}\right)=\rho_{i\alpha,j\beta}\left(t_n\right)+\frac{1}{6}\left(k_1+2k_2+2k_3+k_4\right)\Delta t \tag{4.8}$$

with Δt the step size and

$$\begin{cases} k_1=\frac{d\rho_{i\alpha,j\beta}}{dt}\left(\mathbf{S}\left(t_n\right),t_n\right) \\ k_2=\frac{d\rho_{i\alpha,j\beta}}{dt}\left(\mathbf{S}\left(t_n\right)+\frac{k_1}{2}\Delta t,t_n+\Delta t/2\right) \\ k_3=\frac{d\rho_{i\alpha,j\beta}}{dt}\left(\mathbf{S}\left(t_n\right)+\frac{k_2}{2}\Delta t,t_n+\Delta t/2\right) \\ k_4=\frac{d\rho_{i\alpha,j\beta}}{dt}\left(\mathbf{S}\left(t_n\right)+k_3\Delta t,t_n+\Delta t\right) \end{cases} \tag{4.9}$$

For a system with N sites, building the density matrix generally take $O(N^3)$ time using exact diagonalization. But the exact diagonalization only need to be performed once at the beginning. In addition, other more efficient methods could be used in this step to reduce running time. Compared to the whole dynamical simulation, the time for this step can be ignored. In step (2), the propagation of density matrix involves matrix multiplication, but the H matrix is a sparse matrix, so the time scales as $O(N^2)$. Updating local spins only takes $O(N)$ time. We perform rank-4 Runge-Kuta, the error per time step dt is as small as $(dt)^5$. This method is surprisingly and reasonably efficient. Compared to a 8×8 lattice in [117] or a 16×16 lattice in [118], this method can elegantly simulate a lattice of size 60×60, which contains one order of magnitude more number of sites.

4.4 Simulation Results

Next we apply the above Laudau-Lifshitz-von Neumann (LLvN) dynamics to compute the dynamical structure factor $\mathcal{S}(\mathbf{q},\omega)$ of the phase-separated states. The initial state is prepared using the Langevin simulations at a temperature of $T = 5\times10^{-4}\,t$. A fourth-order Runge-Kutta method is used to integrate the coupled equations of motions. Given the numerical spin trajectories $\mathbf{S}_i(t)$, the dynamical structure factor is computed from the space-time Fourier transform of the correlation function $C(\mathbf{r}_{ij},t) = \langle \mathbf{S}_i(t)\cdot\mathbf{S}_j(0)\rangle$. Importantly, the dynamical simulations here is completely deterministic and energy-conserving. The symbol $\langle\cdots\rangle$ here denotes ensemble average over independent initial states at the same temperature. The lower panels of Fig. 4.7 show the $\mathcal{S}(\mathbf{q},\omega)$ of phase-separated states with five different electron filling fractions; each is averaged over 50 distinct initial states.

Since the Néel order parameter, characterized by the wavevector $\mathbf{Q} = (\pi,\pi)$ at the M-point, is not a conserved quantity, the fluctuations of the associated Fourier component

$$\tilde{S}(\mathbf{Q},t) \equiv \sum_i \mathbf{S}_i(t)\, e^{i\mathbf{Q}\cdot\mathbf{r}_i} \tag{4.10}$$

produce a huge artifact in the raw data of the dynamical structure factor. Interestingly, we found that the drifting of this Goldstone mode of finite lattices exhibits a $1/\omega$ power-law behavior, extending to very high energies. This observation thus allows us to systematically remove the large artificial signal in the vicinity of the M-point. The $\mathcal{S}(\mathbf{q},\omega)$ shown in Fig. 4.7 were obtained after this subtraction.

The dynamical structure factor in the vicinity of half-filling is dominated by the background antiferromagentic spin-wave excitations, as shown in Fig. 4.7(e). The pronounced signals around the M-point correspond to the Goldstone modes of the

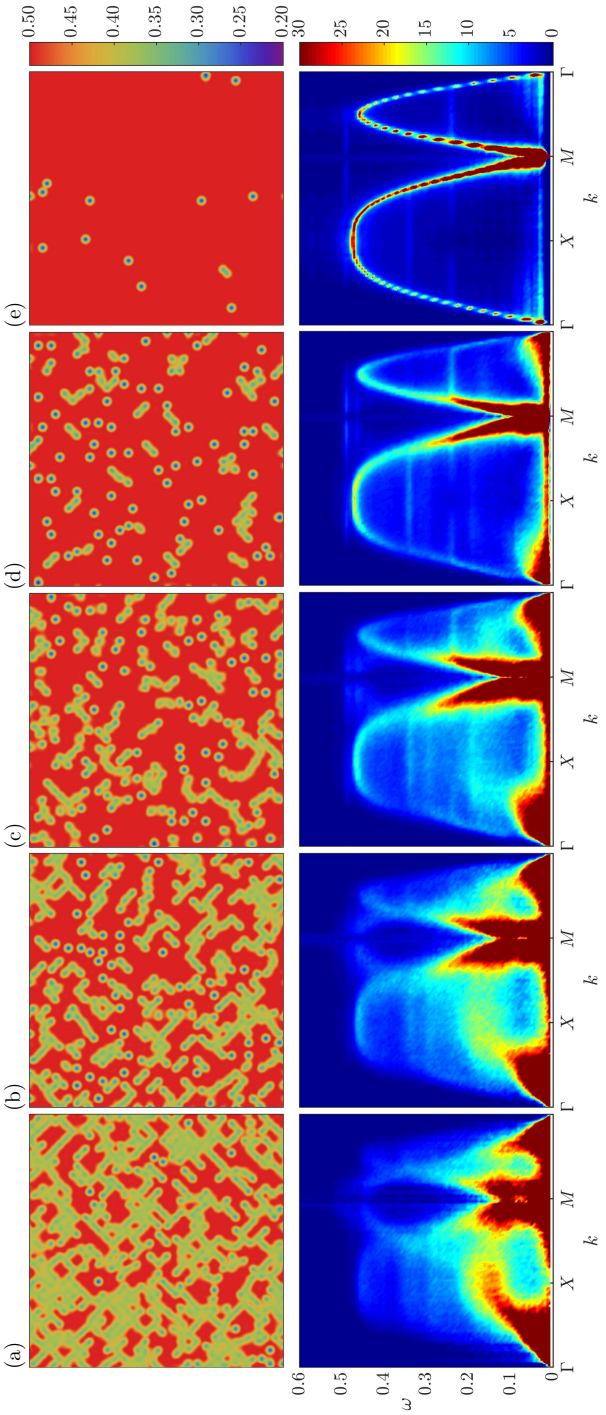

Figure 4.7: Upper panels: density plots of the on-site electron number $n(\mathbf{r}_i) = \langle c^\dagger_{i,\alpha} c_{i,\alpha} \rangle$ in sample phase-separated states for filling fractions (a) $f = 0.43$, (b) $f = 0.45$, (c) $f = 0.465$, (d) $f = 0.48$, (e) $f = 0.498$, obtained from Langevin dynamics simulations on a 60×60 lattice with Hund's coupling $J = 6t$ and temperature $T = 5 \times 10^{-4} t$. The corresponding dynamical structure factors $\mathcal{S}(\mathbf{q}, \omega)$ averaged over tens of independent initial states are shown in the lower panels. The high-symmetry points of the Brillouin zone are $\Gamma = (0, 0), X = (\pi, 0), M = (\pi, \pi)$.

underlying Néel order. As mentioned above, the doped holes in this regime are localized by the self-induced potential in a magnetic polaron. Numerically, each polaron is found to accommodate nearly exactly one hole. To understand the nature of the associated spin excitations, we focus on the dynamics of a single magnetic polaron. To obtain its equilibrium structure, we perform relaxational dynamics on a perturbed half-filled Néel state (by flipping a center spin) with exactly one electron removed. Using this as the initial state for the LLvN dynamics simulation, we then compute the power spectrum

$$I(\omega) \equiv \sum_{i \in \mathcal{C}} |\tilde{\mathbf{S}}_i(\omega)|^2, \tag{4.11}$$

where

$$\tilde{\mathbf{S}}_i(\omega) = \int \mathbf{S}_i(t) e^{-i\omega t} dt, \tag{4.12}$$

and the summation is over five spins at the center of the polaron. The computed spectrum, shown in Fig. 4.8(a), is characterized by prominent peaks at, e.g. $\omega/t = 0.05, 0.25, 0.49$, corresponding to eigen-energies of the spin-wave excitations localized at the magnetic polaron. Importantly, these localized magnons contribute to the flat bands seen in the $\mathcal{S}(\mathbf{q}, \omega)$.

With increasing hole doping, the antiferromagnetic spin-wave dispersion is still visible, yet with gradually reduced strength. Some of the flat-bands due to magnetic polarons also persists. An intriguing new feature is the emergence of a continuum of low-energy magnons throughout the whole Brillouin zone. It is tempting to associate this continuum with the metallic ferromagnetic clusters whose size also grows with increasing hole doping; see Fig. 4.7. To this end, we examine the spectrum of metallic clusters of varying shapes and sizes. Similar to the preparation of the magnetic

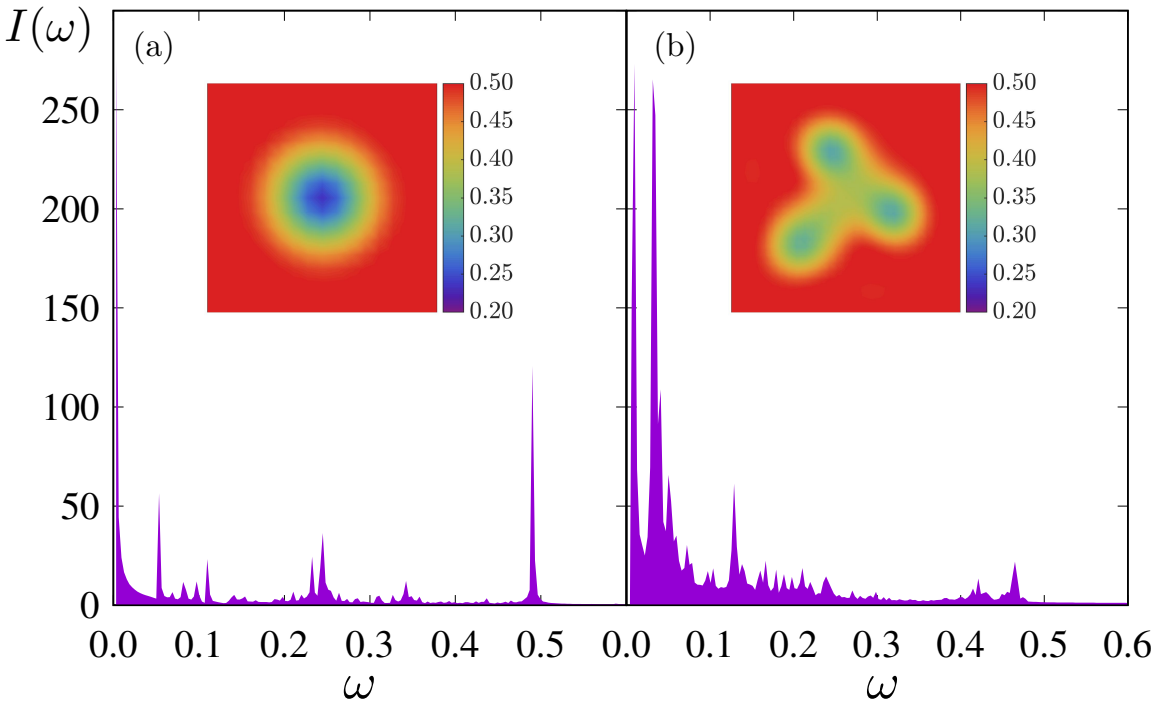

Figure 4.8: The power spectrum $I(\omega) = \sum_{i \in \mathcal{C}} |\tilde{\mathbf{S}}_i(\omega)|^2$ of (a) a magnetic polaron and (b) a FM metallic cluster consisting of roughly 20 spins. Here the sum runs over spins in the FM domain of these object. The inset shows the electron density plot $n(\mathbf{r}_i) = \langle c^\dagger_{i\alpha} c_{i\alpha} \rangle$. With a large Hund's coupling $J = 6t$, the size of the magnetic polaron is rather small, with a radius of roughly three lattice constants.

polaron, we manually create such structures by carefully tuning the hole doping with the cluster size. The LLvN dynamics simulation is then used to compute their power spectrum. Fig. 4.8(b) shows the $I(\omega)$ of such a cluster consisting of roughly 20 spins. A few pronounced peaks, corresponding to the dominant quantized magnons, can be seen in the spectrum. While the intensity and position of these peaks depend on the geometric details of the FM clusters, a common feature of the cluster spectrum is the abundance of low energy modes.

To further investigate the nature of these low-energy magnons, we compare their spatial profile $\mathcal{F}(\mathbf{r})$ with the density plot $n(\mathbf{r})$ from LLvN simulation of a particular initial state, as demonstrated in Fig. 4.9 for two electron filling fractions. Here the magnon profile function is defined as a finite integral of the spin Fourier components

$$\mathcal{F}(\mathbf{r}_i) = \int_{\omega_1}^{\omega_2} |\tilde{\mathbf{S}}_i(\omega)|^2 \, d\omega, \tag{4.13}$$

over a finite band $[\omega_1, \omega_2]$ of small energies. In the case of electron filling $n = 0.465$, where the system is spontaneously segregated into FM domains of various sizes in an AFM background, the dominant spin excitations are from the FM clusters of the doped holes; see Fig. 4.9(a) and (c). As mentioned above, the magnetic polarons dominate the regime of smaller hole doping near half filling. Although the low-energy excitations exhibit a complex profile with various length scales, as shown in Fig. 4.9(d), distinct signals can be seen that are contributed from the magnetic polarons.

We next examine the distribution of low-energy spin excitations of the phase-separated states. Fig. 4.10(a) shows the log-log plot of the dynamical structure factor $\mathcal{S}(\mathbf{q}, \omega)$ versus ω at a few selected wavevectors. Each curve is again obtained after averaging over tens of different mixed-phase configurations. These distributions ex-

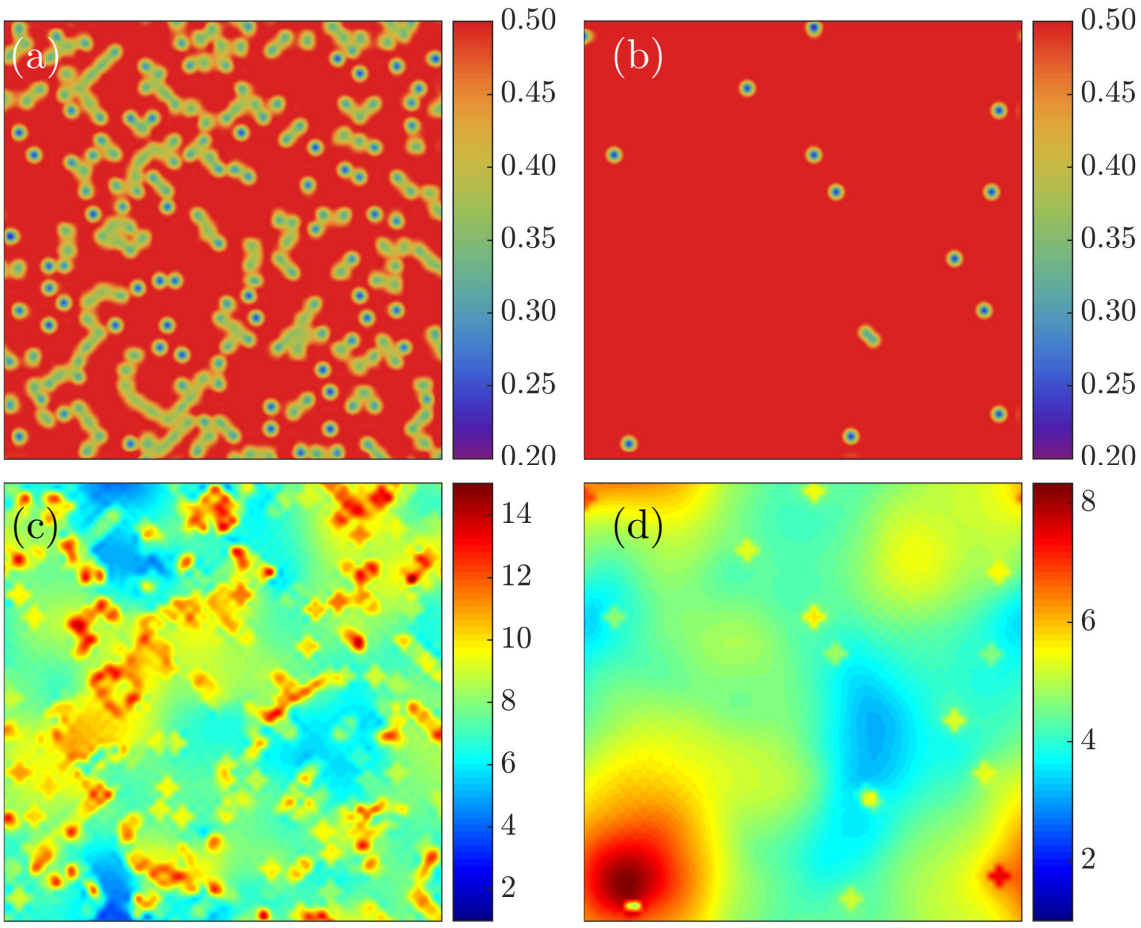

Figure 4.9: Top panels show the density plot $n(\mathbf{r}_i) = \langle c^\dagger_{i\alpha} c_{i\alpha} \rangle$ of one particular phase-separated state for filling fractions (a) $f = 0.465$ and (b) $f = 0.498$. The simulated system size is 60×60. The corresponding spatial profile of spin excitations $\mathcal{F}(\mathbf{r}_i) = \int_{\omega_1}^{\omega_2} |\tilde{\mathbf{S}}_i(\omega)|^2 \, d\omega$ is shown in panels (c) and (d), respectively, where $\omega_1 = 0.006283$ and $\omega_2 = 0.09425$.

hibit an abrupt drop above a band-edge $E_b \sim 0.5t$, indicating the absence of magnon density of states at high energies; see also the density plots in Fig. 4.7. While the high-energy ω dependence of the dynamical structure factor differs at different $\mathbf{q}$, a pronounced increase of $\mathcal{S}(\mathbf{q},\omega)$ at small ω can be seen for all three wavevectors shown in Fig. 4.10(a).

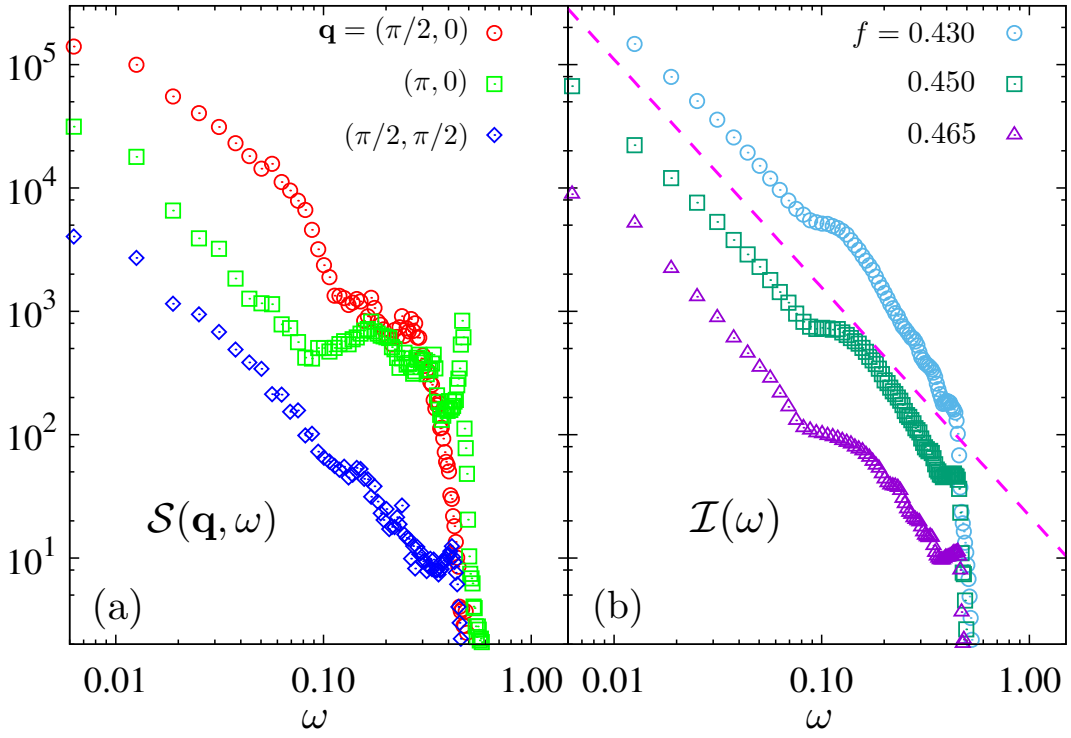

Figure 4.10: (a) The dynamical structure factor $\mathcal{S}(\mathbf{q},\omega)$ versus ω at a few selected wavevectors $\mathbf{q}$ for filling fraction $f = 0.465$. (b) The frequency dependence of the spin excitation spectrum $\mathcal{I}(\omega) \equiv \sum_{\mathbf{q}} \mathcal{S}(\mathbf{q},\omega)/N$ integrated over the whole Brillouin zone, at varying electron filling fractions. The curves are shifted vertically for clarity. The dashed line shows the $\omega^{-1.83}$ power-law dependence.

To further explore this issue, we compute the averaged distribution function

$$\mathcal{I}(\omega) = \frac{1}{N} \sum_{\mathbf{k}} \mathcal{S}(\mathbf{q},\omega) \tag{4.14}$$

by integrating the dynamical structure factor over the whole Brillouin zone. The

obtained distribution functions, shown in Fig. 4.10(b) for three different filling fractions, show strong similarity with each other, especially with increasing hole doping. There are a band-edge and a shoulder-like feature at high energies. Furthermore, the distribution function $\mathcal{I}(\omega)$ develops a sharp peak at $\omega \to 0$, which in turn indicates a significant increase in the magnon density of states (DOS) since the magnon occupation number is roughly a constant at small ω. Moreover, the nearly linear segments in the log-log plot suggest a power-law behavior. As discussed above, this low-energy continuum of magnons can be attributed to the quasi-zero-modes originating from individual FM clusters. It is worth noting that similar disorder-induced peaks at $\omega \to 0$ have also been observed in the magnon DOS in different localized spin models [120, 121].

4.5 Summary and Discussion

To summarize, we have presented an efficient formulation for the real-space dynamics simulation of double-exchange model. Focusing on the regime with small hole doping, we compute, for the first time, the dynamical structure factor of the electronic phase-separated states. At small hole doping close to half-filling, in addition to antieferromagnetic spin-waves from the background Néel order, the spin excitations include distinct flat bands that originates from quantized modes of the small-size magnetic polarons. With increasing doping, a low-energy magnon continuum emerges that is attributed to the quasi-zero-modes of large-size individual FM clusters. Such abundance of low-energy magnons has shown up in recent neutron-scattering measurement of ferromagnetic manganites $La_{0.7}Ca_{0.3}MnO_3$ close to optimal doping [94], although the focus of most studies is still on the anomalous behaviors of the FM magnons in this regime. We have also observed the coexistence of FM and AFM magnons

in the dynamical structure factor with larger hole doping, a result consistent with experiment that shows the coexistence of both spin correlations [122].

While several mechanisms have been proposed to explain the unusual softening and broadening of spin-waves in some manganites, recent experiment [94] highlighted the possibility that this anomalous behavior could be simply caused by the electronic phase separation. With our efficient formulation, it is desirable to quantitatively study the FM magnons in the mixed-phase state, which will be left for future study. Our work also opens a new avenue for dynamical simulations of electronic inhomogeneous states in other systems.

Chapter 5

Summary

We have presented a few numerical studies on the models based on the Kondo lattice model or double exchange moel. In chapter 2, for the 1D Kondo lattice model with quantum 1/2 local spins, we characterized some phases in its phase diagram using density matrix renormalization group (DMRG). We quench the system between representative ground states for different coupling strengths (J) at quarter electron filling. We find that the state stays the same when quenching the ferromagnetic ground state using a Hamiltonian with a lower J in the island phase region via time-evolving block decimation (TEBD). The reverse quench on the island phase using a Hamiltonian with a higher J yields more interesting results. We identified the oscillating pattern of the Loschmidt rate of the reverse quench. Time dependence of other quantities are also identified. The almost linearly increasing entanglement entropy is consistent with other studies on 1D quantum systems. This also indicates that TEBD may not be a good numerical method for long time dynamics of this system, as the bond dimension explodes exponentially with the linearly increasing entanglement entropy.

In chapter 3, we constructed a frustrated magnet on the pyrochlore lattice with

itinerant electrons and performed extensive numerical simulations. In this model, the pyrochlore magnet can be viewed as a cross-linking network of Kondo chains. In several spinels such as $CuIr_2S_4$, $MgTi_2O_4$ and ZnV_2O_4, the localized spin models are difficult to establish some observed complex spin and orbital structures. On the other hand, the itinerant pyrochlore magnet provides a rather natural explanation. We presented the phase diagrams at two representative filling fractions $n = 1/2$ and $2/3$. For the half filling case, we observed a paramagnetic phase and an all-in-all-out phase, mimicking a spin ice. For the case of $2/3$ filling, we found a $(1/3, 1/3, 1)$ magnetic order, ferromagnetic phase, paramagnetic phase and an unexpected $(1/2, 1/2, 1/2)$ order. Especially, we uncover the glassy nature of the $(1/3, 1/3, 1)$ phase, which satisfactorily describes the low temperature phase recently observed in spinel $GeFe_2O_4$. The building block one-dimensional Kondo lattice with classical local moments are also studied.

In chapter 4, a linear scaling kernel polynomial method (KPM) is applied to obtain the equilibrium phase-separated states of the double exchange model on a square lattice. Then we present an innovative and efficient Landau-Lifshitz von-Neumann dynamics (LLvN) framework which enables large-scale dynamical simulation of inhomogeneous electronic states for the very first time. Empowered by the new method, we show dynamical structure factors for the phase separated states. We identify quantized modes of small-size magnetic polarons at small hole doping, and a low-energy magnon continuum at higher hole doping with larger size ferromagnetic clusters. We find the power law dependence of the dynamical structure factor. Relevant experiments on magnetoresistive manganites are also discussed. The state that we are interested in is the phase separated states, which is believed to be the origin of the celebrated colossal magnetoresistance (CMR). To the best of our knowledge, this is the first large-scale dynamical simulation of inhomogeneous electronic states. The

method we developed could be used in other models which involves interactions between electrons and localized spins.

Appendix A

Phase Diagram of 1D Kondo Chain with Classical Spins

In this appendix, we consider the ground state of 1D Kondo chains, which are the backbone of the itinerant frustrated model on the pyrochlore lattice discussed above. The Hamilton of a Kondo chain is

$$\mathcal{H} = -t \sum_i \sum_{\sigma=\uparrow,\downarrow} \left(c^\dagger_{i,\sigma}\, c_{i+1,\sigma} + \text{h.c.} \right) - J \sum_i \mathbf{S}_i \cdot \mathbf{s}_i, \tag{A.1}$$

where $c^\dagger_{i,\sigma}$ is the creation operator of electrons at site-i with spin σ, t is the nearest-neighbor hopping constant, J is the Hund's coupling strength, $\mathbf{S}_i$ is local magnetic moment, and $\mathbf{s}_i = \sum_{\alpha,\beta} c^\dagger_{i\alpha} \boldsymbol{\sigma}_{\alpha\beta} c_{i\beta}$ is the spin of the conduction electron. Since we are interested in magnetically ordered or glass states with frozen nonzero moments, we further assume $\mathbf{S}_i$ are classical spins with magnitude $|\mathbf{S}_i| = 1$. The zero-temperature phase diagram of the classical 1D Kondo chain in the μ-J plane, where μ is the chemical potential of the electrons, has been mapped out in Ref. [56]. Here, instead, we focus on the Kondo chain with a fixed filling fraction $n = 1/2$ and $n = 1/3$, and

obtain the ground states as a function of J. Due to particle-hole symmetry, the $\frac{2}{3}$ filling case studied in chapter 3 for the 3D pyrochlore model, is equivalent to the $\frac{1}{3}$ filling case.

We perform extensive Monte Carlo simulations with Metropolis algorithm to obtain the ground states of the 1D Kondo chain. While most of the results discussed below were obtained from the chain with $N = 72$ spins, we have also conducted simulations with different chain lengths and boundary conditions (periodic vs open boundary conditions) in order to eliminate the finite size effects. To avoid freezing problems, we started our simulations at a relatively high temperature and perform annealing simulations by slowly reducing the temperature. The final spin configuration is determined at $T \approx 10^{-8}$. The structure factor $S(q)$ and correlation function are evaluated and averaged at the final temperature.

We first discuss the half-filling case. Our simulations find a ground state with Néel order, i.e. $\uparrow\downarrow\uparrow\downarrow\cdots$, for all values of electron-spin coupling J, consistent with the results obtained in Ref. [56]. One can understand the stabilization of the Néel order from the weak as well as the strong coupling limits. In the small J limit, the nesting of the Fermi points of a half-filled chain leads to a weak-coupling instability with respect to perturbation of Néel wavevector $q = 2k_F = \pi$. The energy of the Néel ordered state is lowered by opening a spectral gap at the Fermi points. Furthermore, our simulation finds that the energy-gain is maximized by collinear Néel order. In the opposite large J regime, the half-filled chain is a special case in the sense that there exists a macroscopic degeneracy in the $J \to \infty$ limit. In this strong coupling limit, each site binds an electron whose spin is aligned with the local moment $\mathbf{S}_i$, whose direction can point in an arbitrary direction. As discussed in chapter 3, this huge degeneracy is lifted by the nearest-neighbor hopping, giving rise to an effective *antiferromagnetic* spin-spin interaction $J_{\rm AF}\mathbf{S}_i \cdot \mathbf{S}_j$, where $J_{\rm AF} \sim t^2/J > 0$. Consequently, the Néel order

is also stabilized in this large J limit. The cross-linking geometry in the pyrochlore lattice leads to geometrical frustration of Néel ordered chains. The system ends up in an all-in-all-out long-range order in which the Néel order coexists with a ferromagnetic component in each chain.

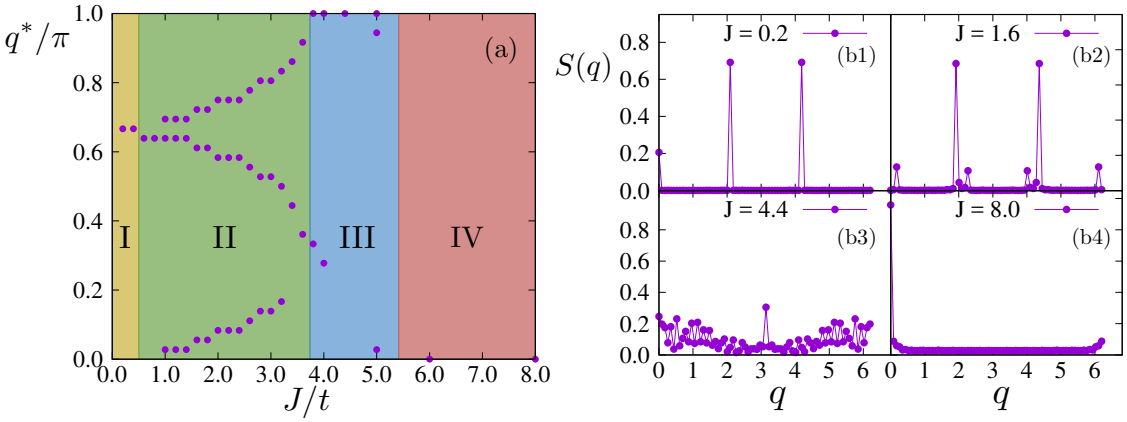

Figure A.1: (a): Wave vectors q^* where the module of $\mathbf{S}(q)$ reaches local maximum for $\frac{1}{3}$ filling. (b1) $\sim$ (b4): $S(q)$ as a function of q for characteristic $J = 0.2, 1.6, 4.4, 8.0$ in region I, II, III, IV.

The 1/3-filled Kondo chain displays a richer phase diagram as shown in Fig. A.1(a). Here we plot the wavevector q^*, which corresponds to the maxima of $S(q)$, as a function of J. At $J \lesssim 0.5$, the ground state shows a spin configuration with a period of 3, represented by a wavevector at $q^* = \frac{2}{3}\pi$, as shown in Fig. A.1 (b1). Again, this magnetic order arises from the weak-coupling instability due to the Fermi point nesting $q^* = 2k_F$ for a 1/3-filled chain. The wavevector $q^* = 2\pi/3$ bifurcates at $J \approx 0.5$ with one branch gradually going down and the other one rising up to $\frac{1}{2}\pi$ (see Fig. A.1 (b2)). The small plateaus for q^* may result from the finite size effect. In region III, the spin structure tends to be non-coplanar and rather complicated, represented by a less pronounced peak at $q^* = \pi$ (see Fig. A.1 (b3)). Starting from $J \approx 5.5$, the ground state is ferromagnetic (Fig. A.1 (b4)). The 3-period phase at small J agrees with that of 3D pyrochlore lattice, while at intermediate J, the

gradual change of q^* is broken by the 3D structure and replaced by a $(1/2, 1/2, 1/2)$ order. In both 1D and 3D models, a large J gives rise to the ferromagnetic phase. The evolution of the most pronounced wave vector, which is the line in the middle in region II of Fig. A.1(a), shows the same trend as that of the quantum Kondo chain [2].

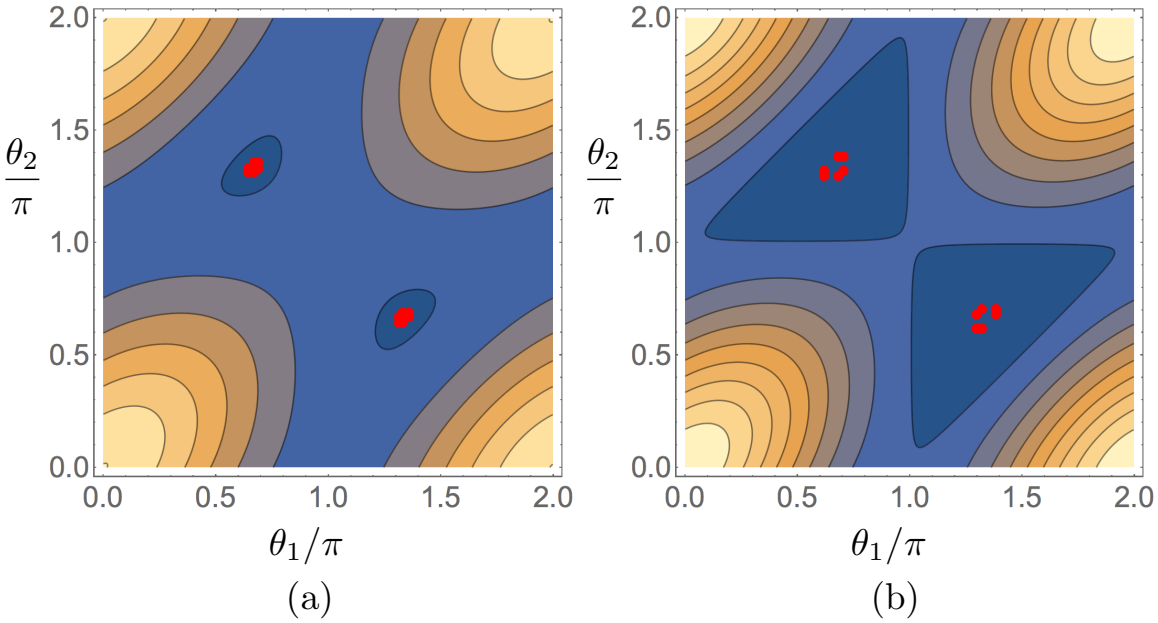

Figure A.2: Energy contour plot with respect to θ_1 and θ_2 for (a) $J = 0.2$, (b) $J = 0.4$. The red dots indicate the optimal configuration. The range for θ_1 and θ_2 is $[0, 2\pi]$. The 12 dots represent the same or symmetry related configuration. For $J = 0.2$, the ground state is the state such that the angles between each of the 3 pairs of $\mathbf{S}_0, \mathbf{S}_1, \mathbf{S}_2$ are $115.8°, 120.6°, 123.6°$. For $J = 0.4$, they are $111°, 112.4°, 126.6°$.

Here we identify the period-3 ground state for small $J = 0.2, 0.4$ at 1/3 filling. Since the ground state is expected to exhibit a 3-period structure due to the Fermi point nesting mechanism as indicated by the Monte Carlo simulations, we can then Fourier transform the real space Hamiltonian to a k-space Hamiltonian

$\mathcal{H} = \sum_k \sum_{i,j=0}^{2} c_{i\alpha}^{\dagger}(k) H_{i\alpha,j\beta}(k) c_{j\beta}(k)$ in which

$$H(k) = \begin{pmatrix} -\frac{1}{2}J\boldsymbol{\sigma}\cdot\mathbf{S}_0 & -te^{ik}\sigma_0 & -te^{-ik}\sigma_0 \\ -te^{-ik}\sigma_0 & -\frac{1}{2}J\boldsymbol{\sigma}\cdot\mathbf{S}_1 & -te^{ik}\sigma_0 \\ -te^{ik}\sigma_0 & -te^{-ik}\sigma_0 & -\frac{1}{2}J\boldsymbol{\sigma}\cdot\mathbf{S}_2 \end{pmatrix} \tag{A.2}$$

where σ_0 is the 2×2 identity matrix. Working on the k-space, we try to identify the ground state local spin configuration. The whole spin chain is composed of multiple periodic duplicates of the first three spins $\mathbf{S}_0, \mathbf{S}_1, \mathbf{S}_2$. It is convenient to set $\mathbf{S}_0 = (0, 0, 1), \mathbf{S}_1 = (\sin\theta_1, 0, \cos\theta_1), \mathbf{S}_2 = (\sin\theta_2\cos\phi_2, \sin\theta_2\sin\phi_2, \cos\theta_2)$. Scanning over $\theta_1, \theta_2, \phi_2$ shows the minimum energy is obtained when $\mathbf{S}_0, \mathbf{S}_1$ and $\mathbf{S}_2$ are coplanar, which allows us to set $\phi_2 = 0$. We can then scan over θ_1, θ_2 only. The final optimal configurations with $J = 0.2, 0.4$ are presented in the figure below. Although it is tempted to consider that the structure with the angle between any pair of spins being 120° is the best configuration, our results show that the optimal state is close to but not exactly the 120° structure and varies with J.

Appendix B

Examples of Matrix Product States and Matrix Product Operators

B.1 Matrix product states: AKLT state

The AKLT state is the ground state of the AKLT Hamiltonian

$$\mathcal{H}_{AKLT} = \sum_i \mathbf{S}_i \cdot \mathbf{S}_{i+1} + \frac{1}{3} \left(\mathbf{S}_i \cdot \mathbf{S}_{i+1} \right)^2 \tag{B.1}$$

with $S = 1$ spins [123, 124]. The ground state can be written as a matrix product state with bond dimension $D = 2$ as follows [25]

$$|AKLT\rangle = \sum_{\sigma} \mathrm{Tr} \left(A^{\sigma_1} A^{\sigma_2} \cdots A^{\sigma_L} \right) |\boldsymbol{\sigma}\rangle \tag{B.2}$$

with

$$A^+ = \sqrt{\tfrac{2}{3}}\sigma^+ = \begin{bmatrix} 0 & \sqrt{\frac{2}{3}} \\ 0 & 0 \end{bmatrix}, \tag{B.3}$$

$$A^0 = -\sqrt{\tfrac{1}{3}}\sigma^z = \begin{bmatrix} -\frac{1}{\sqrt{3}} & 0 \\ 0 & \frac{1}{\sqrt{3}} \end{bmatrix}, \tag{B.4}$$

$$A^- = -\sqrt{\tfrac{2}{3}}\sigma^- = \begin{bmatrix} 0 & 0 \\ -\sqrt{\frac{2}{3}} & 0 \end{bmatrix}. \tag{B.5}$$

B.2 Matrix product operators: Heisenberg Hamiltonian

We take the Heisenberg model as an example from Ref. [7]. The Hamiltonian with open boundary condition can be written as

$$\mathcal{H} = J\sum_{i=1}^{L-1}\left(\frac{1}{2}\left(S_i^+S_{i+1}^- + S_i^-S_{i+1}^+\right) + \hat{S}_i^z S_{i+1}^z\right) + h\sum_{i=1}^{L} S_i^z \tag{B.6}$$

We can introduce the operator valued matrices

$$M^{[i]} = \sum_{\sigma_i,\sigma_i'} M^{\sigma_i,\sigma_i'} \left|\sigma_i\right\rangle \left\langle\sigma_i'\right| \tag{B.7}$$

We expect the matrix product operator representation of the Hamiltonian to be in the form of $H = M^{[1]}M^{[2]}\ldots M^{[L]}$. With this in mind, we construct the automaton diagram for the Hamiltonian as in Fig. B.1. By examining the Hamiltonian B.6 term by term, we could add the local terms S^+, S^z, S^- to our automaton and index the bonds that connect them. We start with the internal state 1. The term $\frac{1}{2}JS_i^+S_{i+1}^-$

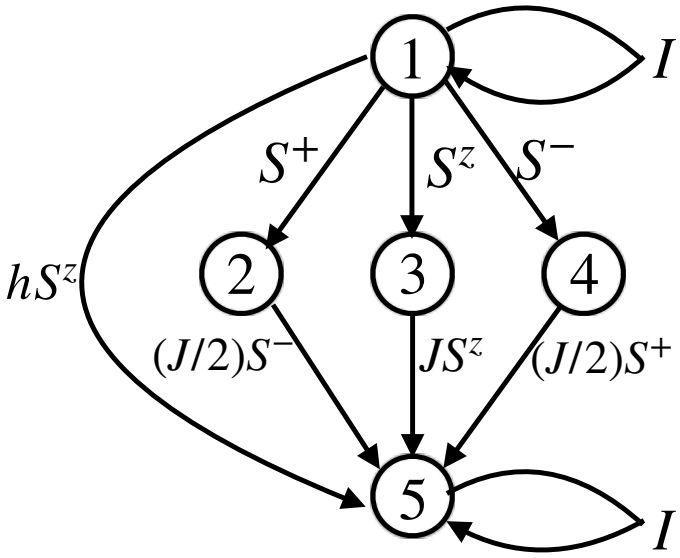

Figure B.1: A schematic diagram of the procedure for obtaining a matrix product operators reproduced from Ref. [7].

can be split as the product of S_i^+ and $\frac{1}{2}JS_{i+1}^-$. So we add a bond S^+ pointing to a new state 2. Similarly, we could add other bonds pointing to internal state 3 and 4. To complete the term $\frac{1}{2}JS_i^+S_{i+1}^-$, we add a bond $\frac{1}{2}JS_{i+1}^-$ starting from internal state 2 and ending at internal state 5. Other terms are treated in the same way. The numbers on the two ends of a bond locates the local operators in the final result. Finally we are able to write the operator valued matrices as

$$M^{[i]} = \begin{bmatrix} I & 0 & 0 & 0 & 0 \\ S^+ & 0 & 0 & 0 & 0 \\ S^z & 0 & 0 & 0 & 0 \\ S^- & 0 & 0 & 0 & 0 \\ hS^z & \frac{J}{2}S^- & J^zS^z & \frac{J}{2}S^+ & I \end{bmatrix}. \tag{B.8}$$

Due to the open boundary condition, on the first and last sites we have

$$M^{[1]} = \begin{bmatrix} hS^z & \frac{J}{2}S^- & J^zS^z & \frac{J}{2}S^+ & I \end{bmatrix}, \tag{B.9}$$

and

$$M^{[L]} = \begin{bmatrix} I \\ S^+ \\ S^z \\ S^- \\ hS^z \end{bmatrix}. \tag{B.10}$$

Here the I is an identity matrix (operator). This provides a general approach for the commonly studied Hamiltonians with short ranged interactions.

Bibliography

[1] M. P. Sarachik, E. Corenzwit, and L. D. Longinotti. Resistivity of mo-nb and mo-re alloys containing 1 *Phys. Rev.*, 135:A1041–A1045, Aug 1964.

[2] D. J. Garcia, K. Hallberg, B. Alascio, and M. Avignon. Spin order in one-dimensional kondo and hund lattices. *Phys. Rev. Lett.*, 93:177204, Oct 2004.

[3] Roderich Moessner and Arthur P. Ramirez. Geometrical frustration. *Physics Today*, 59(2):24–29, Feb 2006.

[4] Elbio Dagotto. *Nanoscale Phase Separation and Colossal Magnetoresistance*. Springer Berlin Heidelberg, 2003.

[5] S. Jin, T. H. Tiefel, M. McCormack, R. A. Fastnacht, R. Ramesh, and L. H. Chen. Thousandfold change in resistivity in magnetoresistive la-ca-mn-o films. *Science*, 264(5157):413–415, 1994.

[6] S. Yunoki, J. Hu, A. L. Malvezzi, A. Moreo, N. Furukawa, and E. Dagotto. Phase separation in electronic models for manganites. *Phys. Rev. Lett.*, 80:845–848, Jan 1998.

[7] Ulrich Schollwöck. *Emergent Phenomena in Correlated Matter: Modeling and Simulation*, volume 3. Forschungszentrum Jülich GmbH, Institute for Advanced Simulation, 2013.

[8] Hirokazu Tsunetsugu, Manfred Sigrist, and Kazuo Ueda. The ground-state phase diagram of the one-dimensional kondo lattice model. *Rev. Mod. Phys.*, 69:809–864, Jul 1997.

[9] Piers Coleman. *Introduction to Many-Body Physics*. Cambridge University Press, 2015.

[10] Elbio Dagotto, Takashi Hotta, and Adriana Moreo. Colossal magnetoresistant materials: the key role of phase separation. *Physics Reports*, 344(1):1 – 153, 2001.

[11] Jun Kondo. Resistance Minimum in Dilute Magnetic Alloys. *Progress of Theoretical Physics*, 32(1):37–49, 07 1964.

[12] W.J. de Haas, J. de Boer, and G.J. van dën Berg. The electrical resistance of gold, copper and lead at low temperatures. *Physica*, 1(7):1115 – 1124, 1934.

[13] P. W. Anderson. Localized magnetic states in metals. *Phys. Rev.*, 124:41–53, Oct 1961.

[14] Alexander Cyril Hewson. *Resistivity Calculations and the Resistance Minimum*, pages 29–46. Cambridge Studies in Magnetism. Cambridge University Press, 1993.

[15] Kenneth G. Wilson. The renormalization group: Critical phenomena and the kondo problem. *Rev. Mod. Phys.*, 47:773–840, Oct 1975.

[16] M. A. Ruderman and C. Kittel. Indirect exchange coupling of nuclear magnetic moments by conduction electrons. *Phys. Rev.*, 96:99–102, Oct 1954.

[17] Tadao Kasuya. A Theory of Metallic Ferro- and Antiferromagnetism on Zener's Model. *Progress of Theoretical Physics*, 16(1):45–57, 07 1956.

[18] Kei Yosida. Magnetic properties of cu-mn alloys. *Phys. Rev.*, 106:893–898, Jun 1957.

[19] Steven R. White. Density matrix formulation for quantum renormalization groups. *Phys. Rev. Lett.*, 69:2863–2866, Nov 1992.

[20] Steven R. White. Density-matrix algorithms for quantum renormalization groups. *Phys. Rev. B*, 48:10345–10356, Oct 1993.

[21] Stellan Östlund and Stefan Rommer. Thermodynamic limit of density matrix renormalization. *Phys. Rev. Lett.*, 75:3537–3540, Nov 1995.

[22] J Dukelsky, M. A Martín-Delgado, T Nishino, and G Sierra. Equivalence of the variational matrix product method and the density matrix renormalization group applied to spin chains. *Europhysics Letters (EPL)*, 43(4):457–462, Aug 1998.

[23] Hiroshi Takasaki, Toshiya Hikihara, and Tomotoshi Nishino. Fixed point of the finite system dmrg. *Journal of the Physical Society of Japan*, 68(5):1537–1540, May 1999.

[24] Steven R. White. Density matrix renormalization group algorithms with a single center site. *Phys. Rev. B*, 72:180403, Nov 2005.

[25] Ulrich Schollwöck. The density-matrix renormalization group in the age of matrix product states. *Annals of Physics*, 326(1):96 – 192, 2011. January 2011 Special Issue.

[26] Steven R. White Matthew Fishman, E. Miles Stoudenmire. Itensor—intelligent tensor—is a c++ library for implementing tensor network calculations.

[27] Guifré Vidal. Efficient classical simulation of slightly entangled quantum computations. *Phys. Rev. Lett.*, 91:147902, Oct 2003.

[28] Pasquale Calabrese and John Cardy. Evolution of entanglement entropy in one-dimensional systems. *Journal of Statistical Mechanics: Theory and Experiment*, 2005(04):P04010, Apr 2005.

[29] Pasquale Calabrese and John Cardy. Time dependence of correlation functions following a quantum quench. *Phys. Rev. Lett.*, 96:136801, Apr 2006.

[30] Walter Selke. The annni model — theoretical analysis and experimental application. *Physics Reports*, 170(4):213 – 264, 1988.

[31] J. T. Chalker, P. C. W. Holdsworth, and E. F. Shender. Hidden order in a frustrated system: Properties of the heisenberg kagomé antiferromagnet. *Phys. Rev. Lett.*, 68:855–858, Feb 1992.

[32] R. Moessner and J. T. Chalker. Properties of a classical spin liquid: The heisenberg pyrochlore antiferromagnet. *Phys. Rev. Lett.*, 80:2929–2932, Mar 1998.

[33] F. Mila edited by C. Lacroix, P. Mendels. Introduction to frustrated magnetism. *Springer Series in Solid-State Sciences*, 2011.

[34] Leon Balents. Spin liquids in frustrated magnets. *Nature*, 464(7286):199–208, Mar 2010.

[35] K. I. Kugel and D. I. Khomskii. Crystal structure and magnetic properties of substances with orbital degeneracy. *Sov. Phys. JETP*, 37(725), 1973.

[36] Hirokazu Tsunetsugu and Yukitoshi Motome. Magnetic transition and orbital degrees of freedom in vanadium spinels. *Phys. Rev. B*, 68:060405, Aug 2003.

[37] S. Di Matteo, G. Jackeli, C. Lacroix, and N. B. Perkins. Valence-bond crystal in a pyrochlore antiferromagnet with orbital degeneracy. *Phys. Rev. Lett.*, 93:077208, Aug 2004.

[38] Gia-Wei Chern. Quantum 120° model on pyrochlore lattice: Orbital ordering in mnv_2o_4. *Physical Review B*, 81(12), 2010.

[39] Paolo G. Radaelli, Y. Horibe, Matthias J. Gutmann, Hiroki Ishibashi, C. H. Chen, Richard M. Ibberson, Y. Koyama, Yew-San Hor, Valery Kiryukhin, and Sang-Wook Cheong. Formation of isomorphic ir3+ and ir4+ octamers and spin dimerization in the spinel cuir2s4. *Nature*, 416(6877):155–158, Mar 2002.

[40] K. Takubo, S. Hirata, J.-Y. Son, J. W. Quilty, T. Mizokawa, N. Matsumoto, and S. Nagata. X-ray photoemission study of $cuir_2s_4$: ir^{3+}–ir^{4+} charge ordering and the effect of light illumination. *Phys. Rev. Lett.*, 95:246401, Dec 2005.

[41] M. Schmidt, W. Ratcliff, P. G. Radaelli, K. Refson, N. M. Harrison, and S. W. Cheong. Spin singlet formation in $mgti_2o_4$: Evidence of a helical dimerization pattern. *Phys. Rev. Lett.*, 92:056402, Feb 2004.

[42] S.-H. Lee, D. Louca, H. Ueda, S. Park, T. J. Sato, M. Isobe, Y. Ueda, S. Rosenkranz, P. Zschack, J. Íñiguez, Y. Qiu, and R. Osborn. Orbital and spin chains in znv_2o_4. *Phys. Rev. Lett.*, 93:156407, Oct 2004.

[43] D. I. Khomskii and T. Mizokawa. Orbitally induced peierls state in spinels. *Phys. Rev. Lett.*, 94:156402, Apr 2005.

[44] Gia-Wei Chern and Cristian D. Batista. Spin superstructure and noncoplanar ordering in metallic pyrochlore magnets with degenerate orbitals. *Phys. Rev. Lett.*, 107:186403, Oct 2011.

[45] Yasuyuki Kato. Quantum monte-carlo study of magnetic ordering in znv2o4. *Physics Procedia*, 34:60 – 65, 2012. Proceedings of the 25th Workshop on Computer Simulation Studies in Condensed Matter Physics.

[46] Paolo G Radaelli. Orbital ordering in transition-metal spinels. *New Journal of Physics*, 7:53–53, Feb 2005.

[47] V. Pardo, S. Blanco-Canosa, F. Rivadulla, D. I. Khomskii, D. Baldomir, Hua Wu, and J. Rivas. Homopolar bond formation in znv_2o_4 close to a metal-insulator transition. *Phys. Rev. Lett.*, 101:256403, Dec 2008.

[48] Christine Kuntscher, Kaneez Rabia, M. K. Forthaus, M. M. Abd-Elmeguid, F. Rivadulla, Y. Kato, and C. D. Batista. Nonmonotonic evolution of the charge gap in znv_2o_4 under pressure. *Phys. Rev. B*, 86:020405, Jul 2012.

[49] M. Croft, W. Caliebe, H. Woo, T. A. Tyson, D. Sills, Y. S. Hor, S-W. Cheong, V. Kiryukhin, and S-J. Oh. Metal-insulator transition in $cuir_2s_4$: xas results on the electronic structure. *Phys. Rev. B*, 67:201102, May 2003.

[50] N. L. Wang, G. H. Cao, P. Zheng, G. Li, Z. Fang, T. Xiang, H. Kitazawa, and T. Matsumoto. Optical study of the metal-insulator transition in $cuir_2s_4$ crystals. *Phys. Rev. B*, 69:153104, Apr 2004.

[51] J. Zhou, G. Li, J. L. Luo, Y. C. Ma, Dan Wu, B. P. Zhu, Z. Tang, J. Shi, and N. L. Wang. Optical study of $mgti_2o_4$: Evidence for an orbital-peierls state. *Phys. Rev. B*, 74:245102, Dec 2006.

[52] H X Yang, B P Zhu, L J Zeng, H F Tian, C Ma, J Shi, and J Q Li. Structural modulation in the orbitally induced peierls state of mgti2o4. *Journal of Physics: Condensed Matter*, 20(27):275230, Jun 2008.

[53] T. Zou, Z. Dun, T. Hong, H. Cao, C. dela Cruz, M. Gottschalk, M. Zhu, H. Zhou, and X. Ke. Spin glass behavior and field induced anisotropic magnetic ordering in s=2 frustrated spinel $gefe_2o_4$. *March Meeting Abstract K5.00009, 2016*, 2016.

[54] J. C. Slater and G. F. Koster. Simplified lcao method for the periodic potential problem. *Phys. Rev.*, 94:1498–1524, Jun 1954.

[55] Junjiro Kanamori. Electron Correlation and Ferromagnetism of Transition Metals. *Progress of Theoretical Physics*, 30(3):275–289, 09 1963.

[56] Sorato Minami and Hikaru Kawamura. Low-temperature magnetic properties of the kondo lattice model in one dimension. *Journal of the Physical Society of Japan*, 84(4):044702, Apr 2015.

[57] J. N. Reimers, A. J. Berlinsky, and A.-C. Shi. Mean-field approach to magnetic ordering in highly frustrated pyrochlores. *Phys. Rev. B*, 43:865–878, Jan 1991.

[58] P. M. Chaikin and T. C. Lubensky. *Principles of Condensed Matter Physics*. Cambridge University Press, 1995.

[59] Dao Xuan Viet and Hikaru Kawamura. Numerical evidence of spin-chirality decoupling in the three-dimensional heisenberg spin glass model. *Phys. Rev. Lett.*, 102:027202, Jan 2009.

[60] Gia-Wei Chern, R. Moessner, and O. Tchernyshyov. Partial order from disorder in a classical pyrochlore antiferromagnet. *Phys. Rev. B*, 78:144418, Oct 2008.

[61] Tsuyoshi Okubo, Trung Hai Nguyen, and Hikaru Kawamura. Cubic and noncubic multiple-q states in the heisenberg antiferromagnet on the pyrochlore lattice. *Phys. Rev. B*, 84:144432, Oct 2011.

[62] M. J. P. Gingras, C. V. Stager, N. P. Raju, B. D. Gaulin, and J. E. Greedan. Static critical behavior of the spin-freezing transition in the geometrically frustrated pyrochlore antiferromagnet $y_2mo_2o_7$. *Phys. Rev. Lett.*, 78:947–950, Feb 1997.

[63] Anjana Samarakoon, Taku J. Sato, Tianran Chen, Gai-Wei Chern, Junjie Yang, Israel Klich, Ryan Sinclair, Haidong Zhou, and Seung-Hun Lee. Aging, memory, and nonhierarchical energy landscape of spin jam. *Proceedings of the National Academy of Sciences*, 113(42):11806–11810, 2016.

[64] M. Matsuda, M. Fujita, K. Yamada, R. J. Birgeneau, M. A. Kastner, H. Hiraka, Y. Endoh, S. Wakimoto, and G. Shirane. Static and dynamic spin correlations in the spin-glass phase of slightly doped $la_{2-x}sr_xcuo_4$. *Phys. Rev. B*, 62:9148–9154, Oct 2000.

[65] Naoyuki Katayama, Sungdae Ji, Despina Louca, Seunghun Lee, Masaki Fujita, Taku J. Sato, Jinsheng Wen, Zhijun Xu, Genda Gu, Guangyong Xu, and et al. Investigation of the spin-glass regime between the antiferromagnetic and superconducting phases in fe1+ysexte1-x. *Journal of the Physical Society of Japan*, 79(11):113702, Nov 2010.

[66] Yongkang Luo, Chao Cao, Bingqi Si, Yuke Li, Jinke Bao, Hanjie Guo, Xiaojun Yang, Chenyi Shen, Chunmu Feng, Jianhui Dai, Guanghan Cao, and Zhu-an Xu. Li_2rho_3: A spin-glassy relativistic mott insulator. *Phys. Rev. B*, 87:161121, Apr 2013.

[67] B. I. Halperin and W. M. Saslow. Hydrodynamic theory of spin waves in spin glasses and other systems with noncollinear spin orientations. *Phys. Rev. B*, 16:2154–2162, Sep 1977.

[68] David F. Mross and T. Senthil. Spin- and pair-density-wave glasses. *Phys. Rev. X*, 5:031008, Jul 2015.

[69] A. M. Samarakoon, M. Takahashi, D. Zhang, J. Yang, N. Katayama, R. Sinclair, H. D. Zhou, S. O. Diallo, G. Ehlers, D. A. Tennant, and et al. Scaling of memories and crossover in glassy magnets. *Scientific Reports*, 7(1), Sep 2017.

[70] G.H. Jonker and J.H. Van Santen. Ferromagnetic compounds of manganese with perovskite structure. *Physica*, 16(3):337 – 349, 1950.

[71] R I Zainullina N G Bebenin and V V Ustinov. Colossal magnetoresistance manganites. *Physics-Uspekhi*, 61(8):719–738, Aug 2018.

[72] Clarence Zener. Interaction between the *d*-shells in the transition metals. ii. ferromagnetic compounds of manganese with perovskite structure. *Phys. Rev.*, 82:403–405, May 1951.

[73] Michael Seul and David Andelman. Domain shapes and patterns: The phenomenology of modulated phases. *Science*, 267(5197):476–483, Jan 1995.

[74] J. P. Gollub and J. S. Langer. Pattern formation in nonequilibrium physics. *Rev. Mod. Phys.*, 71:S396–S403, Mar 1999.

[75] J. D. Gunton, M. San Miguel, and P. S. Saint. *Phase Transitions and Critical Phenomena*, chapter The dynamics of first order phase transitions, pages 269–466. Academic, New York, 1983.

[76] Adriana Moreo, Seiji Yunoki, and Elbio Dagotto. Phase separation scenario for manganese oxides and related materials. *Science*, 283(5410):2034–2040, 1999.

[77] Elbio Dagotto. Complexity in strongly correlated electronic systems. *Science*, 309(5732):257–262, 2005.

[78] Neil Mathur and Peter Littlewood. Mesoscopic texture in manganites. *Physics Today*, 56(1):25–30, jan 2003.

[79] S. A. Kivelson, I. P. Bindloss, E. Fradkin, V. Oganesyan, J. M. Tranquada, A. Kapitulnik, and C. Howald. How to detect fluctuating stripes in the high-temperature superconductors. *Rev. Mod. Phys.*, 75:1201–1241, Oct 2003.

[80] S. A. Kivelson, E. Fradkin, and V. J. Emery. Electronic liquid-crystal phases of a doped mott insulator. *Nature*, 393(6685):550–553, Jun 1998.

[81] Myron B. Salamon and Marcelo Jaime. The physics of manganites: Structure and transport. *Rev. Mod. Phys.*, 73:583–628, Aug 2001.

[82] M. Fäth, S. Freisem, A. A. Menovsky, Y. Tomioka, J. Aarts, and J. A. Mydosh. Spatially inhomogeneous metal-insulator transition in doped manganites. *Science*, 285(5433):1540–1542, 1999.

[83] Ch. Renner, G. Aeppli, B.-G. Kim, Yeong-Ah Soh, and S.-W. Cheong. Atomic-scale images of charge ordering in a mixed-valence manganite. *Nature*, 416(6880):518–521, Apr 2002.

[84] Liuwan Zhang, Casey Israel, Amlan Biswas, R. L. Greene, and Alex de Lozanne. Direct observation of percolation in a manganite thin film. *Science*, 298(5594):805–807, 2002.

[85] M. Uehara, S. Mori, C. H. Chen, and S.-W. Cheong. Percolative phase separation underlies colossal magnetoresistance in mixed-valent manganites. *Nature*, 399(6736):560–563, Jun 1999.

[86] P. Schiffer, A. P. Ramirez, W. Bao, and S-W. Cheong. Low temperature magnetoresistance and the magnetic phase diagram of $La_{1-x}Ca_xMnO_3$. *Phys. Rev. Lett.*, 75:3336–3339, Oct 1995.

[87] J. Burgy, M. Mayr, V. Martin-Mayor, A. Moreo, and E. Dagotto. Colossal effects in transition metal oxides caused by intrinsic inhomogeneities. *Phys. Rev. Lett.*, 87:277202, Dec 2001.

[88] P. G. de Gennes. Effects of double exchange in magnetic crystals. *Phys. Rev.*, 118:141–154, Apr 1960.

[89] Jiandi Zhang, F Ye, Hao Sha, Pengcheng Dai, J A Fernandez-Baca, and E W Plummer. Magnons in ferromagnetic metallic manganites. *Journal of Physics: Condensed Matter*, 19(31):315204, Jul 2007.

[90] H. Y. Hwang, P. Dai, S-W. Cheong, G. Aeppli, D. A. Tennant, and H. A. Mook. Softening and broadening of the zone boundary magnons in $pr_{0.63}sr_{0.37}mno_3$. *Phys. Rev. Lett.*, 80:1316–1319, Feb 1998.

[91] J. A. Fernandez-Baca, P. Dai, H. Y. Hwang, C. Kloc, and S-W. Cheong. Evolution of the low-frequency spin dynamics in ferromagnetic manganites. *Phys. Rev. Lett.*, 80:4012–4015, May 1998.

[92] Pengcheng Dai, H. Y. Hwang, Jiandi Zhang, J. A. Fernandez-Baca, S.-W. Cheong, C. Kloc, Y. Tomioka, and Y. Tokura. Magnon damping by magnon-phonon coupling in manganese perovskites. *Phys. Rev. B*, 61:9553–9557, Apr 2000.

[93] F. Ye, Pengcheng Dai, J. A. Fernandez-Baca, Hao Sha, J. W. Lynn, H. Kawano-Furukawa, Y. Tomioka, Y. Tokura, and Jiandi Zhang. Evolution of spin-wave

excitations in ferromagnetic metallic manganites. *Phys. Rev. Lett.*, 96:047204, Jan 2006.

[94] Joel S. Helton, Susumu K. Jones, Daniel Parshall, Matthew B. Stone, Dmitry A. Shulyatev, and Jeffrey W. Lynn. Spin wave damping arising from phase coexistence below T_c in colossal magnetoresistive $la_{0.7}ca_{0.3}mno_3$. *Phys. Rev. B*, 96:104417, Sep 2017.

[95] Nobuo Furukawa. Spin excitation spectrum ofLa1-xAxMnO3. *Journal of the Physical Society of Japan*, 65(5):1174–1177, may 1996.

[96] Yukitoshi Motome and Nobuo Furukawa. Monte carlo study of doping change and disorder effect on double-exchange ferromagnetism. *Phys. Rev. B*, 68:144432, Oct 2003.

[97] D. I. Golosov. Spin wave theory of double exchange ferromagnets. *Phys. Rev. Lett.*, 84:3974–3977, Apr 2000.

[98] Nic Shannon and Andrey V. Chubukov. Spin-wave expansion, finite temperature corrections, and order from disorder effects in the double exchange model. *Phys. Rev. B*, 65:104418, Feb 2002.

[99] M. D. Kapetanakis and I. E. Perakis. Non-heisenberg spin dynamics of double-exchange ferromagnets with coulomb repulsion. *Phys. Rev. B*, 75:140401, Apr 2007.

[100] Nobuo Furukawa. Magnon linewidth broadening due to magnon-phonon interactions in colossal magnetoresistance manganites. *Journal of the Physical Society of Japan*, 68(8):2522–2525, aug 1999.

[101] L. M. Woods. Magnon-phonon effects in ferromagnetic manganites. *Phys. Rev. B*, 65:014409, Nov 2001.

[102] S Krivenko, A Yaresko, G Khaliullin, and H Fehske. Magnon softening and damping in the ferromagnetic manganites due to orbital correlations. *Journal of Magnetism and Magnetic Materials*, 272-276:458 – 459, May 2004. Proceedings of the International Conference on Magnetism (ICM 2003).

[103] Yukitoshi Motome and Nobuo Furukawa. Disorder effect on spin excitation in double-exchange systems. *Phys. Rev. B*, 71:014446, Jan 2005.

[104] E. Dagotto, S. Yunoki, A. L. Malvezzi, A. Moreo, J. Hu, S. Capponi, D. Poilblanc, and N. Furukawa. Ferromagnetic kondo model for manganites: Phase diagram, charge segregation, and influence of quantum localized spins. *Phys. Rev. B*, 58:6414–6427, Sep 1998.

[105] A. Chattopadhyay, A. J. Millis, and S. Das Sarma. $t = 0$ phase diagram of the double-exchange model. *Phys. Rev. B*, 64:012416, Jun 2001.

[106] Maria Azhar and Maxim Mostovoy. Incommensurate spiral order from double-exchange interactions. *Phys. Rev. Lett.*, 118:027203, Jan 2017.

[107] Nobuo Furukawa and Yukitoshi Motome. Order n monte carlo algorithm for fermion systems coupled with fluctuating adiabatical fields. *Journal of the Physical Society of Japan*, 73(6):1482–1489, June 2004.

[108] G. Alvarez, C. Şen, N. Furukawa, Y. Motome, and E. Dagotto. The truncated polynomial expansion monte carlo method for fermion systems coupled to classical fields: a model independent implementation. *Computer Physics Communications*, 168(1):32–45, may 2005.

[109] Alexander Weiße, Gerhard Wellein, Andreas Alvermann, and Holger Fehske. The kernel polynomial method. *Rev. Mod. Phys.*, 78:275–306, Mar 2006.

[110] Kipton Barros and Yasuyuki Kato. Efficient langevin simulation of coupled classical fields and fermions. *Phys. Rev. B*, 88:235101, Dec 2013.

[111] Kipton Barros, Jörn W. F. Venderbos, Gia-Wei Chern, and C. D. Batista. Exotic magnetic orderings in the kagome kondo-lattice model. *Phys. Rev. B*, 90:245119, Dec 2014.

[112] Zhentao Wang, Gia-Wei Chern, Cristian D. Batista, and Kipton Barros. Gradient-based stochastic estimation of the density matrix. *The Journal of Chemical Physics*, 148(9):094107, Mar 2018.

[113] Nobuo Furukawa. Transport properties of the kondo lattice model in the limit $S = \infty$ and $D = \infty$. *Journal of the Physical Society of Japan*, 63(9):3214–3217, Sep 1994.

[114] C. M. Varma. Electronic and magnetic states in the giant magnetoresistive compounds. *Phys. Rev. B*, 54:7328–7333, Sep 1996.

[115] J. M. D. Coey, M. Viret, L. Ranno, and K. Ounadjela. Electron localization in mixed-valence manganites. *Phys. Rev. Lett.*, 75:3910–3913, Nov 1995.

[116] Hongsuk Yi, N. H. Hur, and Jaejun Yu. Anomalous spin susceptibility and magnetic polaron formation in the double-exchange systems. *Phys. Rev. B*, 61:9501–9505, Apr 2000.

[117] W. Koshibae, N. Furukawa, and N. Nagaosa. Photo-induced insulator-metal transition of a spin-electron coupled system. *EPL (Europhysics Letters)*, 94(2):27003, apr 2011.

[118] Atsushi Ono and Sumio Ishihara. Double-exchange interaction in optically induced nonequilibrium state: A conversion from ferromagnetic to antiferromagnetic structure. *Phys. Rev. Lett.*, 119:207202, Nov 2017.

[119] Gia-Wei Chern, Kipton Barros, Zhentao Wang, Hidemaro Suwa, and Cristian D. Batista. Semiclassical dynamics of spin density waves. *Phys. Rev. B*, 97:035120, Jan 2018.

[120] Akash Chakraborty and Georges Bouzerar. Dynamical properties of a three-dimensional diluted heisenberg model. *Phys. Rev. B*, 81:172406, May 2010.

[121] Matthias Vojta. Excitation spectra of disordered dimer magnets near quantum criticality. *Phys. Rev. Lett.*, 111:097202, Aug 2013.

[122] Tapan Chatterji, M. M. Koza, F. Demmel, W. Schmidt, J.-U. Hoffmann, U. Aman, R. Schneider, G. Dhalenne, R. Suryanarayanan, and A. Revcolevschi. Coexistence of ferromagnetic and antiferromagnetic spin correlations in $la_{1.2}sr_{1.8}mn_2o_7$. *Phys. Rev. B*, 73:104449, Mar 2006.

[123] Ian Affleck, Tom Kennedy, Elliott H. Lieb, and Hal Tasaki. Rigorous results on valence-bond ground states in antiferromagnets. *Phys. Rev. Lett.*, 59:799–802, Aug 1987.

[124] Ian Affleck, Tom Kennedy, Elliott H. Lieb, and Hal Tasaki. Valence bond ground states in isotropic quantum antiferromagnets. *Comm. Math. Phys.*, 115(3):477–528, 1988.